FEDERAL UNIVERSITY OF SÃO CARLOS
CENTER FOR EXACT SCIENCES AND TECHNOLOGY
GRADUATION PROGRAM IN MATERIALS SCIENCE AND ENGINEERING

SELECTIVE LASER MELTING OF A BIOCOMPATIBLE Ti-35Nb-7Zr-5Ta ALLOY

Rodolfo Lisboa Batalha

São Carlos - SP
2019

FEDERAL UNIVERSITY OF SÃO CARLOS
CENTER FOR EXACT SCIENCES AND TECHNOLOGY
GRADUATION PROGRAM IN MATERIALS SCIENCE AND ENGINEERING

SELECTIVE LASER MELTING OF A BIOCOMPATIBLE Ti-35Nb-7Zr-5Ta ALLOY

Rodolfo Lisboa Batalha

Doctoral Thesis presented to the Graduation Program in Materials Science and Engineering as partial requisite to obtain the title of DOCTOR IN MATERIALS SCIENCE AND ENGINEERING.

Supervisor: Prof. Dr. Claudio Shyinti Kiminami
Co-supervisor: Prof. Dr. Piter Gargarella
Funding agency: CAPES and FAPESP (n. 2013/05987-8)

São Carlos - SP
2019

DEDICATION

To my family and friends.

VITAE

Master’s degree in materials engineering by Federal University of Ouro Preto (2015)

Bachelor’s in metallurgical engineering by Federal University of Ouro Preto (2012)

UNIVERSIDADE FEDERAL DE SÃO CARLOS

Centro de Ciências Exatas e de Tecnologia
Programa de Pós-Graduação em Ciência e Engenharia de Materiais

Folha de Aprovação

Assinaturas dos membros da comissão examinadora que avaliou e aprovou a Defesa de Tese de Doutorado do candidato Rodolfo Lisboa Batalha, realizada em 12/08/2019:

Prof. Dr. Piter Gargarella
UFSCar

Bolfarini

Prof. Dr. Claudemiro Bolfarini
UFSCar

Prof. Dr. Tomaz Toshimi Ishikawa
UFSCar

Prof. Dr. Eric Marchezini Mazzer
UFMG

Prof. Dr. Simon Pauly
IFW

Certifico que a defesa realizou-se com a participação à distância do(s) membro(s) Simon Pauly e, depois das arguições e deliberações realizadas, o(s) participante(s) à distância está(ao) de acordo com o conteúdo do parecer da banca examinadora redigido neste relatório de defesa.

Prof. Dr. Piter Gargarella

ACKNOWLEDGMENTS

This study was financed in part by the Coordenação de Aperfeiçoamento de Pessoal de Nível Superior – Brasil (CAPES) – Finance Code 001.

Capes is acknowledged for finance support within the BRAGECRIM Project **n. 88887.137554/2017-00,** and Fundação de Amparo à Pesquisa de São Paulo (FAPESP), within Projeto Temático **n. 2013/05987-8**.

I am thankful to the Graduate Program in Materials Science and Engineering (PPGCEM-DEMa-UFSCar).

I am very thankful to my supervisors Prof. Claudio S. Kiminami and Prof. Piter Gargarella and Prof. Claudemiro Bolfarini for the opportunity and all the lessons, actively participating in my journey and helping me to develop and become a better person and professional.

I want to thank Dr. Simon Pauly for accepting me as his guest at the IFW-Dresden, a life-changing opportunity, with attention and true interest in my development as a researcher.

I would like to thank Dr. Uta Kühn for all the support at the IFW-Dresden and Prof. Tomaz Ishikawa and Prof. Eric Marchezini for agreeing to be reviewers of this Thesis.

I am especially thankful to Dr. Konrad Kosiba, my officemate and friend, for showing me the path to become a true materials scientist and helping me to stay motivated and focused.

I want to thank my dear friends who made my staying abroad an unforgettable time: Dr. Omar O. Salman, Dr. Tobias Gustmann, Dr. Onur Ertugrul, Dr. Hafiz Rub Nawaz Shahid, Dr. Rafael G. Mendes, Dr. Pramote Thirathipviwat, Dr. Akash Kumar, Dr. Pei Wang, Tiabing, Liang Deng, Renan Almeida, Angelo Andreoli, Zichao Li, Mattis Stiebitz…

I am highly grateful to all the help from Dr. Horst Wendrok, Dr. Han Junhee, Dr. Holger Schwab, Heike Bußkamp, Andrea Voß, Birgit Bartusch, Sven Donath, Harald Merker, Alexander Funk, Edson D’Almeida, Regis, Luiz Claudio, Christiane Mix, Alexandre Khant, Juliane Scheiter, Weverson Batalha, Diego Santana…

To all who contributed to this achievement: Thank you!

ABSTRACT

On this work, a novel manufacturing route for processing parts of a biocompatible alloy is studied. Therefore, a biocompatible Ti-35Nb-7Zr-5Ta (wt%) alloy was processed by selective laser melting (SLM). The main SLM processing parameters were defined for the alloy, expanding the mix of materials to be manufactured by SLM. Considering that it is a relatively new alloy composition when it comes to SLM, some samples were also produced by Cu-mould suction casting for comparison. The powder properties were analyzed, the single tracks approach was used, and the best set of parameters were determined to produce bulk samples with relative density of 99.0%. Microstructural features of parts of the TNZT alloy produced by SLM were investigated and a fine columnar-dendritic solidification structure is observed in the as-built samples, whereas an equiaxed dendritic structure was seen in the as-cast samples. A β-Ti single phase structure was identified in the SLM samples, while a β-Ti matrix and α” martensitic laths were observed in the suction-cast samples. The EBSD analysis of the as-built samples shown columnar grains growing epitaxially through several layers, with preferential direction of grain growth, opposed to randomly oriented grains observed in the as-cast samples. The as-built samples presented slightly lower mechanical strength, as a result of the grain structure in the samples produced by SLM. The formation of crystallographic texture was assessed by building cylinders by SLM with different orientation and distinct grain structure and crystallographic textures were developed. Then, some prototypes were manufactured, proving the feasibility of manufacturing parts of a biocompatible alloy with complex geometry by SLM. Finally, an attempt to maximize the pseudoelastic properties of the Ti-35Nb-7Zr-5Ta (wt%) alloy is performed and an innovative approach is proposed to obtain an oligocrystalline structure, combining additive manufacturing with a simple isothermal heat treatment.

Keywords: Additive manufacturing; selective laser melting; Ti alloys; biocompatible alloy; pseudoelasticity; oligocrystalline structure.

RESUMO

FUSÃO SELETIVA A LASER DE UMA LIGA Ti-35Nb-7Zr-5Ta BIOCOMPATÍVEL

Neste trabalho, estudou-se uma nova rota de fabricação de peças de uma liga biocompatível. Assim, uma liga Ti-35Nb-7Zr-5Ta (% em peso) biocompatível foi processada por fusão seletiva a laser (FSL). Os principais parâmetros de FSL foram determinados para a liga, expandindo o portifólio de materiais fabricados por FSL. Considerando que a composição da liga estudada era relativamente nova quando se trata de FSL, algumas amostras foram produzidas por fundição em coquilha de cobre. As propriedades do pó da liga foram analisadas e trilhas simples foram depositadas de forma a definir o melhor conjunto de parâmetros para produzir amostras compactas com densidade relativa de 99,0%. As características microestruturais das amostras da liga TNZT produzidas por FSL foram investigadas, e observou-se uma estrutura de solidificação colunar-dendrítica, enquanto nas amostras fundidas se obteve uma estrutura dendrítica de grãos equiaxiais. Uma estrutura monofásica Ti-β foi identificada nas amostras de FSL, enquanto que uma matriz de Ti-β com ripas de martensita α” foi observada nas amostras de fundição. A análise EBSD das amostras construídas por FSL mostrou grãos colunares crescendo epitaxialmente através de várias camadas, com direção preferencial do crescimento de grãos, diferentemente da estrutura de grãos sem orientação preferencial observada nas amostras de fundição. As amostras de FSL apresentaram resistência mecânica ligeiramente inferior do que as amostras fundidas em coquilha, relacionado a estrutura de grãos nas amostras produzidas por FSL. A formação de textura cristalográfica foi avaliada por meio da construção de cilindros por FSL com diferentes orientações, resultando em estruturas distintas de grãos e texturas cristalográficas. Em seguida, alguns protótipos foram fabricados, comprovando a viabilidade de fabricar peças de uma liga biocompatível com geometria complexa pelo FSL. Finalmente, foi proposta uma alternativa para maximizar as propriedades pseudoelásticas da liga Ti-35Nb-7Zr-5Ta (% em peso), e uma abordagem inovadora é proposta com a formação de uma estrutura oligocristalina, combinando manufatura aditiva a um tratamento térmico isotérmico simples.

Palavras-chave: Manufatura aditiva; fusão seletiva a laser; ligas de Ti; liga biocompatível; pseudoelasticidade; estrutura oligocristalina.

CONTENTS

LIST OF TABLES

LIST OF FIGURES

LIST OF SYMBOLS AND ABBREVIATIONS

AM – Additive Manufacturing;

ASTM – American Society for Testing and Materials;

at% – chemical composition in atomic weight;

BCC – body-centered cubic crystal structure;

BD – building direction;

BSE – back-scattered electrons;

CAD – computer-aided design;

CGHE – carrier gas heat extraction technique;

d_{10} – 10th percentile;

d_{50} – 50th percentile, with also corresponds to the median;

d_{90} – 90th percentile;

DED – direct energy deposition;

E – Young’s modulus;

EBM – electron-beam melting;

EBSD – electron back-scattered diffraction;

EBSP – electron back-scattered pattern;

EDX – energy-dispersive X-ray spectroscopy;

E_l – linear energy input;

E_v – volumetric energy input;

GA – gas atomization;

G_C – gradient in the equilibrium liquidus temperature;

G_L – thermal gradient in the liquid phase;

h_s – hatching distance;

HT – heat treatment;

HV – Vickers hardness;

$HV_{0.1}$ – Vickers micro hardness with 100 gf of load;

$HV_{0.2}$ – Vickers micro hardness with 200 gf of load;

ICP-OES – inductively coupled plasma optical emission spectroscopy;

IPF – inverse pole figure;

ISO – International Organization for Standardization;

L – liquid state;

$\bar{l}_l$ – longitudinal intercept length

$\bar{l}_t$ – transverse intercept length

l_z – layer thickness;

M – mushy zone;

OM – optical microscope;

$M_s^{\alpha'}$ – martensitic start transformation temperature;

$M_f^{\alpha'}$ – martensitic final transformation temperature;

PA – plasma atomization;

PBF – powder bed fusion;

P_l – laser power;

PREP – plasma rotating electrode process;

PSD – particle size distribution;

R – solidification rate;

RA – rotatory atomization;

S – solid state;

SAED – selected area electron diffraction;

SE – secondary electrons;

SEM – scanning electron microscopy;

SLM – Selective Laser Melting;

TEM – Transmission Electron Microscope;

TNZT – Ti-35Nb-7Zr-5Ta (wt%) alloy;

TNZT-HE – samples of the TNZT alloy processed by SLM with high energy;

TNZT-LE – samples of the TNZT alloy processed by SLM with low energy;

T_q – final quenching temperature;

$\dot{T}$ – cooling rate;

$T^{\alpha/\beta}$ – beta *transus* temperature;

$T_0^{\beta/\omega}$ – transformation temperature from beta to omega;

UAM – ultrasonic additive manufacturing;

v_s – scanning speed

Wt% - chemical composition in weight percentage;

XRD – X-ray diffraction;

α – alfa-Ti phase with hexagonal structure;

α' – martensitic phase with hexagonal structure;

α'' – martensitic phase with orthorhombic structure;

β – beta-Ti phase with body-centered cubic structure;

ε_{se} – recoverable strain;

μ-XCT – X-ray computed micro-tomography;

$\sigma_{35\%}$ – compression stress at 35% of true strain;

σ_{YS} – Yield Strength;

ω_{ath} – athermal omega phase with trigonal structure;

ω_{iso} – isothermal omega phase with hexagonal structure.

1 INTRODUCTION

Additive manufacturing is defined by ISO/ASTM 52900:2015 as a “process of joining materials to make parts from 3D model data, usually layer upon layer, as opposed to subtractive manufacturing methodologies” [1]. The processes of additive manufacturing (AM) of metals have been drawing considerable attention due to the great flexibility of manufacturing parts and components with complex geometry, tight control of the microstructure, shorter lead time (time between development and manufacture of a product) and less usage of raw material [2-7]. The primary focus of AM is customization of low volume, high value-added products that may be manufactured quickly [8, 9]. The technology has been adopted as a processing route in aerospace, biomedical, automotive and robotic industries, with an expectation of expressive growth at a rate of 18% per year until 2025 [4]. It allows near net-shape production, without the need of expensive moulds and dies, a high material utilization rate, direct production based on a CAD model, and a high level of flexibility (e.g. parts with different geometry can be produced in the same batch) [4, 10].

The most popular denomination for additive manufacturing is the term "3D printing", relating to the construction of objects by consecutive deposition of two-dimensional layers "printed" on top of each other. Each layer is a section of a three-dimensional CAD (Computer Aided Design) model of a component [4, 5]. The most known metal additive manufacturing processes are electron-beam melting, laser-powder bed fusion, also known as selective laser melting, and direct energy deposition [2-7]. Selective laser melting (SLM) is an additive manufacturing technique and uses a laser beam to melt successive layers of metallic powder and consolidate the 3D part [2-4, 7, 11].

Metallic materials employed on medical and dental fields are especially suitable to be produced by SLM due to their complex geometry, individualization and high-aggregate value [12, 13]. Another important feature is the possibility to manufacture multiple individual parts in one batch, enabling mass customization [14]. Metallic materials are used as structural parts for medical devices in the fields of orthopedic surgery, blood circulatory system and dentistry [15, 16].

Approximately 70% of the structural implants are made of metallic materials [16]. The main metals applied as biomaterials are stainless steel, Co-Cr alloys, Ti and Ti-alloys [17, 18]. Ti and Ti-based alloys are widely used as biomedical materials since they have interesting properties as high strength-to-density ratio, low stiffness, good fatigue resistance, biocompatibility, and high corrosion resistance as the passivation film can be formed easily on the surface [15, 19]. Figure 1.1 shows examples of metallic implants produced by additive manufacturing.

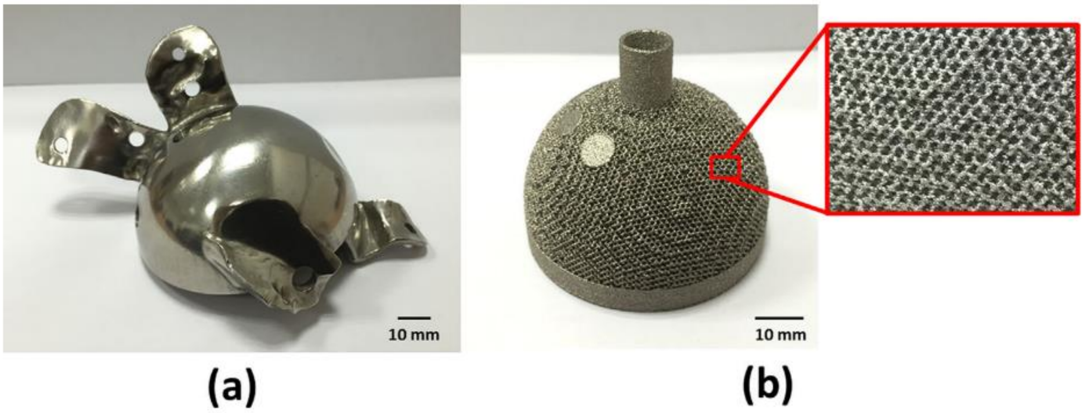

Figure 1.1. Metallic implants produced by additive manufacturing: a) hip joint and b) as-built acetabular cup [12].

The Ti-6Al-4V alloy (wt%), developed for aerospace applications, was the first Ti-based alloy applied in implants [18]. However, studies have shown toxic effects of Al e V, associated with a reasonably high Young’s modulus of the alloy (103-120 GPa) when compared to the bone (10-30 GPa). The mismatch of Young’s modulus between natural bone and bulk metallic biomaterial is a major problem for titanium implants in orthopedic surgery, which may lead to insufficient load of bone and cause stress shielding. Then, stress shielding will result in the fracture of bone and eventual loosening of the implants [15, 16]. This fact has drawn the attention for research of new alloys presenting lower Young’s modulus and absent of toxic elements. Some studies have shown the elements Ti, Nb, Zr and Ta as atoxic, without causing allergic reactions on living organisms. Therefore, those elements emerge as alternative for the more conventionally used Ti-6Al-4V alloy [15, 20-22].

β-Ti alloys are considered the most versatile among Ti alloys, offering good combination of mechanical strength and ductility, besides low Young's modulus [23, 24]. The low Young's modulus, for instance, allows the development of implants with higher biomechanical compatibility with cortical bones (Figure 1.2), which has resulted in great interest on research and development of β-Ti alloys for biomedical applications [17, 18, 20, 25].

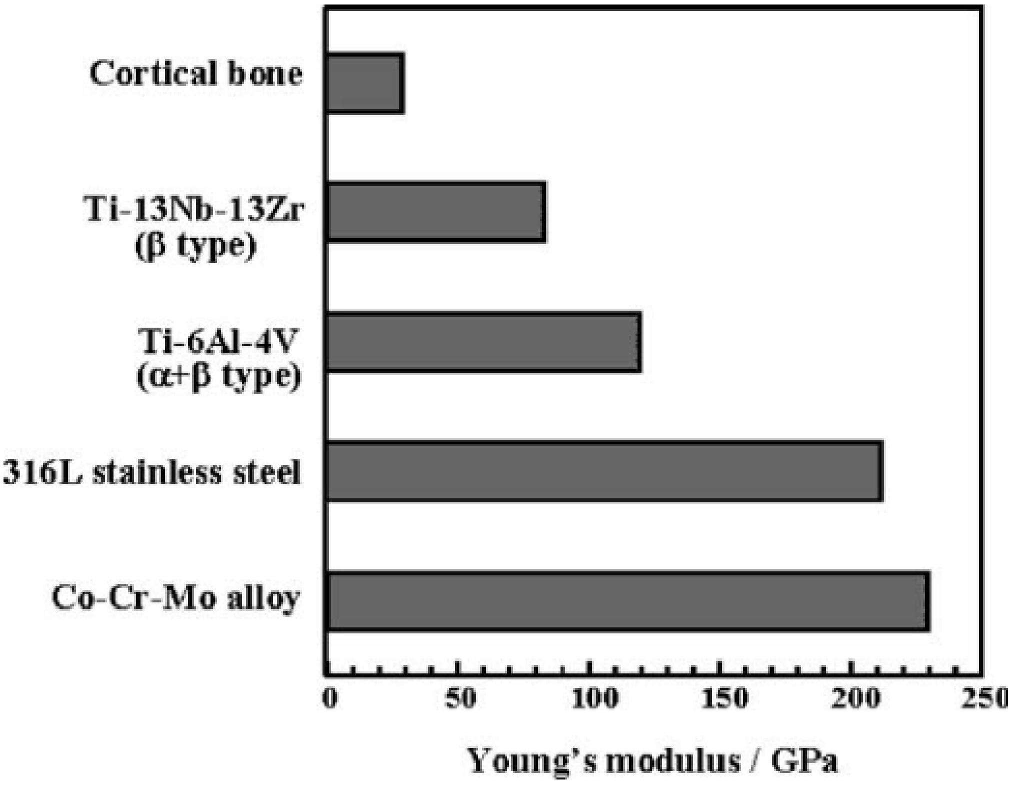

Figure 1.2. Young's modulus of metallic alloys applied on implants, compared to cortical bone [20].

The biocompatible β-Ti metastable alloys of the Ti-Nb system have been given especial attention for biomedical applications. In fact, these alloys present the lowest Young's modulus among Ti alloys [26-28]. In addition, Ti-Nb-based alloys show shape memory effect and pseudoelasticity due to a thermoelastic martensitic transformation (α", orthorhombic structure), although these effects are reportedly less pronounced than the observed in Ni-Ti-based alloys [15, 16, 25].

A promising Ti-Nb-based alloy for orthopedic protheses and biomedical applications, and subject of the present work, is the quaternary Ti-35Nb-7Zr-5Ta (wt%) alloy, commercially known as TiOSteum®, TNZT or Ti-35-7-5 (Unified Numbering System R58350). The TNZT alloy was developed in the 2000's for biomedical application, presents beta phase stable at room temperature, pseudoelasticity and Young's modulus of 50-70 GPa [26-31].

Nonetheless, the limited availability of some materials in powder form and the extensive research that is still needed to optimize the process for a given material restrict the material range that can currently be processed by SLM [9, 11]. The manufacturing of metal products by selective laser melting is only in its early stages, with few materials being processed. More specifically, Co-Cr alloys, stainless steel, tool steels, titanium and its alloys (especially Ti-6Al-4V alloy) and Al-casting alloys may be commercially produced by SLM [2-11]. Therefore, on this work a beta Ti-35Nb-7Zr-5Ta (wt%) biocompatible alloy was processed by selective laser melting. The parameters are optimized, in order to obtain bulk samples with relative density ≥ 99.0% and expand the mix of materials to be processed by SLM for biomedical applications. Considering that it is a relatively new alloy composition when it comes to SLM, some samples are also produced by Cu-mould suction casting for comparison.

A deep understanding of feedstock materials, processes, structures and properties are necessary to produce defect-free additive manufactured parts. The AM of metals has its foundation based in metal powder technology, high-energy beam welding, cladding and prototyping. However, significant research is still required for studies of microstructure formation and resulted mechanical properties of additive manufactured parts, relating to the different processing conditions [4]. Accordingly, the present work deals with microstructural features of parts of Ti-35Nb-7Zr-5Ta (wt%) alloy produced by selective laser melting, correlating mechanical properties with metallurgical aspects.

One of the drawbacks of Ti-Nb-based alloys is the low recoverable strain when compared to the Ni-Ti system, which limits the scalability of Ti-Nb alloys in biomedical applications when pseudolelasticy is required (e.g. stents). Recent studies have reported an alternative method to improve pseudoelasticity of Cu-based shape-memory alloys. An oligocrystalline structure is formed (oligo – few; crystalline – crystals), also known as *bamboo structure* (Figure 1.3), resulting in recoverable strain and pseudoelasticity comparable to those observed in single crystals of Cu-based alloys [32, 33].

Figure 1.3 Optical micrograph of a Cu-Zn-Al microwire longitudinal cross section, with bamboo-like structure of grains [34].

The method to obtain such oligocrystalline structure is the Taylor wire casting technique, in which microwires are produced directly from the melt, resulting in filaments with ≤ 150 μm of diameter [34]. Although the Taylor method has its advantages compared to wire drawing, it is limited to alloys with lower melting point and specifically designed to produce wires on micro scale [35]. On this sense, an attempt to maximize the pseudoelastic properties of the Ti-35Nb-7Zr-5Ta (wt%) alloy is performed, by forming oligocrystalline structure in thin-walled samples produced by selective laser melting. The aim is to explore new perspectives of widening the applicability of the Ti-Nb-based alloy when pseudoelasticity is required, by tailoring the microstructure with selective laser melting, while the metallurgical aspects and processing conditions are assessed.

1.1 Aims and Objectives

The general objective of this Doctoral Thesis is the development of a novel manufacturing route for processing parts of a biocompatible Ti-35Nb-7Zr-5Ta (wt%) alloy by means of additive manufacturing. Therefore, selective laser melting is studied, and the main processing parameters are optimized for the TNZT alloy, expanding the palette of materials to be processed by SLM. Microstructural features and resulted mechanical properties are investigated and new perspectives of tailoring the microstructure of the Ti-Nb-based alloy are explored.

The specific objectives of this Thesis are:

- To analyze the feasibility of the Ti-35Nb-7Zr-5Ta (wt%) powder to be used in the selective laser melting process;
- To attest the processability of the TNZT alloy by selective laser melting and identify the optimum parameters to manufacture bulk samples;
- To study the processing-microstructure-properties correlation when producing samples of TNZT by SLM and compare to a more conventional Cu-mould suction casting technique;
- To investigate grain structure formation in selective laser melting and after post-processing heat-treatment;
- To investigate oligocrystaline structure formation in selective laser melted thin-walled samples.

2 LITERATURE REVIEW

2.1 Additive Manufacturing of Metals

Additive manufacturing of metals (AM), also widely known as metal 3D printing, is a method to manufacture parts in a layer-by-layer manner. The technologies behind the AM processes evolved expressively in the past 30 years, especially focused on the science of metal additive manufacturing, with new machines and materials developed [4, 10, 11, 36]. Additive manufactured parts are made by adding material in layers and each layer is a cross-section of the part based on the CAD model [10]. It involves several steps from the design to the resultant part (Figure 2.1), by consolidating feedstock material into solid 3D structure, either fully dense or with certain level of porosity depending on the desired application [10, 37].

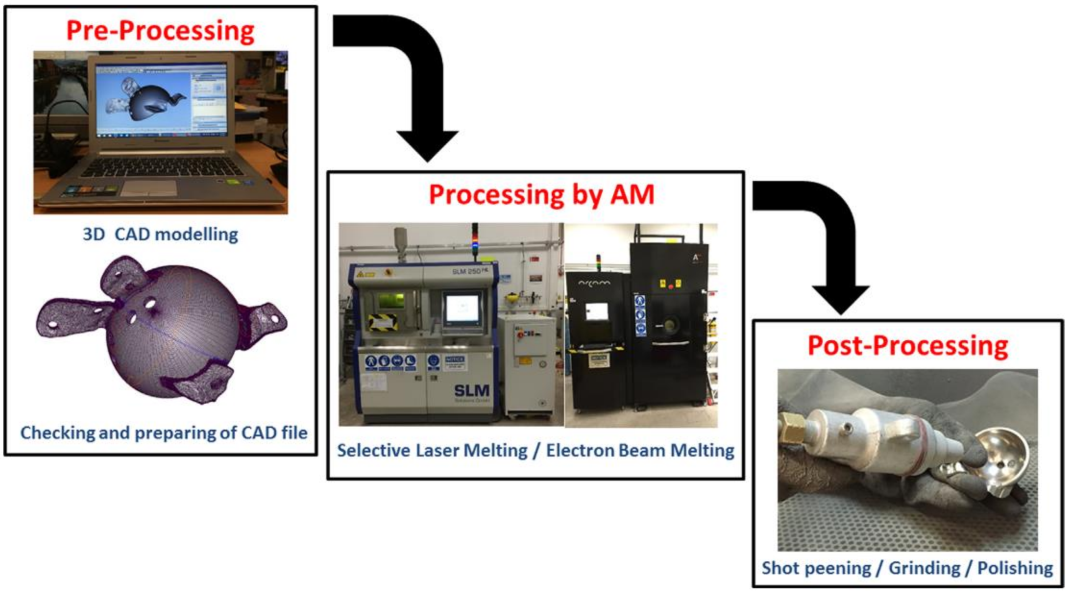

Figure 2.1. Sequence of steps in additive manufacturing: from the CAD model to the final part [12].

The production of complex or customized parts directly from the design without the need for expensive tooling, dies or casting moulds, and eliminating many conventional processing steps are the biggest advantages of additive manufacturing. Intricate parts may be manufactured in one-step without the limitations of conventional processing methods (e.g. straight cuts, round holes in machining operations) or commercial shapes (e.g. sheet, tubing) [10, 37]. A significant reduction in the part count may be realized by eliminating or reducing the need to assemble multiple components. In addition, parts may be manufactured on demand, reducing the inventory of spares and decreasing lead time for critical or obsolete replacement components [11, 38]. On the other hand, limited build volumes, slow deposition rates, high feedstock and machine costs limit the current use of the technology. Therefore, the complexity of part geometry is the critical factor which defines whether AM is an economically viable production pathway [2, 4].

The metal AM processes must consolidate feedstock as powder, sheets or wire into a dense part, which may occur by sintering, melting or solid-state joining. Therefore, metal AM processes are categorized in four main classes, with its unique applications, strengths and challenges: Powder bed fusion (PBF), which includes selective laser melting (SLM) and electron beam melting (EBM); Direct energy deposition (DED), with laser- and electron beam-based processes; Binder jetting, including infiltration and consolidation processes; Sheet lamination, which is basically ultrasonic additive manufacturing (UAM) [2]. On the present work, the denomination selective laser melting (SLM) will be used to describe the powder-bed fusion process with laser as energy source.

2.2 Selective Laser Melting

2.2.1 Working principle

Selective laser melting (SLM) means a selective interaction of a laser beam melting successive layers of metallic powder and consolidating the part, resulting in non-equilibrium microstructures normally seen in rapid solidification processes [2-4, 7]. Due to the additive and layer-wise production, the SLM process may produce geometrical features that are not possible by using conventional production routes [2]. The process is associated to fully melting the powder in a protective atmosphere (Ar or N_2), producing parts with density ≥ 99% [3, 4]. Another important feature of SLM is the resolution: The powder layer thickness is in the range of 10-50 µm and the thinnest possible dimension is 75-100 µm, with the possibility to manufacture thin-walled structures [14].

The process requires the basic steps: model design, machine set-up, operation, powder recovery, and base plate removal. The building process starts with laying a thin layer of metal powder with a recoater (also known as roller or scraper) on a substrate plate in a building chamber (Figure 2.2) [38, 39].

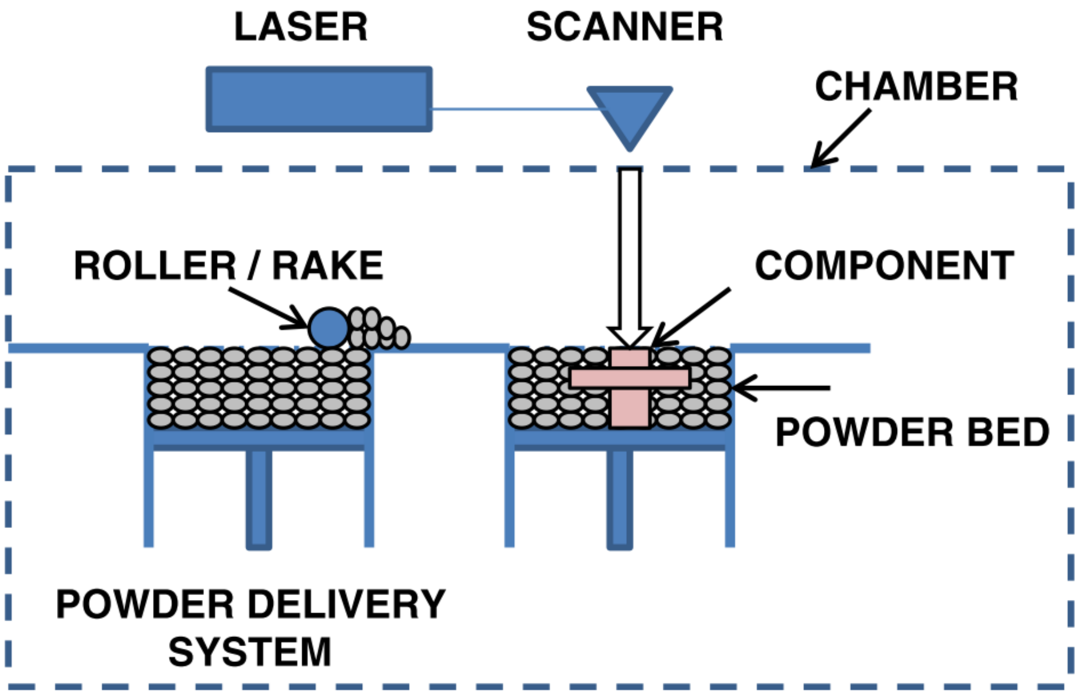

Figure 2.2. Illustration of a selective laser melting system [38].

After spreading the powder on the substrate, a high energy density laser beam is used to selectively melt the part geometry according to the CAD model. The laser beam sources predominantly used in selective laser melting are solid fiber lasers in continuous wave mode, with wavelength of 1060 nm - 1080 nm in the near infrared. The laser and scanner are basically an optical system with a set of lenses and a scanning mirror (galvanometer) [7]. After melting a layer, the building plate is lowered vertically by means of a lifting platform at a distance corresponding to a pre-defined layer thickness. A new layer of metallic powder is spread over the base plate with the recoater, keeping the laser focal distance constant. The laser then melts one more cross section of the model. The process repeats until the part is formed with the desired dimensions and hundreds or even thousands of layers of powder may be melted depending on the thickness of each layer and part geometry [2, 3, 39].

The main challenges faced in SLM are high temperature gradients and melt pool stability. Thermal gradients result in the build-up of thermal stresses and considerable levels of residual stress in the parts, which can lead to delamination and distortion [2, 4, 14]. Therefore, it is common to apply post-processing stress relief heat treatment. Also, due to the superficial aspect of the pieces, finishing operations are frequently inevitable [3, 4]. The stability, dimensions and behavior of the melt pool is to a great extent decisive to porosity and surface roughness, in addition to the roughness created by the layer-wise building (i.e. the staircase effect). The presence of dissolved gases in the metallic powder, laser opacity in relation to the surface roughness of the material and the rapid melting of the powder layers at room temperature may also lead to porosity formation in the components manufactured by selective laser melting [14].

Hence, it is important to understand the relationship between processing parameters and the solidification and metallurgical mechanisms when processing a metallic material by selective laser melting [39]. The main parameters of the SLM process are laser power, diameter of the laser beam (spot size), scanning parameters (scanning speed, distance between tracks or hatching distance and scanning strategy), layer thickness, properties of the material (surface tension, thermal conductivity and solidification range), powder characteristics (flowability and packability), and atmosphere of the melting chamber [14]. It is known that the SLM processing parameters are material and device-specific, and have significant influence on the solidification, phase transformation and the resulting microstructures and mechanical properties of the parts [37, 40]. In addition, the densification is a fundamental property that influences internal integrity and mechanical properties of parts processed by selective laser melting [4]. Therefore, a brief description of the SLM main processing parameters is presented in the next section.

2.2.2 Parameters and optimization factors

Selective laser melting requires powder characteristics which are important for ensuring reproducibility and repeatability. Metal powders used in SLM are assumed to be nominally spherical with narrow particle size distribution, in order to assure proper flowability and achieve homogeneous spreading of the powder, as well as good packing characteristics for the formation of a highly packed powder layer [41]. The main characteristics of the powder for SLM are particle size and shape, surface morphology, composition and internal porosity. These powder characteristics impact the bulk material properties of the fabricated component such as density and porosity [42, 43]. The nominal particle size distribution of powder used in SLM is 10–60 μm and it is generally accepted that spherical particles improve flowability and apparent density. Smooth particle surfaces are better than surfaces with satellites or other defects [42]. In addition, the initial powder composition is very important in determining the chemistry of final parts [2]. Porosity in the powder feedstock is another important feature of gas-atomized powder, since inert gas may be trapped in the particles during production. This entrapped gas is transferred to the part, due to rapid solidification, and results in powder-induced porosity in the fabricated material [11].

The main atomization techniques for producing powders suitable for selective laser melting are gas atomization (GA), rotary atomization (RA), plasma rotating electrode process (PREP), and plasma atomization (PA). Gas atomization is the main technique used to produce powder of Ti and Ti alloys for selective laser melting (Figure 2.3a) [44]. The risk of oxidation is reduced by using an inert gas, such as argon or nitrogen. The process has the ability to produce highly spherical powder particles with a narrow particle size distribution and smooth surface. The presence of satellites is commonly seen and is inherent to the process, and it is related to particles adherence to the surfaces of larger ones due to collisions during atomization (Figure 2.3b) [41, 44-46].

Another important variable in selective laser melting is the build chamber atmosphere. The build chamber atmosphere strongly affects chemistry, processability and heat transfer of the part [2, 11]. Most metal powders tend to oxidize and collect moisture when exposed to air, especially at high temperatures. It is known that oxygen uptake and the formation of oxide layers are undesired effects as they influence the powder flow behavior, impact the melt pool and consequently change the bulk material composition and the mechanical properties of the parts [47].

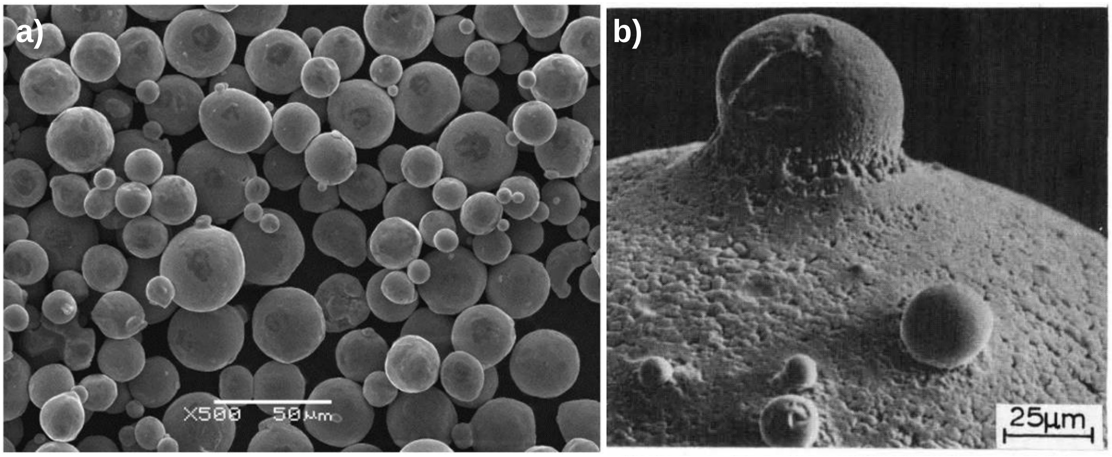

Figure 2.3. Typical particle morphology and size of a Ti-6Al-4V powder [46] (a) and particle surface with 'satellite' (b) [45].

Furthermore, selective laser melting is a complex transformation process, which follows a process routine from a “line” to a “layer” to a “bulk” [4]. The process begins with a single line scanning, in which laser power, (P_l), and scanning speed, (v_s), are the most important parameters. The overall quality of the tracks (uniformity and continuity) is assessed and the track width is related to the laser power/scanning speed combination used. After scanning multiple lines, a single layer is formed, which introduces another important parameter, hatching distance, (h_s), defined as the distance between two adjacent tracks. In addition, a suitable layer thickness, (l_z), needs to be selected, which is related to the size of the powder particles and part details [48] and, therefore, the layer-by-layer consolidation yields a bulk component (Figure 2.4). Another important parameter is the scanning strategy used during processing, which is the path the laser follows to melt the part cross section in a layer [4, 38, 40].

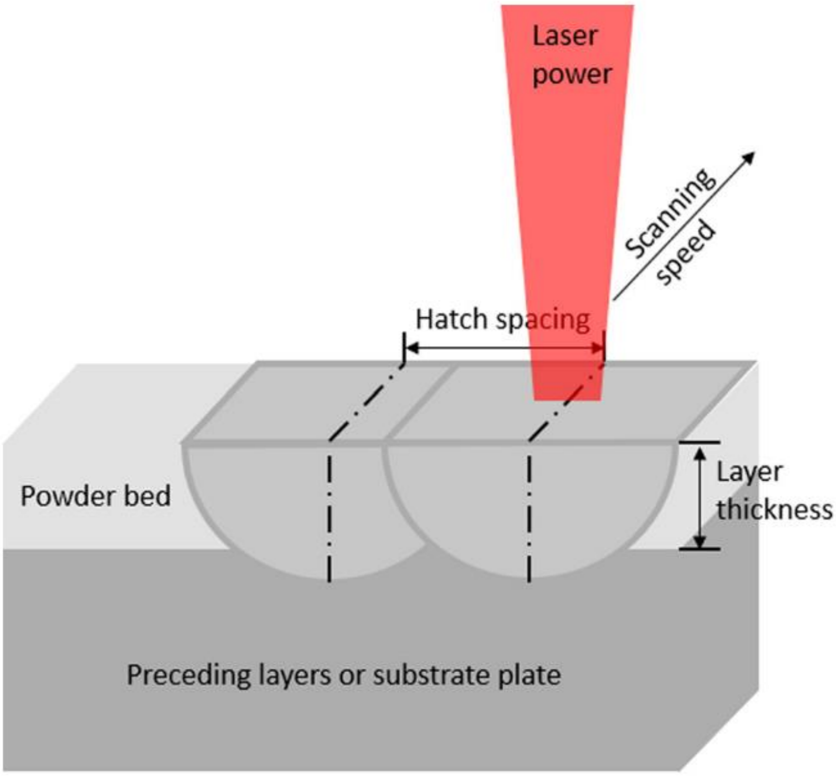

Figure 2.4. SLM process parameters: laser power, scanning speed, hatch spacing, and layer thickness [39].

The suitable processing window for a material is normally very narrow, making it difficult to optimize the processing conditions. The individual parameters P_l, v_s, h_s, and l_z have great influence on densification of the part, besides also showing influence on each other [4]. In order to evaluate the combined effect of these parameters the volumetric energy input, E_v [J/mm³], is defined [39, 49]:

$$E_v = \frac{P_l}{v_s \cdot h_s \cdot l_z} * 10^{-9},$$

where P_l is the laser power (W), v_s is the scanning speed (m/s), h_s is the hatching distance (µm), and l_z is the layer thickness (µm).

The laser power is one of the most important parameters of SLM [50]. The relationship between laser power and scanning speed is material-dependent and it is important for process parameter mapping as only certain combinations will result in dense material [48]. In addition, the part density of a selective laser melted part is depended on the applied volumetric energy input. It is generally recognized that high energy densities are desirable to obtain fine microstructure and improved mechanical properties in the final parts. It is also known that too low energy input may result in unmelted material and thus reduced density by the formation of irregular-shaped voids, while too high energy input may lead to higher melt pool dynamics and reduced density originating from pores formed due to entrapped gas. Therefore, it is difficult to obtain a general set of optimum individual process parameters for all metal AM processes, and ‘one size fits all’ is not possible [7, 37].

Hatching distance is another important parameter when producing bulk parts by selective laser melting [39]. A component fabricated by SLM is built layer by layer, which is exactly the overlapping resultant of neighboring tracks. To ensure a uniform in-layer fusion, two subsequent laser tracks must overlap, i.e., the melt pool width should be at least 1.5–1.6 times larger than the hatching distance (i.e., 50-60% of overlapping between adjacent tracks) [52], as poor hatching distance often results in porosity in built parts as adjacent melt lines do not melt together completely [39, 40, 52].

An important limitation of the volumetric energy input equation is that it does not consider the scanning strategy, which is the path that the laser beam follows during selective melting [53]. The scanning strategy may have a similar impact on heat flow as the energy input, depending on how the strategy allows cooling between each layer [39, 53]. The scanning strategy for a given build may be adjusted by layer or by part. Unidirectional, bidirectional and island scanning strategies, normally rotated by an angle between each layer (cross-hatching), are the most used scanning strategies in selective laser melting (Figure 2.5) [2-4, 53].

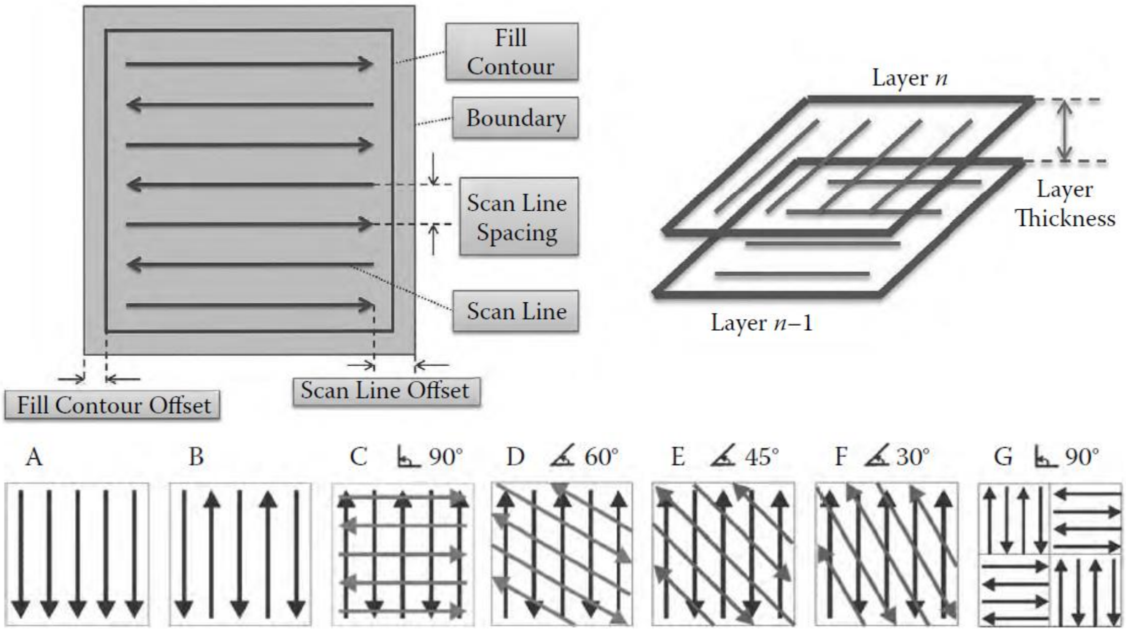

Figure 2.5. Scheme of layer deposition in selective laser melting, with some examples of scanning strategies: A – unidirectional; B – bidirectional; C-F – alternating bidirectional, varying the angle between layers (cross-hatching); G – island or chessboard scanning strategy [3].

2.2.3 Solidification aspects of selective laser melting

A wide range of non-equilibrium phenomena takes place in SLM [3, 7, 8, 11-14, 39]. It is recognized that the properties of the parts depend basically on the laser beam-metallic powder interaction (Figure 2.6), which occurs in a short period of time, resulting in a fast melting-solidification cycle. The resultant heat transfer and fluid flow affect the size and shape of the melt pool, the cooling rate and phase transformations [3, 14].

In the SLM process, radial thermal gradients between melt pool centerline and liquid-solid interface are in the order of 10^2-10^4 K/mm. Because of the rapid scanning of the laser beam the temperature contours are elongated behind the heat source and compressed in front of the beam (Figure 2.7a) [54]. Inside the melt pool, the temperature is highest near the heat source axis and lowest near the boundary of the pool. This non-uniform temperature results in a surface tension gradient inside the melt pool, which leads to a flow of molten metal [11]. Therefore, thermal gradients stimulate melt movement, leading to a heat flux opposite to the thermal gradient due to a surface tension gradient on the top surface of the melt pool resulting from the spatial variation of temperature, an effect known as Marangoni [55, 56]. This effect may turn into a dominant convective mechanism in the melt pool and has a major effect on the temperature distribution in the liquid, heating and cooling rates, solidification pattern, and microstructure and properties of the build [57].

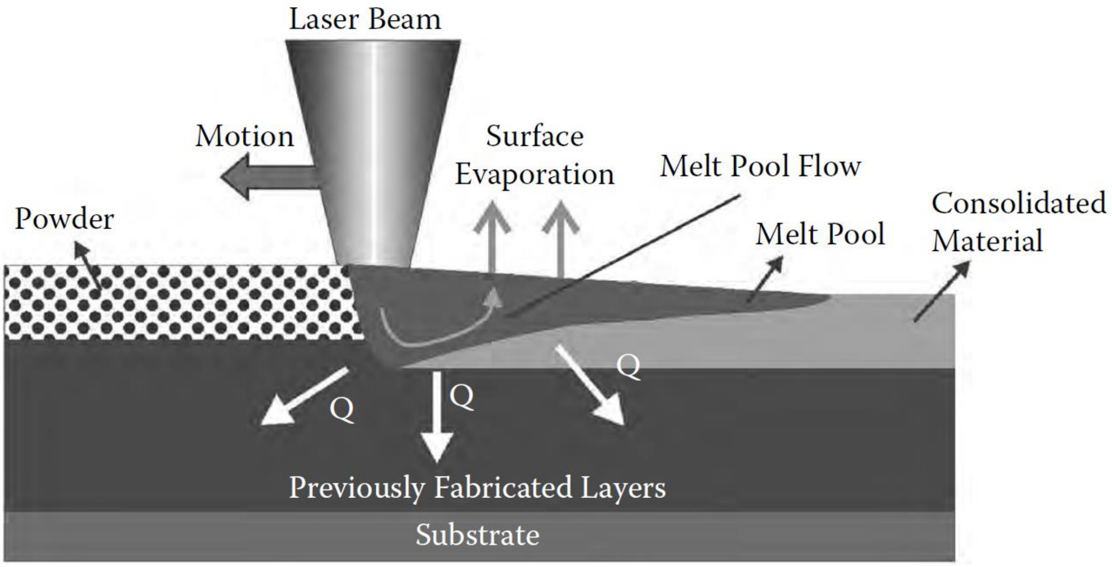

Figure 2.6. Laser beam-metallic powder interaction in selective laser melting [3].

Another important aspect is the peak temperature in the melt pool, which may be several hundred degrees higher than the *liquidus* temperature of the alloy. It is known that the substrate plate acts as a heat sink, especially in the first layers' deposition and, therefore, heat transfer occurs by conduction. As the part is built, the conductive heat transfer through the substrate decreases progressively and the peak temperature for the upper layers increases. Thus, heat transfer from the melt pool into the substrate becomes more difficult with increasing distance from the substrate, resulting in larger melt pool and higher peak temperatures in the upper layers (Figure 2.7b) [54]. This behavior may lead to a microstructural gradient, both in grain size and structure, between the bottom and top of a part along the building direction. Basically, the different thermal histories of different layers of the part may lead to variation of microstructures along the height direction, as the conduction, convection, and radiation conditions change [4].

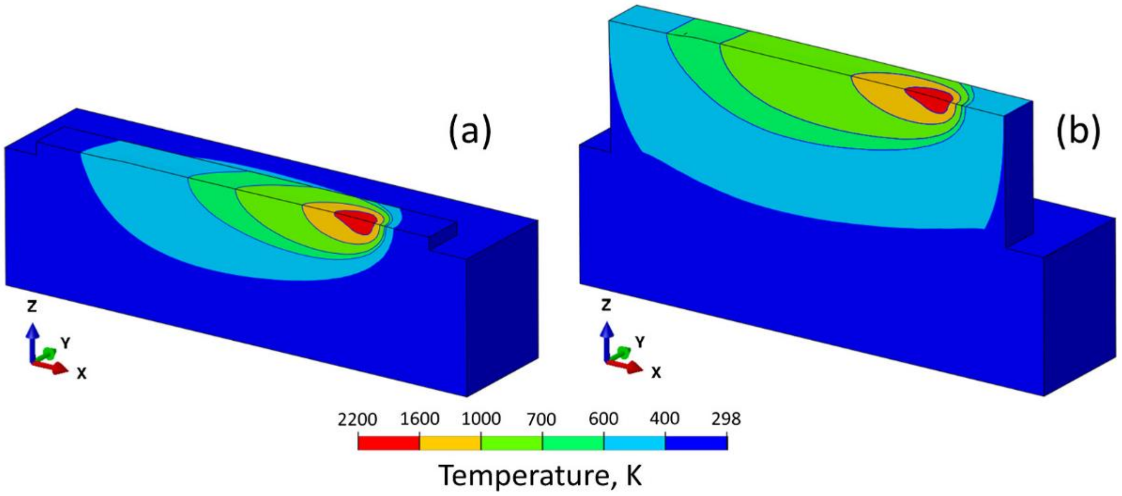

Figure 2.7. Temperature distribution simulation on a laser direct energy deposition process of a nickel Inconel 718 powder deposited on a substrate of same material, with laser power of 300 W and scanning speed of 15 mm/s, during the deposition of (a) 1st and (b) 10th layer. Laser beam scanning direction is along the positive x-axis [54].

Selective laser melting involves several mechanisms of phase transformations. From the solidification point of view, the process has similarities to high energy welding processes, due to the localized concentration of heat input, moving melt pool and high cooling rates involved [11, 14]. The layer-by-layer process deposits metal that has the same chemical composition as the previous layer. This eliminates the need for nucleation and allows growth to occur with no activation energy barrier: If the temperature drops below the liquidus, crystals grow epitaxially from the substrate [11, 58, 59].

Cooling rates in SLM are higher than 10^4 K/s, resulting in microstructures with fine grains and precipitates, enhanced chemical homogeneity and solid solubility, and possibly metastable phase formation [3]. The solidification takes place in a small localized volume and the resulting microstructure is affected by repetitive thermal cycles. The previous deposited layer is thermally affected by melting of subsequent layers, resulting in complex thermal cycles, which in turn makes it difficult the accurate forecasting of the microstructure, especially for alloys with multiple possible phase transformations as Ti-based alloys [3, 14].

According to the solidification theory, once the solid phase nucleate, the stability of the solidification front determines the type of the resulting microstructure. For pure metals that have a single melting temperature, the stability is determined by the thermal gradient in the melt. Depending on the sign of the thermal gradient in the liquid phase, (G_L), either a planar solidification front or an unstable solidification front may occur. Alloys, on the other hand, have a solidification range rather than a specific melting point, except alloys with solute content corresponding to an invariant reaction (e.g. eutectic alloys), which causes alloy elements to redistribute between solid and liquid. The solid/liquid interface morphology of an alloy is dependent on solute diffusion in the liquid phase, besides the thermal gradient in the liquid. Due to the absence of convective heat transfer and limited diffusion of solute in the liquid as the solid/liquid interface advances, there is a solute accumulation in front of the interface, resulting in a compositional gradient. This compositional gradient, in turn, leads to a gradient in the equilibrium liquidus temperature, (G_C), an effect known as constitutional undercooling. On this way, even with positive thermal gradients, the constitutional undercooling may destabilize the planar solidification front, causing a cellular-dendritic solidification [58-63].

The constitutional undercooling, planar solidification front instability and cellular or dendritic structure formation are based on the condition that the thermal gradient in the liquid phase, (G_L), is lower than the gradient in the equilibrium liquidus temperature due to the compositional gradient, (G_C) (Figure 3.8). On this sense, the following evaluation may be performed:

- The instability on the planar solidification front increases as the actual thermal gradient in the liquid in front of the interface, (G_L), is reduced.
- For a given thermal gradient (G_L), a higher solidification rate, (R), and, therefore, higher compositional gradient in front of the interface, destabilizes the planar solidification front.

Regarding the two mentioned parameters, the thermal gradient in the liquid G_L has influence on the solidification front stability and it is material dependent: it is higher for low conductive materials (e.g., Ti and its alloys). It is also dependent on the process, as it is known to be higher for high energy input processes such as laser or electron beam melting. The solidification rate, R, defined as the rate at which the solid/liquid interface moves, is directly related to the heat source speed (laser scanning speed, v_S, in the case of SLM). It influences the solidification substructure scale (e.g., interdendritic spacing), the solute distribution and constitutional undercooling [61, 63]. The ratio between the thermal gradient in the liquid and the solidification rate, (G_L/R), is the parameter which defines the morphology of the solidification microstructure of the alloys. Thus, the solidification microstructures may be planar, cellular, columnar dendritic or equiaxed dendritic, with decreasing G_L/R values (Figure 2.8) [11].

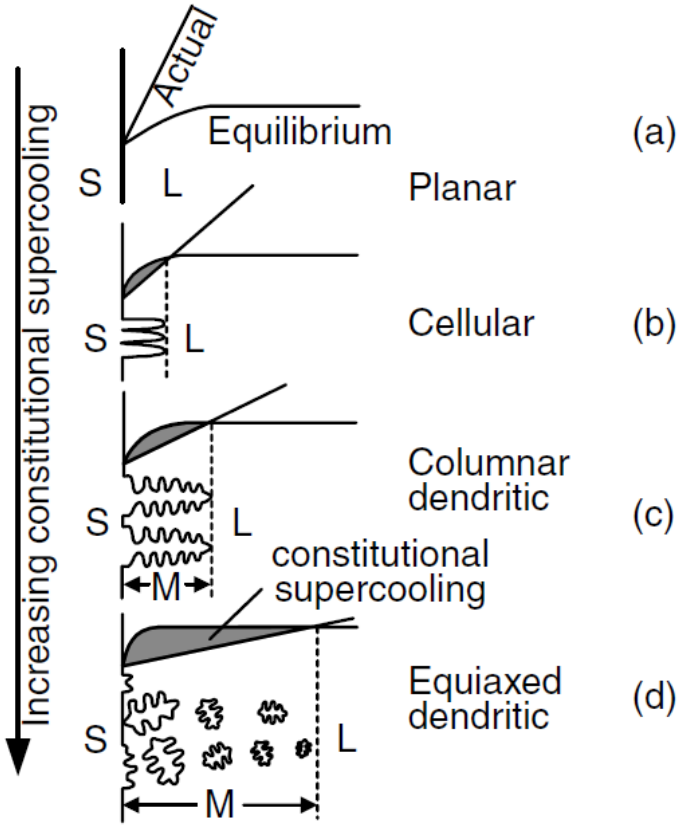

Figure 2.8. Effect of the constitutional undercooling on the solidification mode: (a) planar; (b) cellular; (c) columnar-dendritic; (d) equiaxed-dendritic. S, L and M mean solid, liquid and mushy zone, respectively [58].

Another important relationship between thermal gradient and solidification rate is the cooling rate, ($\dot{T} = G_L R$). The cooling rate has direct influence on the solidification microstructure scale. In casting processes, the cooling rate is in the range 10^{-2}-10^{2} K/s, while in rapid solidification process such as selective laser melting, the cooling rate is in the range of 10^{4}-10^{7} K/s, depending on the processing parameters [3]. It is known that the scale of the solidification microstructures decreases with increasing cooling rate [11].

Despite the complexities of AM, the solidification structure is mainly determined by the parameters thermal gradient G_L, solidification rate R, and cooling rate $\dot{T}$. Efforts to correlate the processing parameters with these key solidification parameters may efficiently promote the understanding of the relationship between process and structure. Plotting a solidification map, which relates morphology and scale of the solidification structure to the solidification (growth) rate and thermal (temperature) gradient, may indicate the resultant microstructure of the build (Figure 2.9) [11]. The most widely observed solidification microstructures in the AM components are cellular and columnar-dendritic structures [11], and equiaxed grains are rare in polycrystalline materials processed by selective laser melting due to the high temperature gradient, which is on the order of 10^{6} K/m [64-69]. However, equiaxed grains may still form depending on the constitutional undercooling near the solidification front [11, 70, 71] and heterogeneous nucleation on partially melted powders or second phase added particles [69].

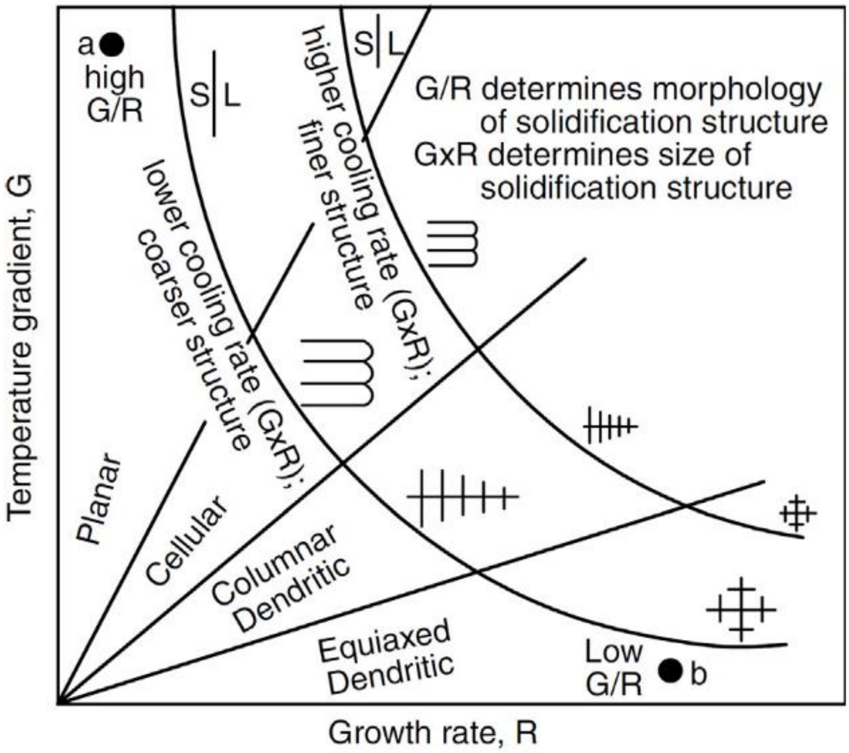

Figure 2.9. Solidification map correlating the thermal gradient and solidification rate based on G/R e $\dot{T} = GR$ parameters, with morphology and size of solidification microstructure [58].

2.2.4 Microstructure of selective laser melted parts

Previous studies have reported results of solidification microstructure of parts manufactured by selective laser melting. In the case of the Ti-6Al-4V alloy (wt%), the microstructure shows columnar prior β grains that contain acicular martensite (Figure 2.10a). The melt pools were not visible in the micrographs of the Ti6Al4V samples. However, the melt pools were clearly observed in a sample of 316L stainless steel produced by SLM (Figure 2.10b) [36]. In some other systems, e.g. AlSi10Mg, 316L, 18Ni300 maraging steel, and Inconel 718 the melt pool boundaries were identified in metallographic prepared samples of the building direction cross-section (Figure 2.10c-f) [36]. In a higher magnification view (insets), a cellular structure is observed for the alloys. For AlSi10Mg alloy (Figure 2.10c), the intercellular zone consists of an Al–Si eutectic, but for all other materials, the contrast is provided by a small amount of microsegregation [73, 74]. The fine scale of the cellular structure is due to the high cooling rates during metal AM manufacturing, which can reach 10^6 K/s in SLM [69].

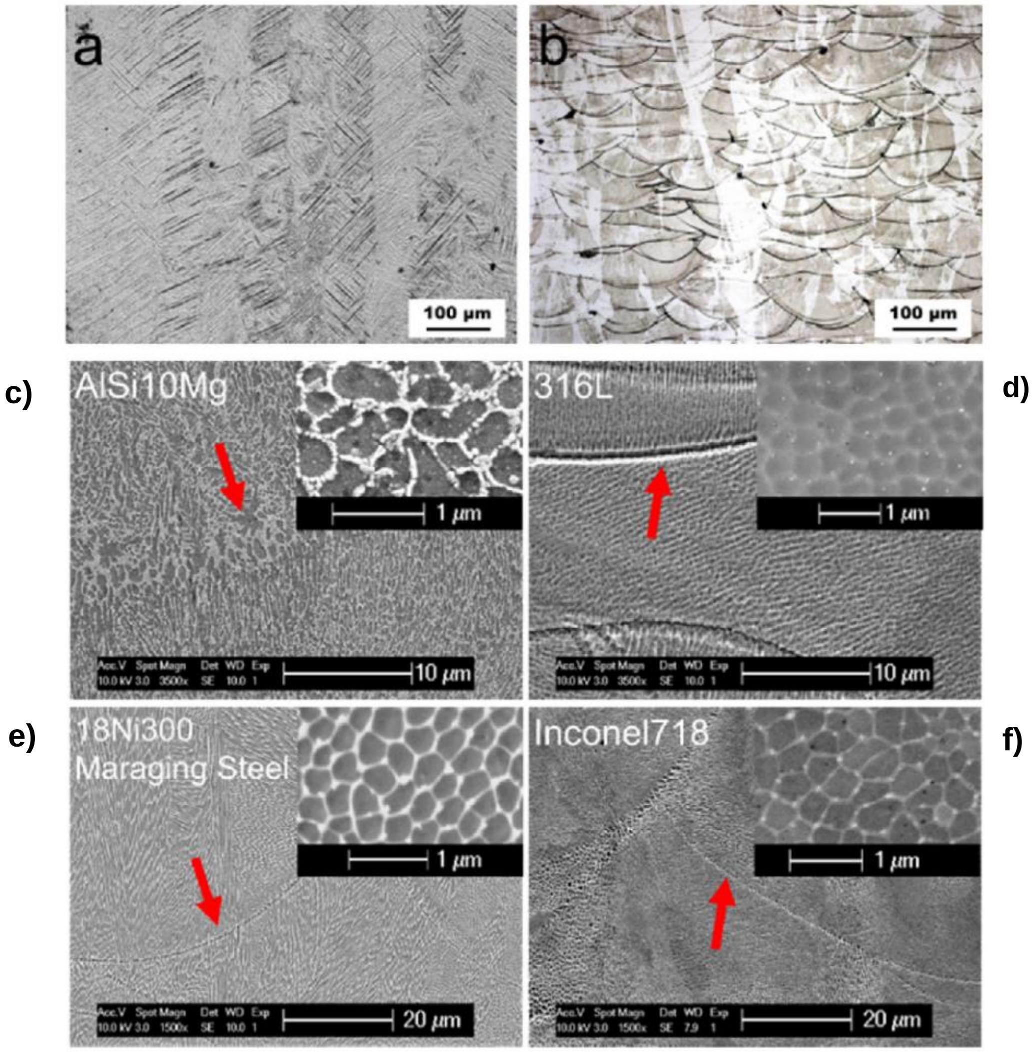

Figure 2.10. (a) The columnar microstructure in SLM of Ti6Al4V and (b) the visible melt pools in SLM of 316L in the building direction and side views of the cellular microstructure of SLM samples of (c) AlSi10Mg, (d) 316L stainless steel; (e) 18Ni300 maraging steel, and (f) Inconel 718. The insets are close-ups of the top view [36].

The grain grows in selective laser melting during solidification from previously deposited layers, and ultimately determines the crystallographic texture of the structure through partial or complete melt-back of the previously formed underlying layer [67]. Columnar grains grow from the boundary of the melt pool towards the center. For polycrystalline materials, the grain growth direction is parallel to the maximum heat flow direction, which is normal to the solidifying surface of the melt pool [59, 75]. Figure 2.11 shows grain morphology and crystallographic texture of samples produced by SLM and EBM.

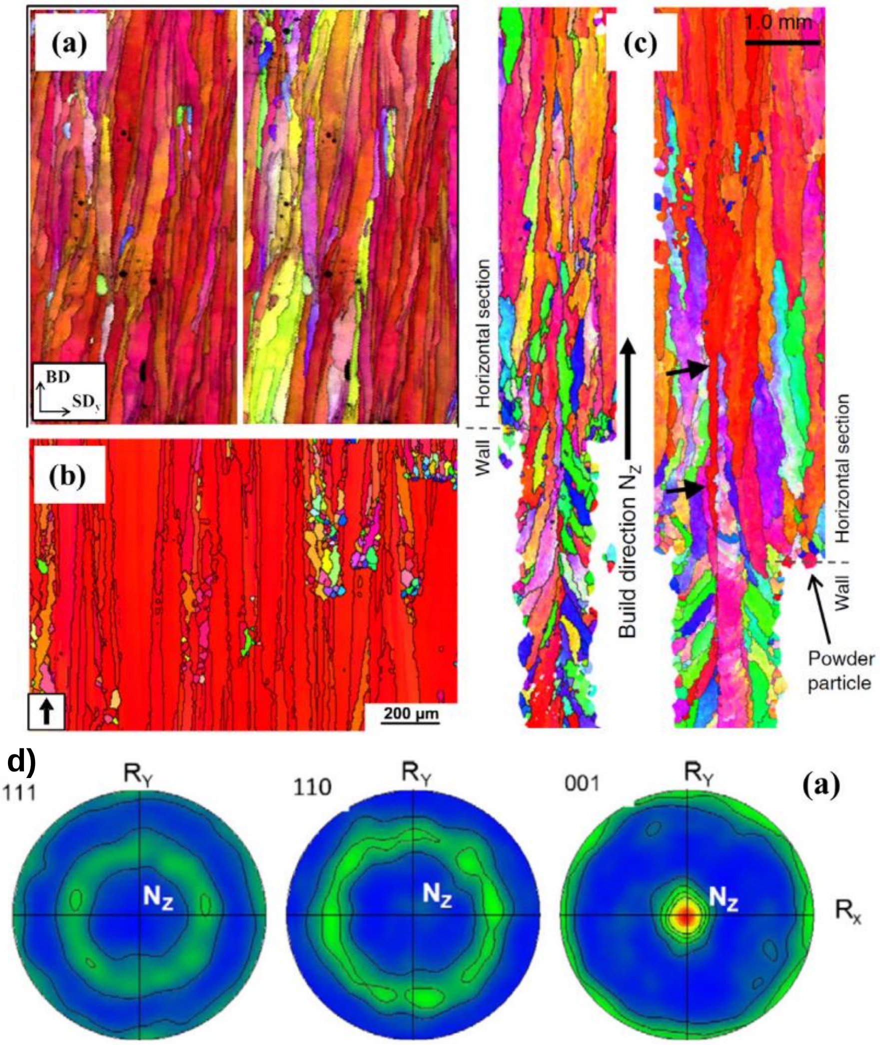

Figure 2.11. Grain orientations closely aligned with the <001> building direction in samples made by SLM. (a) high-silicon steel (6.9%wt. Si) [78], (b) Inconel 718 [79], (c) Ti-6Al-4V [68]. (d) Pole figures depicting reconstructed β <001> fiber texture for Ti-6Al-4V manufactured by electron beam melting (EBM) [68].

Competitive growth occurs among dendrites with various crystallographic orientations in the polycrystalline materials [58, 59, 75]. Dendrites with easy-growth directions aligned closely with the maximum heat flow direction at the solid/liquid interface achieve competitive growth during the solidification process. The growth direction and velocity of the solidification structure of the AM component are dependent on both crystallographic orientation and local heat flow direction [11]. The preferential growth direction for cubic crystals is the <100> direction, and <1010> for hexagonal crystals. The direction of grain growth may closely align with the <001> build direction, and it has been observed for several systems produced by SLM (Figure 2.11a-c) [68, 75-80]. Besides the solidification texture, microstructural banding is also commonly observed in samples produced by SLM. The former is normally seen as fiber texture of grains aligned with the building direction and originates from the fact that in bulk sections the grains grow up through many layers, which favors the development of a coarse grain structure (Figure 2.11d). The latter is also observed on the building direction of the part, but it is related to repetitive thermal cycles on consecutive layers [14].

2.3 Selective Laser Melting of Ti-based Alloys

Antonysamy (2012) investigated the influence of processing parameters on additive-manufactured parts of Ti-6Al-4V (wt%) alloy [14]. The author produced samples by selective laser melting in an EOSINT M270, from Ti-6Al-4V powder with particle diameter in the range 10 e 45 µm, on a base plate of same material. The parameters used were laser power of 170 W, scanning speed of 1.25 m/s, laser beam diameter of 200 µm, layer thickness of 30 µm, and hatching distance of 100 µm. From the obtained microstructure, it was observed prior β columnar grains formed by epitaxial growth (Figure 2.12a). The author also used a finite difference element method to simulate the melt pool and solidification conditions and the depth of the melt pool could be assessed (Figure 2.12b). The melt pool shape was obtained by the simulation, and a teardrop melt pool was observed (Figure 2.12c), related to the high scanning speed and low thermal conductivity of the Ti-based alloy [14].

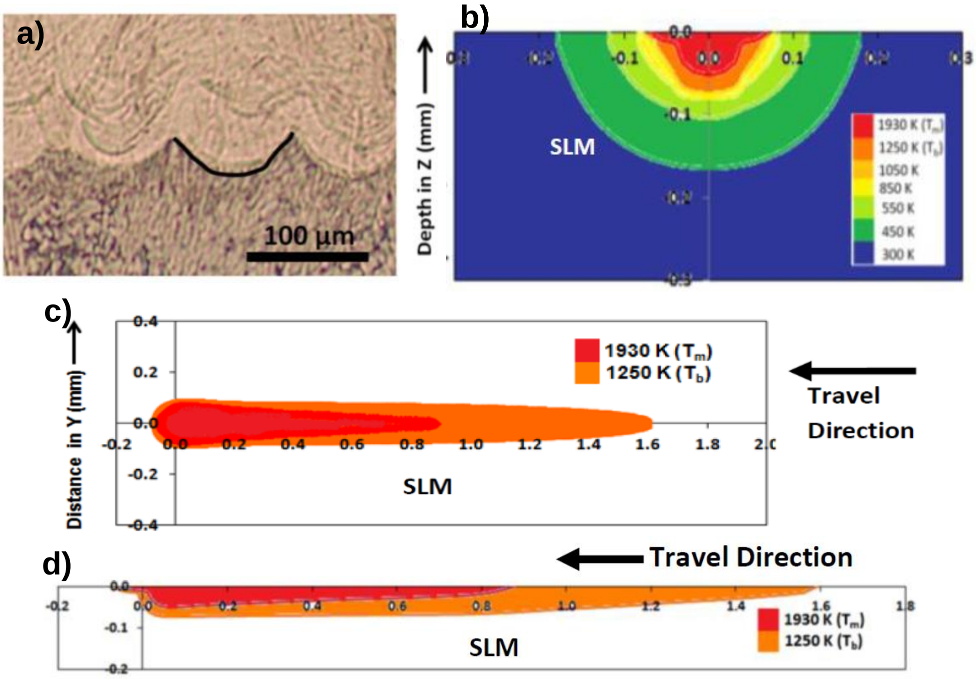

Figure 2.12. Melt pool in a Ti-6Al-4V sample manufacture by selective laser melting (a), with isotherms obtained by computational simulation (b). Melt pool shape in upper view (c) and along the centerline (d), with the *liquidus* (red) and *β-transus* temperature (orange) [14].

A solidification map was plotted, correlating the thermal gradient and solidification rate to the microstructure morphology (Figure 2.13). The calculated values of the solidification parameters were: G_L = (0.67-2.35) x 10^4 K/cm; R_{max} = 1.25 m/s; cooling rate, $\dot{T}$ = (0.73-8.37) x 10^5 K/s; G_L/R_{min} = 8 x 10^6 K.s/m^2. The planar solidification front instability criterion was defined as $G_L/R < 5 \times 10^9$ K.s/m^2. According to the simulation, it was observed that the microstructure in the selective laser melting process resulted in an initially planar solidification structure, with a transition from columnar to equiaxial structure. The author also reported results obtained by electron back-scattered diffraction. The columnar grains presented preferential growth in the <001> direction, parallel to the building direction, i.e., aligned with the deposition direction, but opposite to the heat-flux [14].

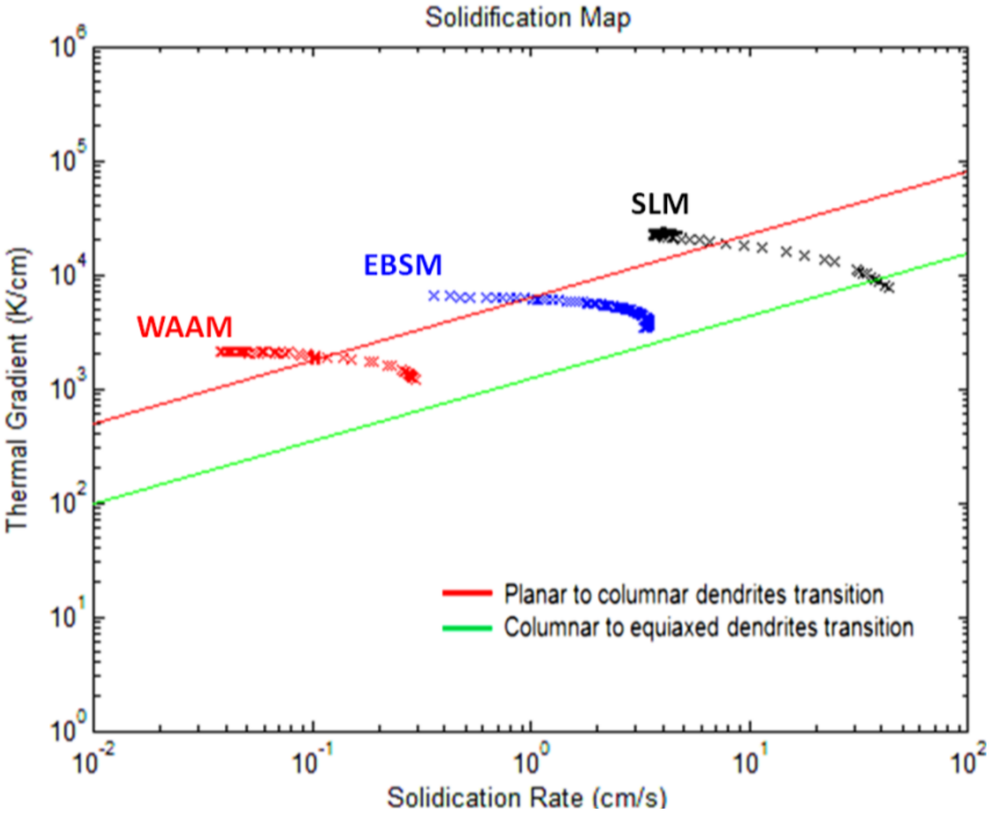

Figure 2.13. Solidification map for Ti-6Al-4V alloy, obtained by computational simulation, additive-manufactured by wire-arc additive manufacturing (WAAM), electron-beam selective melting (EBSM) and selective laser melting (SLM) [14].

Thijs et al. (2010) investigated the microstructure development of a Ti-6Al-4V (wt%) alloy manufactured by selective laser melting and the influence of the process parameters. The powder was produced by plasma atomization, with a particle size of 5-50 µm (d_{50} = 34.4 µm). The parameters used were laser power of 42 W, scanning speed of 50, 100 e 200 mm/s, layer thickness of 30 µm, and hatching distance of 50, 75 e 100 µm. Three scanning strategies were tested: unidirectional, bidirectional and cross-hatching, and samples with cuboid geometry (5 x 10 x 5 mm^3) were produced. The micrographs of the samples were presented, and according to the authors, samples manufactured with a volumetric energy input of 93 J/mm³ presented relative density of 99.6%. A herringbone structure was observed, and it is related to the bidirectional scanning strategy (Figure 2.14a). It was observed grains with 100 µm up to millimeter of length, extending through several layer thickness, related to an epitaxial growth. The grain width was 75 µm, equal to the hatching distance used (Figure 2.14b). According to the authors, the microstructure was formed by α' martensite laths, due to the high cooling rate imposed by SLM. The Vickers hardness was reported as (409 ± 35.9) [8].

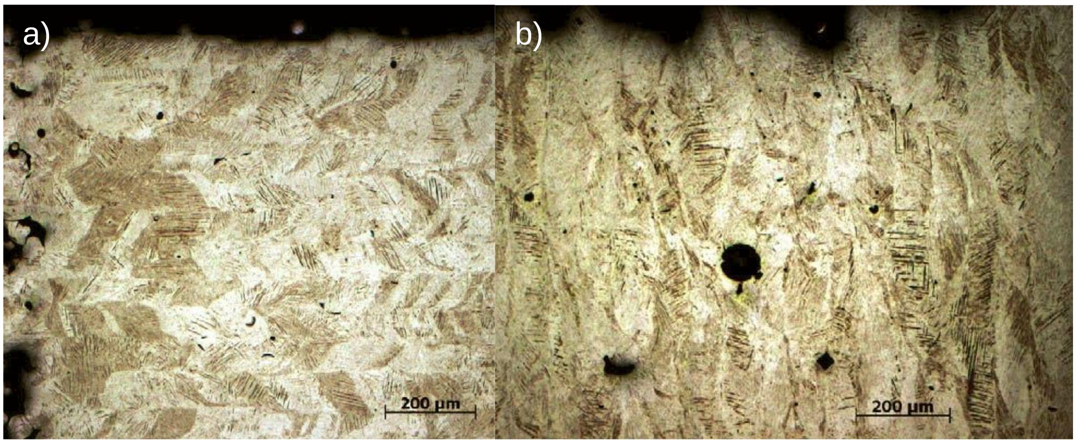

Figure 2.14. Optical micrographs of Ti-6Al-4V (wt%) samples manufactured by SLM: (a) laser scanning cross section; (b) building direction plane. Processing parameters: laser power, 42 W; scanning speed, 200 mm/s; layer thickness, 30 µm; hatching distance, 75 µm; volumetric energy input, 93 J/mm³, and bidirectional scanning strategy [8].

Saedi et al. (2017) studied the process-microstructure-property relationship of a $Ni_{50.8}Ti_{49.2}$ (at%) alloy processed by selective laser melting. The authors also performed a systematic study on the effect of aging temperature and time on shape memory and pseudoelastic effects of samples submitted to aging heat-treatment. Therefore, cuboids with dimensions 12 x 6 x 6 mm³ were manufactured by SLM with a NiTi powder (d_{50} = 50 µm). The micrographs of the as-built samples are presented and compared to as-cast sample (Figure 2.15). It was noticed that the applied scanning strategy produced a rather regular pattern of melt pools with chess-like grains or checker grains and width of 100-

140 µm, as observed in the laser scanning cross section (Figure 2.15c). Perpendicularly to this plane, in the building direction cross section, columnar grains are observed (Figure 2.15d) [80].

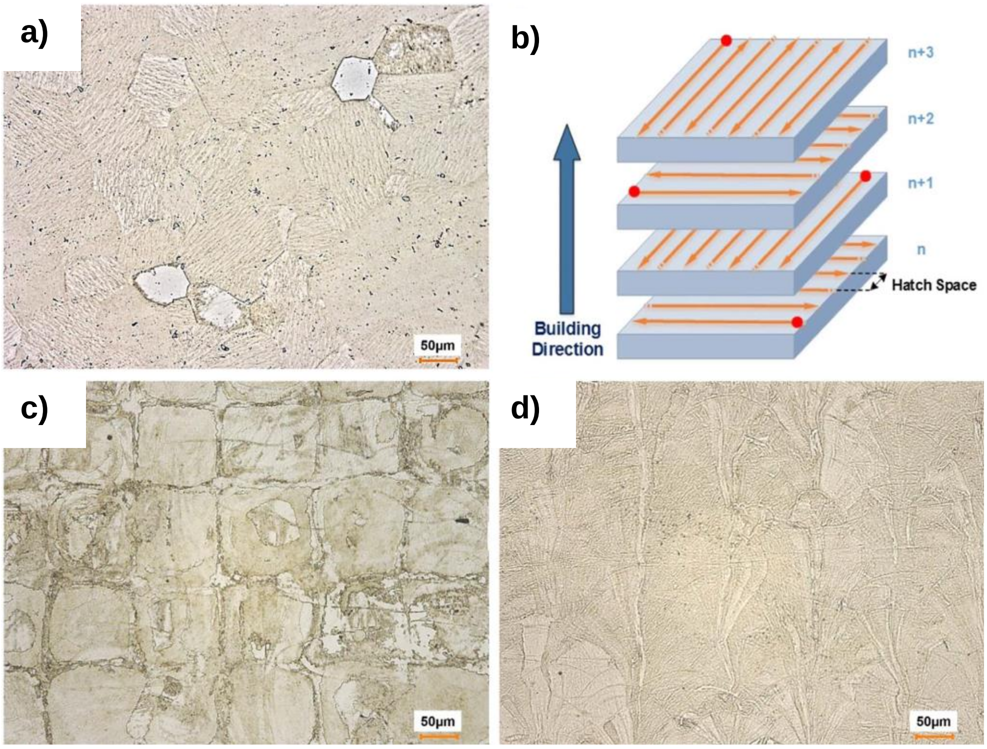

Figure 2.15. Optical micrographs of as-cast $Ni_{50.8}Ti_{49.2}$ (at%) (a); scanning strategy used in the SLM experiments (b); scanning direction cross-section (c) and building direction cross-section [80].

The authors reported that, although the samples manufactured by SLM shown lower mechanical resistance than the as-cast samples (Figure 2.16a), the strong [001] texture in the building direction improved the pseudoelasticity, especially in the samples submitted to aging heat-treatment (Figure 2.16b and c). The cyclic stress-strain curves shown that selective laser melted samples, submitted to aging heat-treatment at 350 °C for 1 h (Figure 2.16b), and 600 °C for 1.5 h (Figure 2.16c), presented pseudoelasticity of up to 5.5% at room temperature [80].

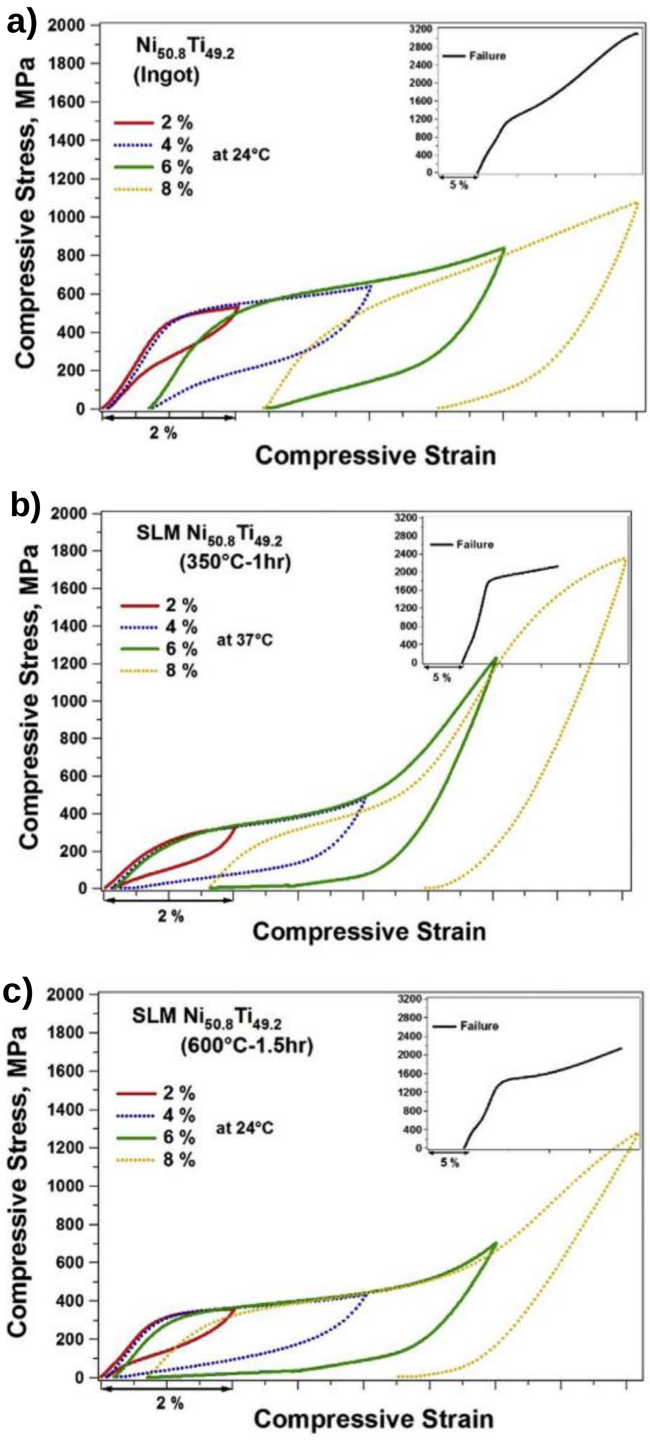

Figure 2.16. Pseudoelasticity of $Ni_{50.2}Ti_{40.8}$ (at%) samples: (a) as-cast; sample manufactured by SLM and submitted to aging heat-treatment at 600°C for 1.5 h at 350 °C for 1 h (b) and at 600°C for 1.5 h (c) [80].

Fischer et al. (2016) investigated the microstructure of Ti-45Nb (wt%) alloy manufactured by selective laser melting. The Ti and Nb powders were mixed *in situ* during the process. The authors used microtomography to investigate pores distribution in the samples. It was seen that samples manufactured with laser power of 120 W and hatching distance of 100 µm presented more than 19.7% of porosity with unmelted Nb particles (Figure 2.17). Therefore, the authors concluded that the correct parameters selection has a decisive influence on the porosity level of the samples [81].

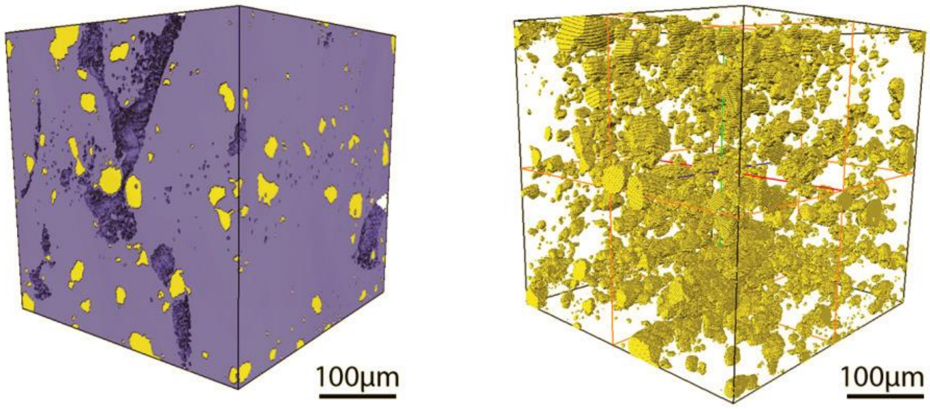

Figure 2.17. Microtomography 3D image reconstruction of a sample of Ti-45Nb (wt%) alloy, with 19.7% of porosity and 20.3% of unmelted Nb particles (yellow) [81].

Schwab et al. (2015) processed by selective laser melting a gas-atomized powder (20-100 µm) of a Ti-45Nb (wt%) alloy, applying three sets of parameters. The samples were produced in SLM Solutions SLM 250HL device, using a Ti-45Nb substrate plate, under argon atmosphere, layer thickness of 100 µm and bidirectional scanning strategy with 74° rotation between layers (cross-hatching). A β single phase structure was observed in the microstructure of the samples with the three set of parameters used. In addition, it was observed some pores with spherical geometry and the samples presented relative density of (99.5 ± 0.5)% (Figure 2.18a). The authors reported that the pores were uniformly distributed over the whole analyzed cross section of the samples, and its spherical morphology is related to entrapped gas in the powder. The micrographs also shown the melt pool boundaries and the solidification structure (Figure 2.18a). According to the authors, the grains growth by epitaxy from previous layers, and a cellular morphology is observed (Figure 2.18b). The grain size was 5 µm of width and 100 µm of length. The Vickers micro-hardness was correlated to the energy input: it was 211 $HV_{0.1}$ for samples processed with 257 J/mm^3 and 192 $HV_{0.1}$ for samples processed with 137 J/mm^3, indicating that the hardness was influenced by the energy input [82].

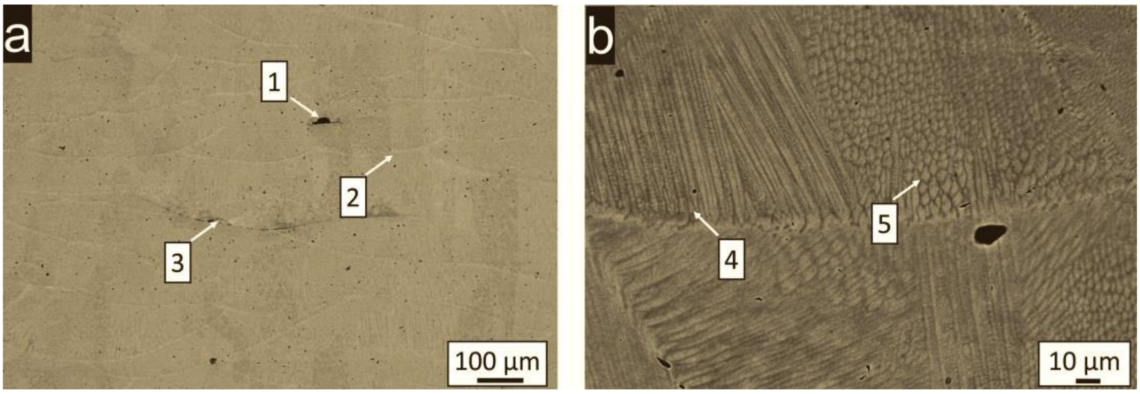

Figure 2.18. Microstructure of a Ti-45Nb (wt%) sample obtained by scanning electron microscope in the back-scattered electrons mode. The SLM parameters used were laser power of 250 W; scanning speed of 35 mm/s, and 50% of overlapping [82].

2.4 Metallurgy of Ti-Nb-based Alloys

The Ti-35Nb-7Zr-5Ta (wt%) biocompatible alloy investigated on the present work is a β-Ti alloy of the Ti-Nb system, which has been considered promising for biomedical applications. In fact, these alloys present low Young's modulus, enabling their application in prostheses. In addition, Ti-Nb-based alloys show the shape memory and pseudoelasticity effects due to a thermoelastic martensitic transformation. Therefore, Ni-free alloys may also be considered for biomedical applications such as coronary stents, among other engineering applications [25].

Baker (1971) firstly reported the shape memory effect in a Ti-35.4Nb (wt%) alloy, and several studies on the system followed since then [83]. Ti-(35-39)Nb (wt%) alloys presented shape memory effect and Ti-(40-41.8)Nb (wt%)

shown pseudoelasticity at room temperature [25, 27]. The Ti-Nb phase diagram of Figure 2.19a present a stable α-β system superimposed by a metastable β-ω system. The Ti-Nb system is isomorphous and Nb exhibits full solid solubility in the BCC β-Ti phase at temperatures higher than the beta *transus* temperature ($T^{\alpha/\beta}$). At such temperatures, either Ti or Nb present body-centered cubic structure (BCC). Adding Nb reduces the α/β transformation temperature, delaying the formation of α phase, since Nb is a β-stabilizer element. The metastable phase diagram of ω and β shows a miscibility gap in β, resulting in a monotectoid type system. A summary of the characteristic transformations of the Ti-Nb phase diagram is shown in Table 2.1.

Table 2.1. Phase transformation of the Ti-Nb system, with respective temperatures and alloy content. Adapted from Bönisch (2016) [84].

	Phase transformation	Type of transformation	Temperature	Nb content	
			°C	wt%	at%
Stable	L ↔ Nb	Melting	2477	100	100
	L ↔ β-Ti	Melting	1668	0	0
	β-Ti ↔ α-Ti	Allotropic	882	0	0
Metastable	$\beta \leftrightarrow \beta_1 + \beta_2$	Critical	513	66	50
	β-Ti ↔ ω-Ti	Allotropic	485	0	0
	β ↔ β + ω	Monotectoid	430	37	23.3

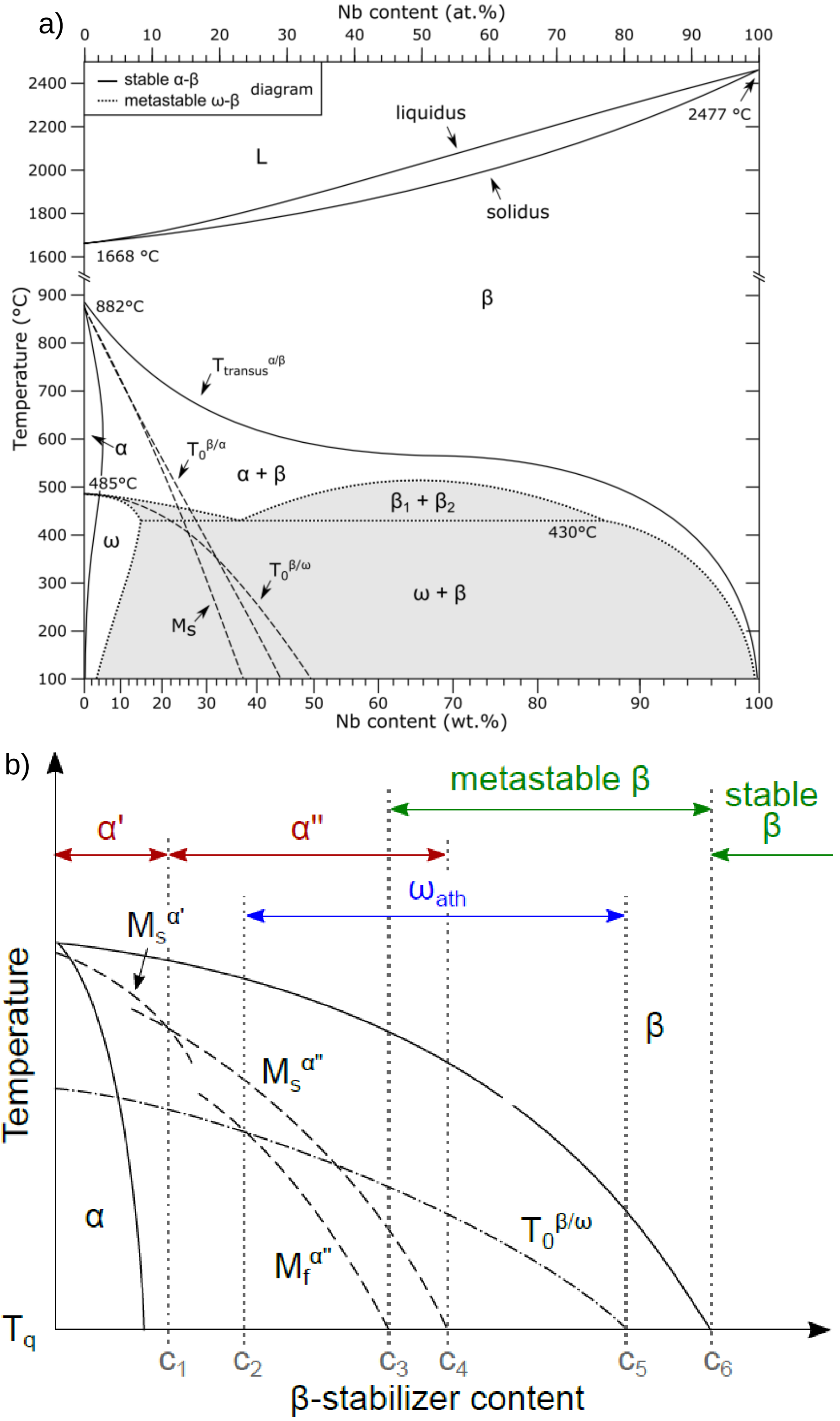

Figure 2.19. (a) Stable and metastable phase diagrams of Ti-Nb; (b) illustration of phase diagram of an isomorphous β-Ti system, with stable α e β phases and metastable α', α" e ω phases, which may be formed in fast cooling conditions [84].

The phase transformation of the Ti-Nb system, with respective alloy content and related temperatures are shown in Figure 2.19b. Metastable phases such as α’ (martensite with hexagonal structure), α” (martensite with orthorhombic structure) and ω-phase may also form in the Ti-Nb system from the β-phase field in fast cooling conditions [84-86]. In addition, it is possible to obtain β single phase at room temperature, if there is enough Nb. On this case, C_6 = 56 wt% of Nb is necessary in order to stabilize the β phase. Lower Nb content leads to formation of α and β stable at room temperature, in equilibrium conditions. Nb content lower than C_1 (13.1 wt%), β transforms to α’ martensite (hexagonal structure) in fast cooling condition. The martensitic start transformation temperature is labeled as $M_s^{\alpha'}$. From alloy content C_1 upwards, α” martensite is formed with orthorhombic structure. This martensitic transformation takes place up to an alloy content of C_4 (39.9 wt% Nb), from which the martensitic start transformation temperature $M_s^{\alpha''}$ becomes lower than the final quenching temperature, T_q. Nb content between C_3 (28.5 wt%) and C_6 (56 wt%) stays in a field where $M_f^{\alpha''}$ and $T_0^{\beta/\alpha}$ are equal to T_q, and β is metastable under fast cooling conditions.

There are two morphologies of ω-phase in Ti-Nb alloys: athermal (ω_{ath}) with trigonal structure and isothermal (ω_{iso}) with hexagonal structure [89]. The former, formed from β and indicated by temperature $T_0^{\beta/\omega}$, occurs on fast cooling conditions and is undesirable when shape memory effect is expected; the latter is formed on aging heat treatment and is related to embrittlement on Ti-Nb alloys [19, 88]. The $\beta \rightarrow \omega$ transformation is related to concentrations between C_2 (25.5 wt% Nb) and C_5 (52% wt% Nb), when $T_0^{\beta/\omega}$ is higher than $M_f^{\alpha''}$. This transformation competes with α” martensite formation on fast cooling and interfere on shape memory effect and pseudoelasticity mechanisms of Ti-Nb alloys [85].

The pseudoelastic effect observed in the β-Ti alloys results from the thermoelastic and reversible $\beta \rightarrow \alpha''$ martensitic transformation. A β single phase microstructure is necessary to obtain pseudoelasticity on such alloys. For the binary alloy Ti-40.5Nb (wt%), for instance, the critical martensitic transformation stress to transform β into α” was determined as 170 MPa. A recoverable strain of 2.5% was reported for this composition at room temperature [25, 27, 87], which when compared to the 5.0% of the Ni-Ti alloys [80], stands as an important drawback of the Ti-Nb-based alloys in applications where pseudoelasticity is required. The main reason for that is the low yield strength of the Ti-Nb alloys causing plastic deformation prior the strain-induced martensitic transformation. Therefore, some studies have been performed adding alloying elements and applying thermomechanical treatments, reducing the martensitic transformation temperature and increasing the resistance to plastic deformation of the Ti-Nb alloys [25, 27, 85, 88].

Zhang et al. (2013) investigated the additions of Ta, Fe, Zr, Mo, Sn and Si in ternary Ti-35Nb-1X (wt%) alloys, with effects on microstructure, mechanical properties and shape memory effect of the alloys. The as-cast button-shaped ingots were hot-formed by compression at 1073 K, with 50% of reduction in thickness, followed by solubilization heat-treatment at 1073 K for 0.5 h and water quenching. It is reported that the elements shown small effects in the microstructure of the samples, and β- e α”-phase were identified after the solubilization heat treatment. Sn, Si, Fe e Ta were responsible for the highest solid solution strengthening in the Ti-35Nb-1X (wt%) alloys. The addition of Zr resulted in a slight decrease in the elastic modulus, while Ta caused no considerable change. According to the reported results, Ta, Fe, Zr, Mo, Sn, and Si resulted in higher pseudoelasticity in the ternary alloys [88].

Hence, the Ti-35Nb-7Zr-5Ta (wt%) alloy emerges as promising for biomedical application in prostheses. The alloy composition contains exclusively non-toxic elements, with a combination of mechanical strength, hardness and low Young’s modulus [29, 31, 89]. Tahara et al. (2010) investigated the effect of nitrogen addition and heat-treatment in samples of Ti-(14-24)Nb-4Zr-2Ta-(0-0.6)N (at%), which corresponds to a Ti-35Nb-5Zr-5Ta (wt%) alloy, submitted to annealing at various temperatures for 1 h [31]. The stress-strain curves obtained at room temperature shown that alloys with 27-30 wt% of Nb and free of N presented shape memory effect, after being heated to 500 K.

Pseudoelasticity was observed in alloys with 32 wt% of Nb, with a recoverable elastic strain (pseudoelasticity) of 2.0% (Figure 2.20) [31].

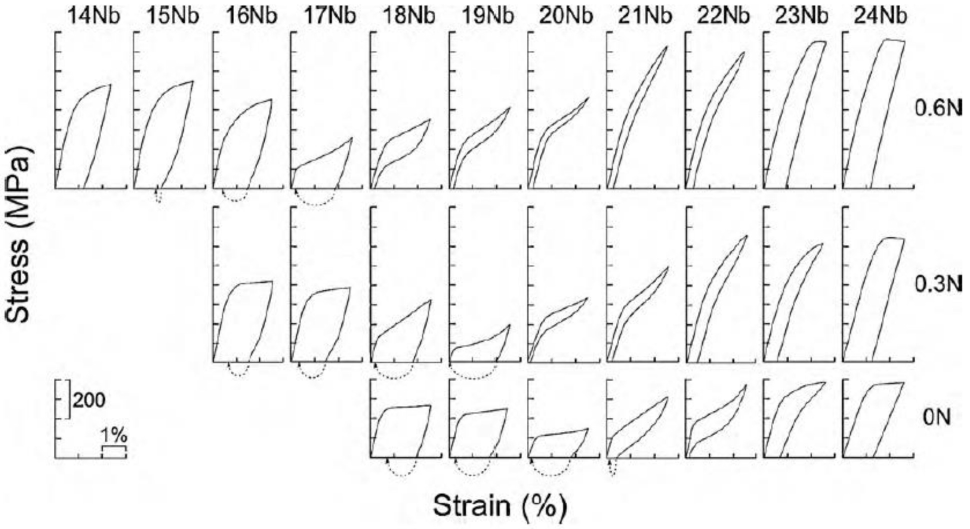

Figure 2.20. Stress-strain curves obtained at room temperature of Ti–Nb–Zr–Ta alloys. The composition is given in at%. [31].

The effect of annealing temperature was also investigated in the alloy Ti-32Nb-5Zr-5Ta (wt%) and the micrographs are shown in Figure 2.21. The results shown that the samples presented α and β phases when annealed at 773 and 873 K. The bright field TEM images of the samples annealed at 773-1073 K shown grain growth as the annealing temperature was increased. A fine subgrain structure was observed in the sample annealed at 773 K (Figure 2.21a). In samples annealed at 873 K (Figure 2.21b), α precipitates at β grain boundaries, while only a β single-phase microstructure is observed in samples annealed at 973 and 1073 K (Figure 2.21c and d), confirmed with X-ray diffraction patterns. The results also shown that the grains presented more significant grain growth in the samples heat-treated at 973 and 1073 K, where the precipitation of α was absent.

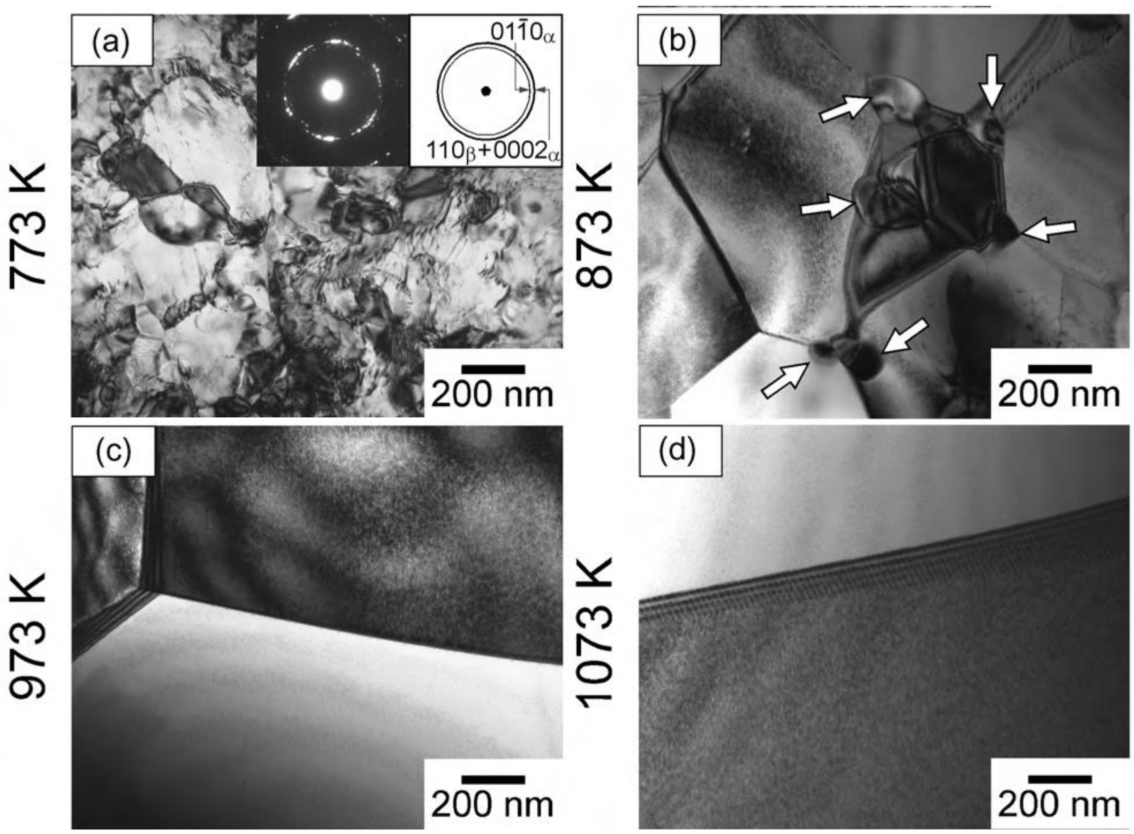

Figure 2.21 – Micrographs of a Ti–32Nb–5Zr–5Ta (wt%) alloy analyzed by transmission electron microscopy (TEM). The samples were annealed for 1 h at the following temperatures: a) 773 K, b) 873 K, c) 973 K, and d) 1073 K. The α phase precipitation is indicated by arrows [31].

Ferrandini et al. (2007). investigated phase formation on samples of a Ti-35Nb-7Zr-5Ta (wt%) alloy submitted to thermomechanical treatment, followed by solubilization treatment at 1000 °C for 35 min and water cooling, and aged at 200, 300 and 400 °C (for 4 h). The authors report that either the solubilized or the aged samples presented only β peaks in the XRD experiments (Figure 2.22). The authors state that Ta and Zr displaces the β → α transformation to increased times, avoiding α precipitation in the samples, even though Zr is a neutral element [14,15]. In addition, ω-phase formation was not observed, and it is related to the Zr effect of suppressing the β → ω transformation in the alloy [29].

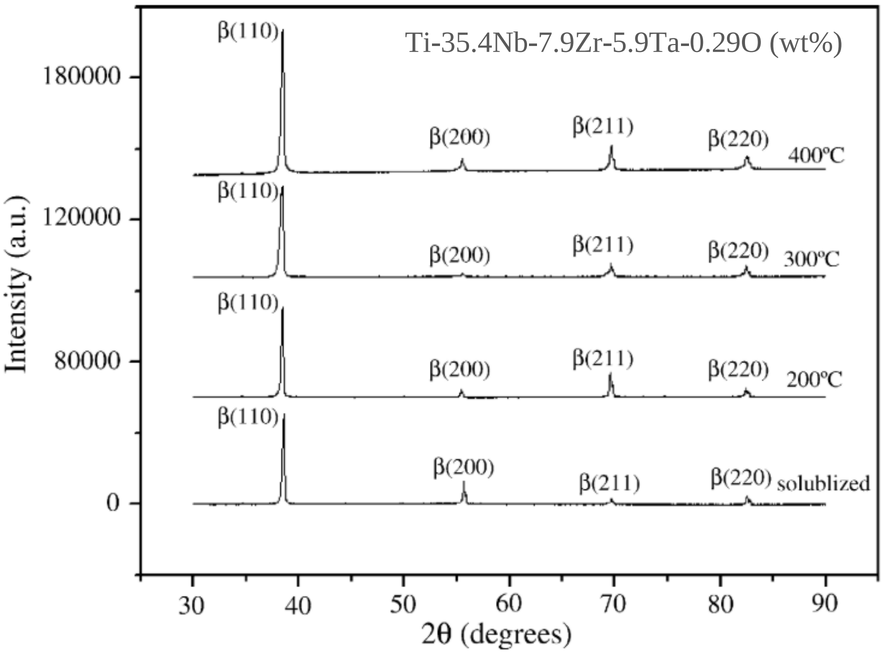

Figure 2.22. XRD patterns show that only β phase was detected for samples solubilized and aged at temperatures up to 400 °C [29].

2.5 Oligocrystalline Structure and Pseudoelasticity

One of the drawbacks of Ti-Nb-based alloys is the low recoverable strain when compared to the Ni-Ti system, which limits the applicability of Ti-Nb alloys in biomedical parts when pseudolelasticy is required. Recent studies have reported an alternative method to improve pseudoelasticity of Cu-based shape-memory alloys, when an oligocrystalline or bamboo structure is formed (oligo – few; crystalline – crystals). This results in recoverable strain and pseudoelasticity comparable to those observed in single crystals of Cu-based alloys, overcoming the premature failure normally seen in Cu-based shape memory alloys due to brittle fracture along grain boundaries [32, 33].

The oligocrystalline shape memory alloys (oSMA) are defined as alloys in which the total grain boundary area is less than the total sample surface. The higher surface area in an oligocrystalline structure allows the martensitic phase transformation, the basic shape memory effect mechanism, to occur with less inhibition than in a conventional polycrystalline structure [33]. The grain boundaries in polycrystalline alloys are preferential sites for nucleation of martensite with certain configurations but imposes limitations to the extension of the transformation [90]. The oligrocrystalline or bamboo structure enables the control of the martensite variants nucleation and increase the extent of the transformation [33].

It has been reported a pseudoelasticity of 8% in a Cu-11.9Al-4.4Mn-3.9Ni (wt%) alloy, with oligocrystalline structure formation associated to a crystallographic texture [91]. The samples had a wire geometry with 45–300 µm diameter obtained by the Taylor wire casting technique. In another work, microwires of Cu-Al-Ni with oligocrystalline structure were obtained (Figure 2.23a-e) [92]. The filaments presented a uniform diameter and the *bamboo* structure was formed: some few grains with grain boundaries at approximately 90° of the filaments' main axis. Martensite laths are observed, which meant that the martensitic transformation temperature, M_S of the alloy was higher than the room temperature.

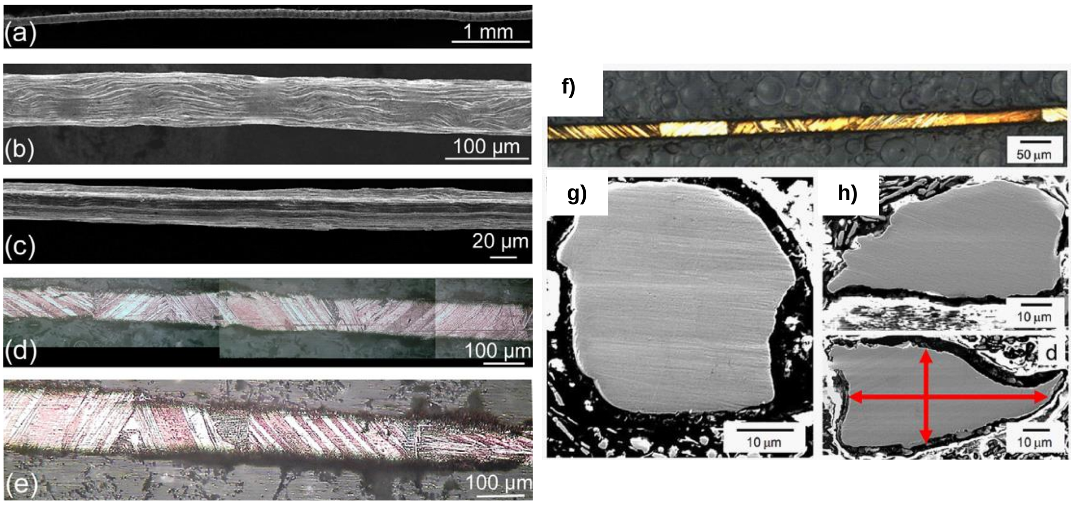

Figure 2.23. Wires of a Cu-Al-Ni alloy with average diameter of 90 (a), 65 (b) and 30 µm (c); optical micrographs of a cross section of a wire with diameter of 100 µm, showing the bamboo structure with martensitic laths spanning through the whole sample cross-section (d-e) [92]; optical micrographs of a Cu–Zn–Al ally with oligocrystalline structure (f-h) [90].

Furthermore, another work investigated the effects of sample size on the pseudoelasticity of microwires, with diameter varying between 100 µm a 20 µm obtained by wire-casting [90]. The filaments of Cu-22.9Zn-6.3Al (wt%) alloy were produced by the Taylor wire casting technique and presented oligocrystalline structure (Figure 2.23f-h). The martensite laths seen in the microstructure (Figure 2.23f) indicate that the M_s of the alloy was above room temperature. It may also be noticed that martensite laths extend through the whole sample geometry.

The grain size/sample size relationship effect was investigated on the pseudoelastic behavior of a Cu-17Al-10.5Mn-0.5Co (wt%) shape memory alloy, in sheets submitted to thermomechanical treatment [93]. Recoverable strain of 7% was observed in the samples with oligocrystalline structure: The grains extended through the whole sample thickness (Figure 3.24a). The inverse-pole figures (Figure 2.24b) and pole figures (Figure 3.24d), obtained by electron back-scattered diffraction, shown the grain orientation related to the applied tensile stress and the orientation-dependency of pseudoelasticity on each grain, respectively. It was noticed that the highest recoverable strain of ≈ 9% occurred in grains labeled as (2) and (3), which were oriented approximately parallel to the tensile stress applied.

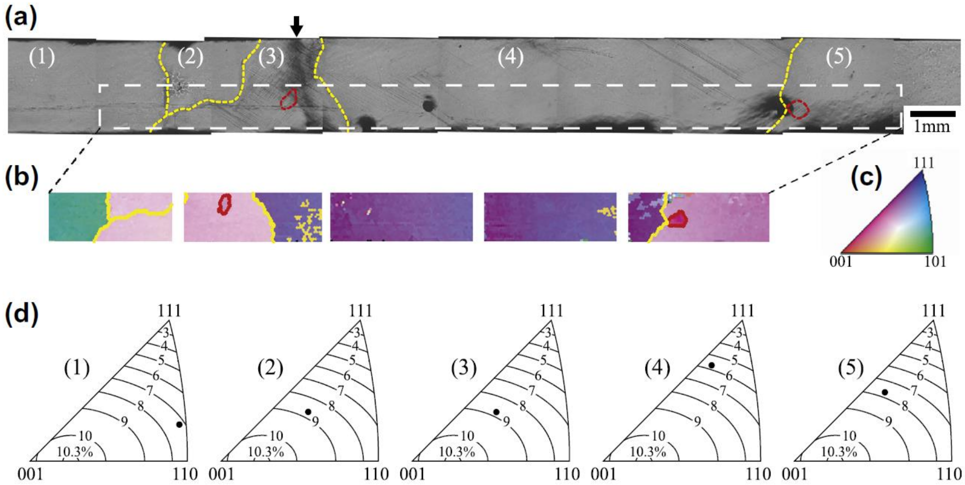

Figure 2.24. (a) Oligocrystalline structure in a sample of 72.0Cu-17Al-10.5Mn-0.5Co (wt%), after being submitted to cyclic tensile test; (b) EBSD maps showing the corresponding grain orientations in the region limited by the dash lines; (c) stereographic triangle for reference; (d) pole figures showing orientation of grains labeled 1-5, related to the tensile stress direction [93].

Besides the Cu-based shape memory alloys, some other works have reported oligocrystalline structure formation in Fe-based [94] and Ni-based [95, 96] alloys; pure Al [97] and pure Ta [98]. More recently, a cyclic-heat treatment was developed to induce abnormal grain growth and obtain oligocrystalline structure in bulk samples of a Cu-Al-Mn alloy [99, 100]. Nonetheless, to the author’s best knowledge, there are not reported results of oligocrystalline structure formation in Ti-Nb-based alloys. In addition, the processing route used to obtain the *bamboo* structure is either the Taylor wire casting technique or thermomechanical processing. On this work, an innovative approach is proposed to obtain a bamboo-like structure formation in a β-Ti-35Nb-7Zr-5Ta (wt%) alloy with selective laser melting, an additive manufacturing technology.

3. EXPERIMENTAL PROCEDURE

This chapter describes the experimental techniques for samples preparation and characterization. Figure 3.1 illustrates the workflow with the general approach and experimental methods applied.

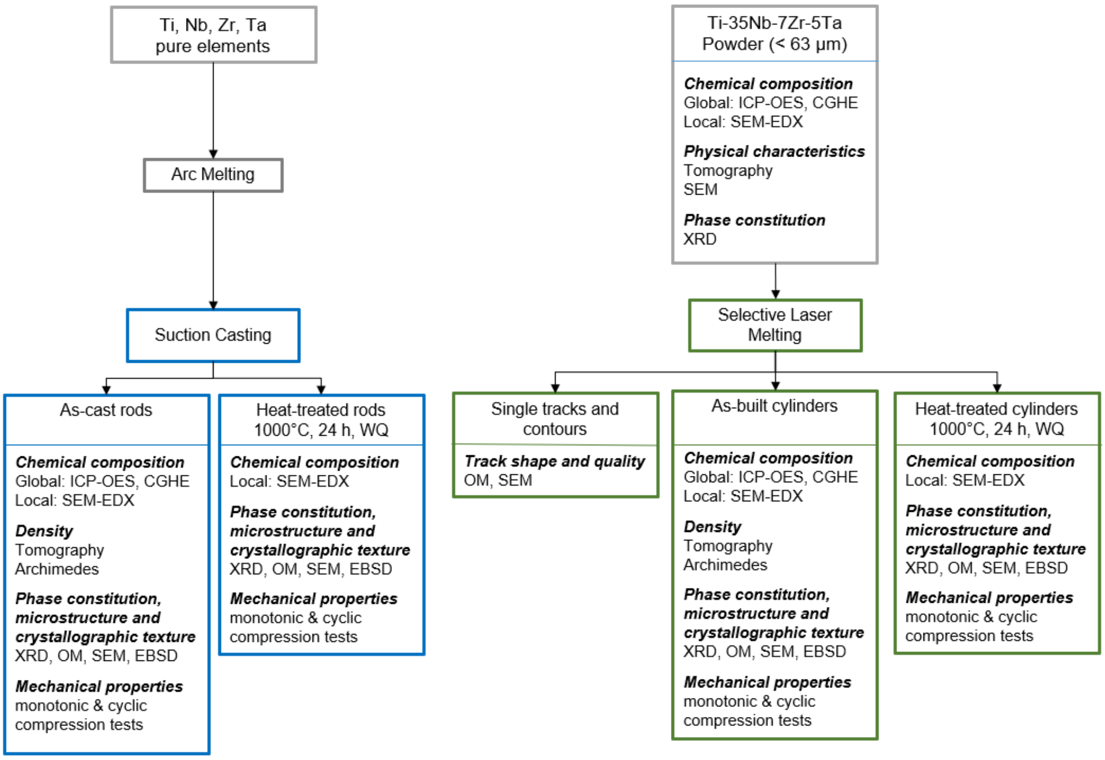

Figure 3.1 Overview of workflow and experimental methods.

3.1 Materials

3.1.1 Ingots preparation and Cu-mould suction casting of rods

The processability of the Ti-35Nb-7Zr-5Ta (wt%) alloy was first studied by producing samples in a more conventional technique. Therefore, rods with 3 mm of diameter and 30 mm of length were produced by Cu-mould suction casting in a Mini-Arc Melter Edmund Bühler GmbH. Ti, Nb, Zr and Ta pure elements (99.99% purity) were arc-melted to produce the pre-alloy in button-shaped ingots with ≈ 15 g. The pre-alloy was remelted five times in order to assure chemical homogeneity of the elements. Then, 1.5 g of the ingots were cut and used to cast the rods, as follows: In the beginning, the valves were opened with tubes connecting the melting and suction chambers. These chambers were then evacuated to 10^{-4} mbar. Then, the valves were closed, and the melting chamber filled with argon in order to obtain a protective atmosphere, enable the formation of the electric arc and create the difference in pressure, which is responsible for the suction energy. A Ti-getter was first melted in order to remove residual oxygen in the melting chamber [101].

Due to high viscosity of the molten TNZT alloy, the ingot had to be slightly dislocated from the mould orifice in the melt chamber before switching on the electric arc. Then, the current used to melt the alloy was quickly increased (level 7 to 9) and the suction valve was opened immediately after the liquid started flowing with the electric arc still opened, in order to facilitate the suction of the melt into the water-cooled Cu-mould. The as-cast samples were labeled *TNZT-as-cast*.

3.1.2 Powder feedstock and chemical analysis

The gas-atomized Ti-35Nb-7Zr-5Ta (wt%) powder was supplied by Ercata GmbH as spherical powder with particle size < 150 µm and 99.99% of purity, in an Ar-sealed container with 5 kg of powder. The powder was dry-sieved and a fraction of 3 kg with particles size < 63 µm was used in selective laser melting (SLM), labeled as *TNZT-powder*.

The chemical analysis of the main elements Ti, Nb, Zr and Ta of the powder and bulk samples were performed by inductively coupled plasma optical emission spectroscopy (ICP-OES; Thermo Fischer Scientific). The carrier gas heat extraction technique (CGHE; LECO) was applied to analyze the oxygen content. At least three analysis for each element were performed. The local element distribution in the powder and bulk samples was analyzed by energy dispersive X-ray spectroscopy (EDX) coupled with scanning electron microscopy (SEM). The mass unity used throughout the present work to describe chemical composition of the samples is mass weight percentage (wt%).

3.1.3 Selective laser melting – parameters optimization

Samples were manufactured by selective laser melting in a Realizer SLM 50, with a fiber laser in continuous mode (λ = 1070 nm, focus position F: 9.55 mm, spot size ≈ 60 μm) and laser power of 129 W (Figure 3.2). The construction volume is 70 mm diameter and 40 mm height. The samples were produced on baseplates of pure Ti (grade 2) at room temperature (peak temperature of 40 °C), previously sandblasted in order to obtain a reproducible surface. The layer thickness was kept at 40 μm in all experiments. The atmosphere was filled with argon (99.99% purity) under constant flow of 8000 l/min, with a chamber pressure of ≈ 20 mbar. The oxygen content in the build chamber was kept < 0.1 wt%.

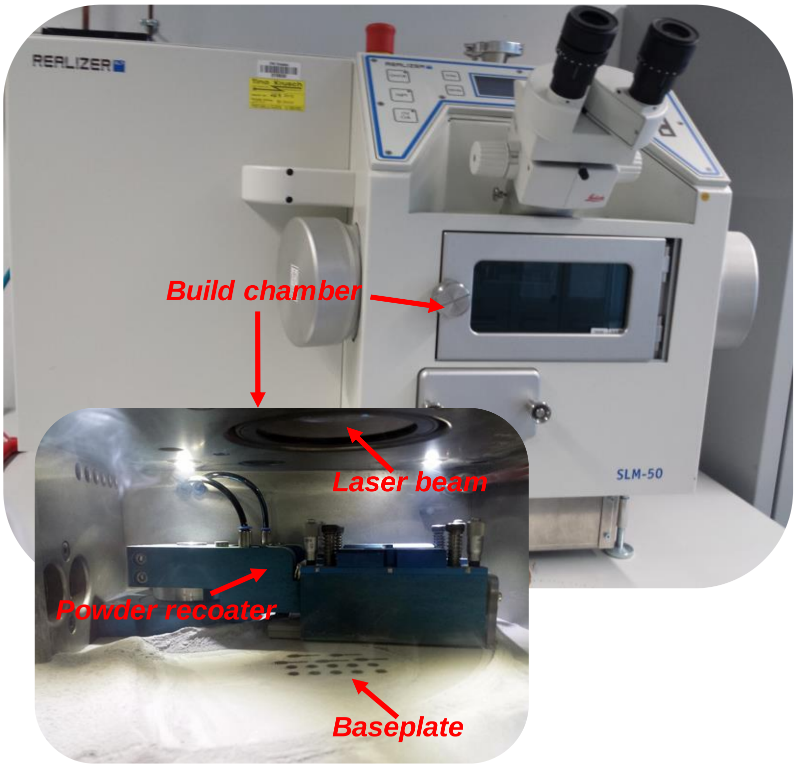

Figure 3.2. Selective laser melting Realizer SLM 50 device used throughout the experiments.

A first set of experiments was performed to optimize the laser parameters. For this experiment, laser power of 61 and 129 W was applied on a thin layer of powder with ≈ 100 μm thickness and single tracks with 20 mm length were produced. Scanning speed of 0.30, 0.33, 0.50, 0.57, 0.75, 1.00, 1.50, 2.00, 2.67, 3.00, and 4.00 m/s were applied for each laser power.

On a next step, cylinders with 3 mm external diameter and 6 mm in height were produced. This time, the outer shell of the cylinders (also known as contours) were melted, without defining a hatching distance or distance between tracks. The laser power was kept at 129 W varying the scanning speed in the range 0.33-4.00 m/s.

The linear energy input, E_l [J/m], on single tracks and outer-shell cylinders was calculated with the equation adapted to calculate the line energy input [102]:

$$E_l = \frac{P_l}{v_s},$$

where P_l is the laser power (W) and v_s is the scanning speed.

The track widths, wall thickness and morphology of the single tracks and contours were assessed by optical microscope. On this manner, the stability (stable, unstable, and balling) and uniformity of the melt paths could be assessed. Henceforth, three scanning speeds were selected to build bulk cylinders with 3 mm diameter and 10 mm height. Therefore, bulk samples were produced with scanning speed of 0.33, 0.57 and 2.67 m/s, and overlapping of 25, 50 and 75% on each scanning speed, while keeping the laser power of 129 W, layer thickness of 40 µm and unidirectional scanning strategy with 79° scanning vector rotation between successive layers (cross-hatching). Next, the hatching distance (distance between tracks) was further optimized keeping the scanning speed at 0.57 m/s, covering an overlapping range of 10-75%. The volumetric energy input, E_v [J/mm³], was calculated by the following equation [102]:

$$E_v = \frac{P_l}{v_s \, . \, h_s \, . \, l_z} * 10^{-9},$$

where P_l is the laser power (W), v_s is the scanning speed (m/s), h_s is the hatching distance (10 µm) and l_z is the layer thickness (10 µm).

3.1.4 Sample orientation and laser remelting

In order to further investigate the possibility of modifying the microstructure of the TNZT alloy (e.g. phase formation, grain size, morphology and orientation) during the selective laser melting process, some additional experiments were performed. The formation of crystallographic texture was assessed by building cylinders by selective laser melting with different orientation. This time, samples at 0°, labeled as *TNZT-0°horizontal*, and 45°, labeled as *TNZT-45°degree* were produced with Ø 3 mm and 15 mm length (projected on the surface of the baseplate).

The parameters used were laser power 129 W, scanning speed 0.57 m/s, layer thickness 40 µm and 50% of overlapping. The scanning strategy was unidirectional and rotating 79° between each layer (cross-hatching). On the case of *TNZT-0°horizontal* samples, the scanning strategy had to be divided into stripes of 3.0 x 3.0 mm² (width x height), with a 50% of overlap between each island, in order to avoid the laser scanning a long line and, therefore, warpage during the process. On each stripe, the laser scanning was unidirectional and rotating 79° between each layer. Then, an experiment was performed adding a remelting step (*TNZT-remelting*) [103]. The parameters used in laser remelting were identical to the SLM parameters: laser power 129 W, scanning speed 0.57 m/s, layer thickness 40 µm and 50% of overlapping.

3.1.5 Selective laser melting of prototypes and thin-walled samples

Some prototypes were produced in order to attest the feasibility of producing parts of Ti-35Nb-7Zr-5Ta alloy with complex geometry by selective laser melting. Therefore, dental mini implants (*TNZT-mini-implant*) with threads and stents (*TNZT-stent*) were produced directly on the baseplate with the following parameters set layer thickness of 40 µm, laser power of 129 W and scanning speed of 0.57 m/s.

For the mini implants, an overlapping of 50% was applied and the prototype was built as a bulk sample with unidirectional scanning strategy 79° rotation between layers. In the case of the stents, hatching distance was not defined due to its open geometry and struts dimension corresponding to a single track. A remelting step was applied in order to improve the surface finishing of the stents with same parameters used in the first melting.

Thin-walled samples (hollow tubes with 3 mm of external diameter, wall thickness of 200 µm and 12 mm height) were also produced by selective laser melting to investigate oligocrystalline structure formation. The parameters used were laser power of 129 W, scanning speed of 0.57 m/s, with a layer thickness of 40 µm. Hatching distance was not defined and the wall thickness corresponded to a single track. The thin-walled tubes were labeled *TNZT-single-tube*.

3.1.6 Heat treatment

In order to homogenize the as-cast rods and as-built selective laser melted samples, a homogenization heat treatment was applied. The samples were encapsulated in fused-silica glass, evacuated and filled with 500 mbar of argon and heat-treated at 1000 °C (β single phase stability field) for 24 hours in Ar atmosphere, followed by water quenching [88]. The thin-walled tubes produced by SLM were also heat-treated in the same conditions in order to investigate grain growth mechanism and the formation of the bamboo (oligocrystalline) structure (*TNZT-tube-HT*).

3.2 X-ray Computed Micro-tomography and Density Measurements

In order to investigate the powder characteristics and determine particle size distribution, sphericity, anisotropy and overall porosity, X-ray computed micro-tomography (µ-XCT) was performed. It is a non-destructive method, which allows evaluation of internal characteristics and 3-D imaging of materials [104]. The measurements were carried out in a GE Phoenix Nanotom® M device, with following parameters: 130 kV, 110 µA, tungsten target and 0.3 mm Cu filter; voxel size of 1.5 µm; exposure time of 1000 µs per image and 1000 images for 360° sample rotation. Two samples of powder were taken from particle size fraction < 63 µm (used for SLM) and approximately six-thousand particles were analyzed. In order to reconstruct the scan, the software VGStudio Max 2.2.7 of image analyzing was used. After reconstructing, the evaluation of the powder particle size and morphology was done using the software Avizo 9.4.0.

The µ-XCT was specially used to determine the optimal selective laser melting parameters of the TNZT alloy, which produced samples with highest density. The degree of porosity and internal soundness of the as-cast rods and as-built selective laser melted cylinders were assessed by µ-XCT with same parameters used for the powder; only this time a different voxel size was used. The voxel size is defined by the device resolution limit and dependent on the sample size as ≈ 0.5 µm x largest sample dimension [105, 106]. On this way a voxel size of 4.0 µm was used for bulk samples.

The densities of the bulk samples (as-cast and SLM) were also determined by the Archimedean method using a balance (Sartorius MSA2255) with Cubis density kit. Part density was measured as follows: The samples were weighed in air, then immersed into distilled water for a few seconds and weighted again. Relative density was calculated by considering the density of a suction-cast sample, which present lowest observed porosity with µ-XCT (< 0.01% of porosity). Samples with relative density higher than 99.0% were considered of good quality and the related parameters set taken as the optimized selective laser melting parameters.

3.3 Microstructure and Phase Formation Characterization

3.3.1 X-ray diffraction

The phase constitution of the Ti-35Nb-7Zr-5Ta (wt%) powder, as-cast rods, as-built SLM cylinders and heat-treated samples was analyzed by X-ray diffraction. The measurement was carried out in a Stoe Stadi P device on transmission mode, equipped with a position-sensitive detector and Ge (111) monochromator, which selects Mo-Kα1 radiation (λ = 0.07093 nm) and a generator operating with 50 kV and 40 µA. The loosen powder sample was carefully glued in an acetate piece and then placed in the sample holder. In the case of bulks, samples were cut from the middle of the bulks (x-y cross section) and then manually ground to thicknesses around 100 µm using 400 and 800 mesh grinding papers, and at least two samples were measured for each case. The samples were rotated around their normal axis during the measurement in order to enhance scattering statistics. The parameters used were diffraction angle scan range of 5-60°, step size of 0.5 °/min and time step of 80 s. Two ranges for each sample were measured. The data were analyzed with the software PANalytical X'Pert HighScore Plus 4.7 using the PDF-4+ 2016 database of the International Centre for Diffraction Data (ICDD).

3.3.2 Metallography

The microstructure of the powder, as-cast rods, as-built (SLM) cylinders and heat-treated samples was investigated by microscopy. The samples were metallographically prepared following the steps: cold mounting in an epoxy resin + catalyst + carbon powder mixture, grinding in SiC paper up to 4000 mesh and polishing for 10 min in a Struers Tegrapol with 300 rpm, 10 N and oxi-silicate + 10 vol% H_2O_2 polishing solution (0.04 µm). Polished and etched surfaces were analyzed: the etchant solution was 5 HF (40% concentrated) + 10 HNO_3 (65% concentrated) + 85% H_2O, with a dwell time of 15 s, followed by ultrasonic-bath cleaning for 5 min and drying in a hand-drier [84]. The SLM samples were examined in x-y (laser scanning plane) and y-z (building plane) cross-sections.

3.3.3 Optical microscopy

The overall quality of the single tracks and contours was assessed and the track widths, wall thickness and morphology of the single tracks and contours were evaluated by optical microscope. The microstructure of the as-built SLM cylinders, as-cast rods and heat-treated samples were also investigated. A digital optical microscope Keyence VHX 6000, with magnification from 30 to 2000x was used. The planar average grain size of the bulk samples was measured by the intercept procedure in at least three micrographs taken along the building direction of the samples (ASTM E112-13). The number of grains intercepted by three test circles was counted and the average grain diameter ($\overline{d_G}$) was calculated in the native image processing software in the Keyence VHX 6000 microscope. The grain size was also determined by the comparison procedure following the ASTM E112-13 Standard and the ASTM grain size number, *G*, was obtained.

3.3.4 Scanning electron microscopy

The morphology of the powder and microstructure of the as-built SLM cylinders, as-cast rods and heat-treated samples were investigated in a scanning electron microscope (SEM Field Emission Gun, Gemini Leo 1530 from Carl Zeiss AG), with secondary electrons (SE) and back-scattered electrons (BSE) detectors. A Bruker Xflash 4010 energy-dispersive X-ray (EDX) system was used to perform chemical microanalysis of the samples.

The crystallographic texture, grain size and morphology of the as-built SLM cylinders, as-cast rods and heat-treated samples were analyzed by means of electron back-scattered diffraction (EBSD), with a Bruker e-FlashHR 1000 detector attached to the SEM Gemini Leo. The electron back-scattered pattern (EBSP) datasets were post-processed using the software Bruker ESPRIT 2.2.1. A misorientation criterion of 10° was employed to differentiate between low- and high-angle boundaries. Inverse pole figure (IPF) maps combined with the microstructure were obtained (the sample axis relative to the crystal orientations, i.e., which crystallographic directions align with the specimen axes).

Further analyzes of the EBSP datasets (pole figure and grain size) were performed in the Chanel 5 software package (HKL Technology, Denmark). The pole figures (stereographic projection of a crystal axis down some sample direction) were calculated in Chanel 5 Mambo software, setting the z-axis of the samples in the building direction. The crystallographic average grain size was also determined with the intercept procedure: parallel test lines are drawn over the EBSD map and the points where the lines intercept a grain boundary are counted (ASTM E112-13). The mean transversal linear intercept length, ($\overline{l_t}$), and mean longitudinal linear intercept length, ($\overline{l_l}$), was obtained in the transverse (y) and longitudinal (z) axes, respectively, of the samples building plane cross-section with the Channel 5 Tango software.

3.3.5 Transmission electron microscopy

The microstructure and phase analysis of the TNZT as-cast rods and as-built SLM cylinders was analyzed in a high-resolution transmission electron microscope (TEM Fei Tecnai G2 F20), in bright field and dark field modes. The samples were cut from the middle of the bulks (x-y cross section) and then manually ground to thicknesses around 100 µm using 400, 800 and 1200 mesh grinding papers. Then, ionic polishing was employed using a precision ion polishing system (Gatan 691). The electron diffraction patterns obtained by TEM were evaluated in the software ELDISCA C1.2 [101].

3.4 Mechanical Characterization

Compression test in monotonic and cyclic modes were conducted on Ø 3 mm cylindrical specimens cut from the as-cast rods, as-built SLM cylinders and heat-treated samples to an aspect ratio ≈ 2 (height/diameter), following the ASTM E9-19 Standard. The samples were carefully ground to 1200 mesh in order to obtain parallel surfaces, perpendicular to the cylinder axis. The tests were conducted in an Instron 5869 device and the strain was measured with a laser-extensometer (Fiedler Optoelektronik GmbH).

The monotonic uniaxial compression test was conducted by increasing the compressive load. The experiment was stopped after 60% of strain due to strain measurement issues, without breaking the specimens. The experiments were performed at a constant strain rate of 10^{-4} s^{-1} and at least three specimens were tested for each condition. The yield point was determined by means of the offset method: a straight line intersecting the strain axis at a predefined value (0.2% strain offset) was drawn parallel to the elastic segment. The test was conducted with a laser extensometer and, therefore, the Young's modulus of the specimens was recorded.

The cyclic uniaxial compression test was carried out by loading-unloading the specimens up to 6.5% of strain on steps of 0.5%. Figure 3.3 shows a stress-strain curve obtained in cyclic compression test.

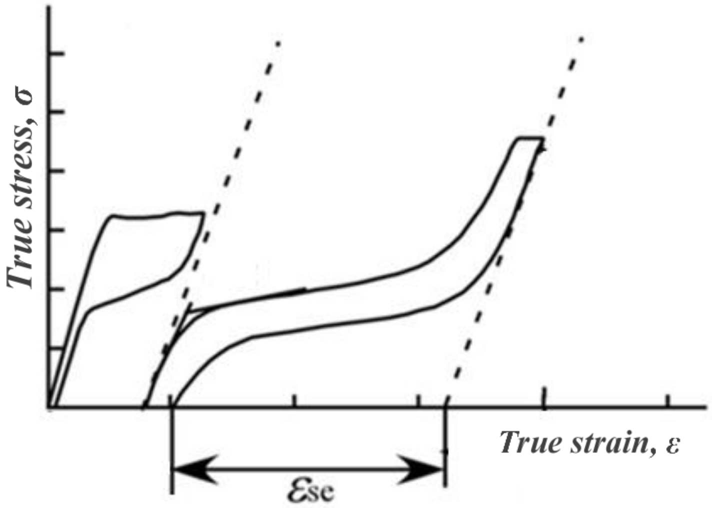

Figure 3.3. Illustration of a stress-strain curve in a cyclic compression test, indicating the recoverable strain, ε_{se}, as a measure of pseudoelasticity [85].

Every loading-unloading sequence produced a hysteresis loop and the last unloading step was conducted from an applied strain of 6.5%. The pseudoelasticity of the samples was measured by the recoverable strain, ε_{se}, (Figure 4.3) [85]. The loading and unloading steps were performed at strain rate of 10^{-4} s^{-1}.

4. RESULTS AND DISCUSSION

4.1 Rapid Solidification by Cu-mould Suction Casting

The processability of the Ti-35Nb-7Zr-5Ta (wt%) alloy was first studied by producing samples in a more conventional technique. Therefore, rods with 3 mm of diameter and 30 mm of length were produced by Cu-mould suction casting (Figure 4.1).

Figure 4.1. *TNZT-as-cast* rods.

The bulk chemical analysis of Ti, Nb, Zr and Ta in the as-cast samples was performed by ICP-OES (Table 4.1). The composition of the samples is approximately equal to the nominal composition of the alloy, although a high standard deviation is noticed in the Ta content. The oxygen content was analyzed using the carrier gas heat extraction technique (CGHE), with a concentration of (900 ± 30) ppm, within the specified for the alloy (7500 ppm) [28].

Table 4.1. Chemical analysis of the *TNZT-as-cast* samples.

Sample	**Ti (wt%)**	**Nb (wt%)**	**Zr (wt%)**	**Ta (wt%)**	**O (ppm)**
TNZT [28]	55.2-47.1	34.0-37.0	6.3-8.3	4.5-6.5	7500 (max)
TNZT-as-cast	53.4 ± 0.5	34.7 ± 0.5	7.1 ± 0.3	4.6 ± 3.4	900 ± 30

4.1.1 Phase formation and microstructure

The phase formation was analyzed by X-ray diffraction and the resulting pattern show a β single phase structure (Figure 4.2), which is related to the high β stabilizing content in the alloy.

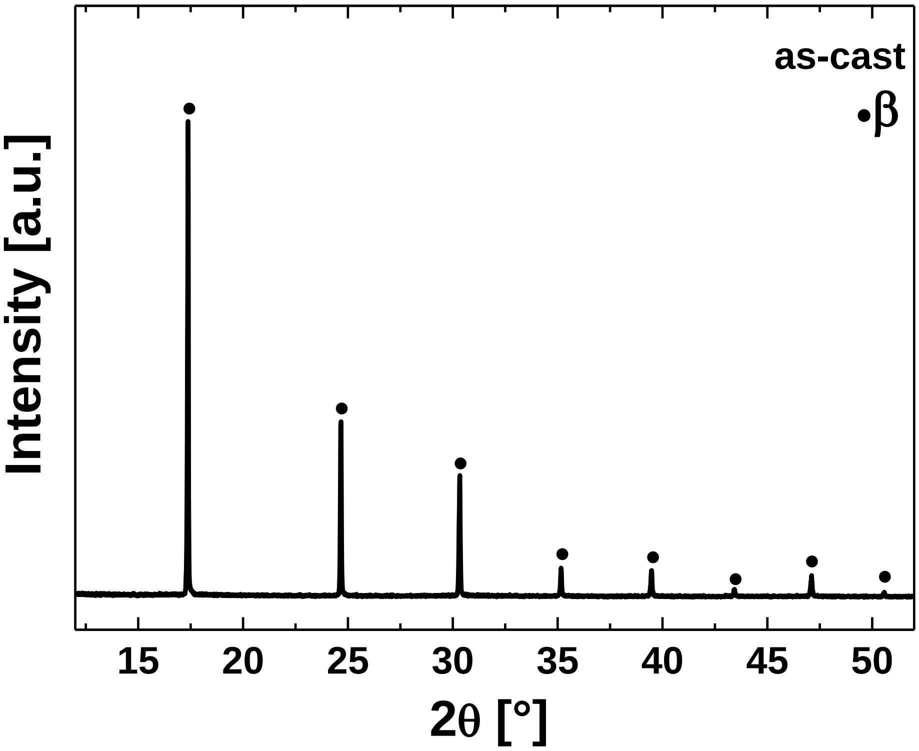

Figure 4.2. Diffractogram of sample produced by Cu-mould suction casting (*TNZT-as-cast*).

An equiaxed dendritic structure is observed in the as-cast samples (Figure 4.3a-c), a result of the high alloying content and solidification rate (constitutional supercooling), combined to thermal diffusivity properties of the alloy and thermal gradient imposed by the Cu-mould suction casting process. The presence of precipitates is not observed, differently from the results in arc-melted button-shaped samples of same nominal composition [26].

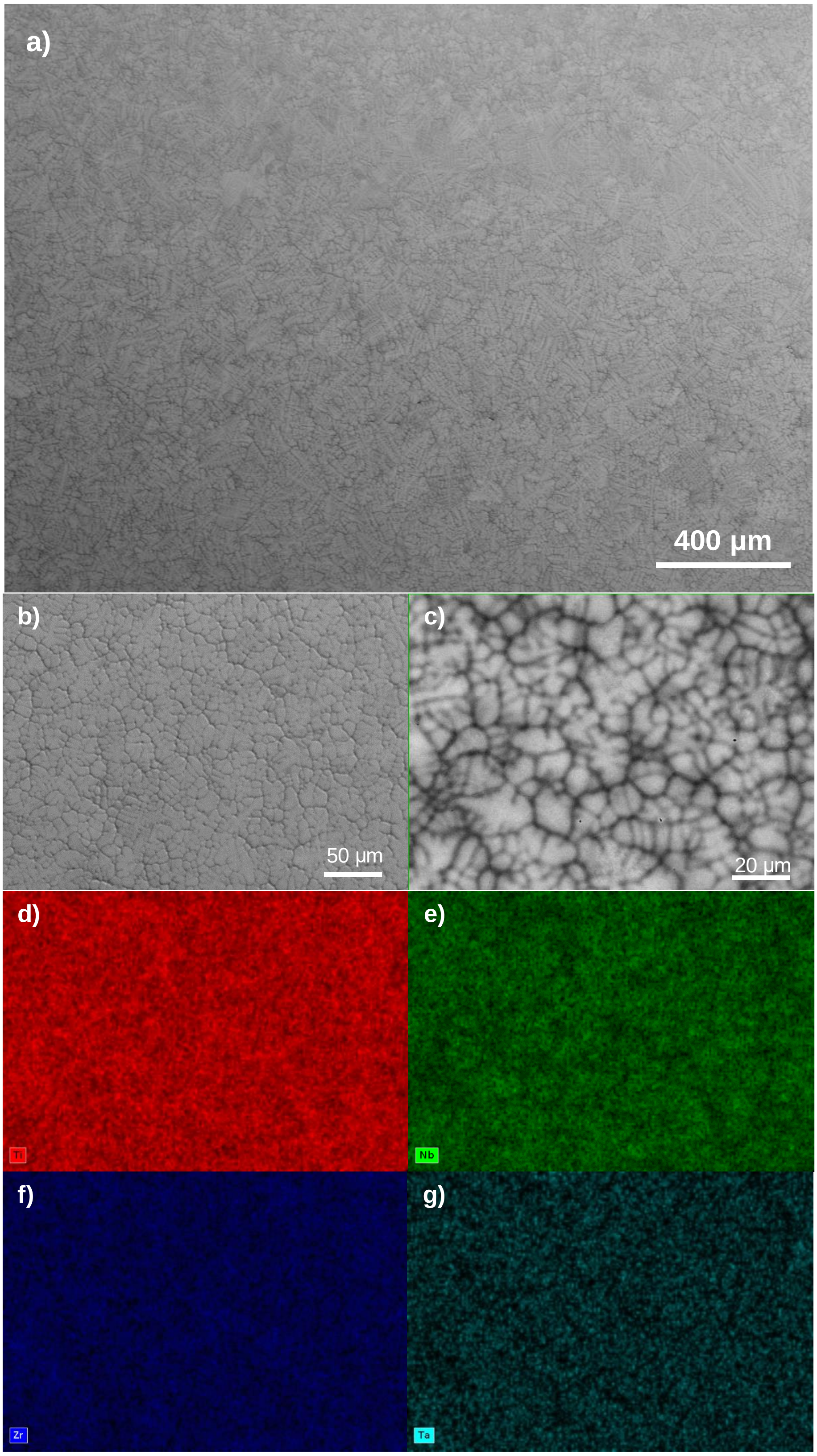

Figure 4.3. (a) Microstructure of the *TNZT-as-cast* sample; (b) equiaxial dendritic structure of the as-cast sample; (c) chemical contrast observed by back-scattered electrons (BSE) and (d-g) EDX maps.

The semiquantitative chemical analysis obtained by energy-dispersive X-ray spectroscopy (EDX) microanalysis of the as-cast samples resulted in a composition of Ti-34.5Nb-7.1Zr-4.8Ta (wt%), practically identical to the composition obtained in the inductively coupled plasma optical emission spectroscopy analysis (Ti-34.7Nb-7.1Zr-4.6Ta-0.09O). The EDX maps also show microsegregation in the grain boundaries, with formation of Nb- and Ta-enriched dendrites and a Ti-rich interdendritic phase (Figure 4.3b-f). This result was previously reported in Ti-Nb binary alloys and it is related to the solidification process and it has been proposed that the cooling rate during suction-casting is not high enough to avoid Ti diffusion from the core of the dendrites, resulting in microsegregation in the solidification process [84, 107].

Bright field TEM images of the as-cast sample (Figure 4.4a), with selected area electron diffraction (SAED) pattern of the α“ martensite laths (Figure 4.4b) (zone axis: [100]).

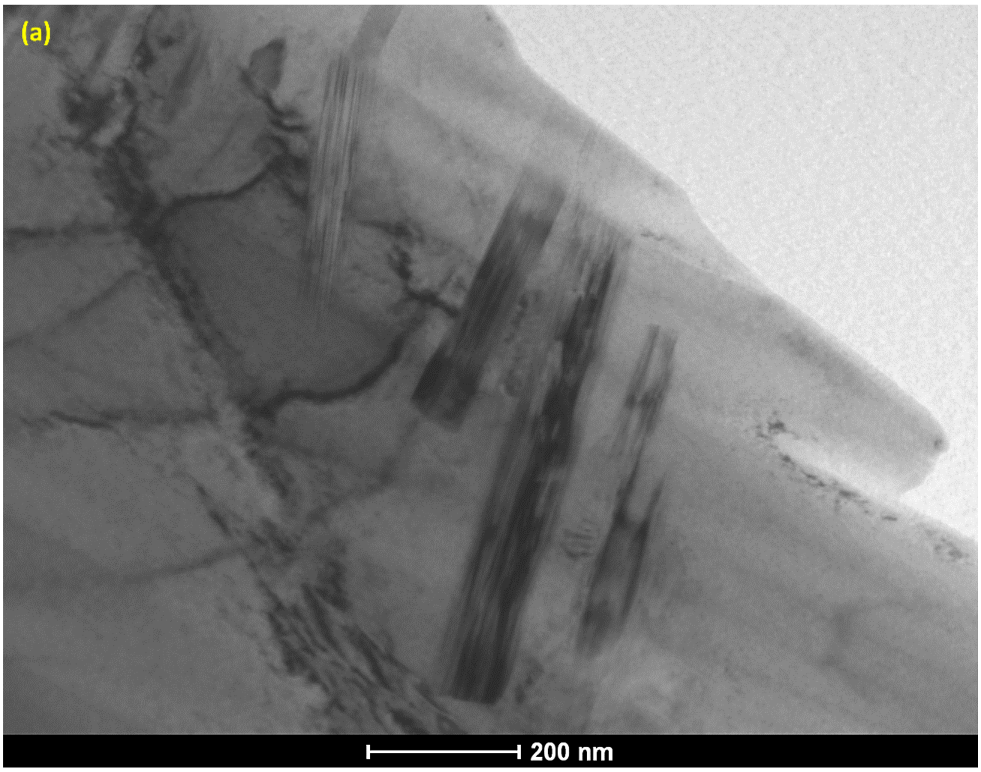

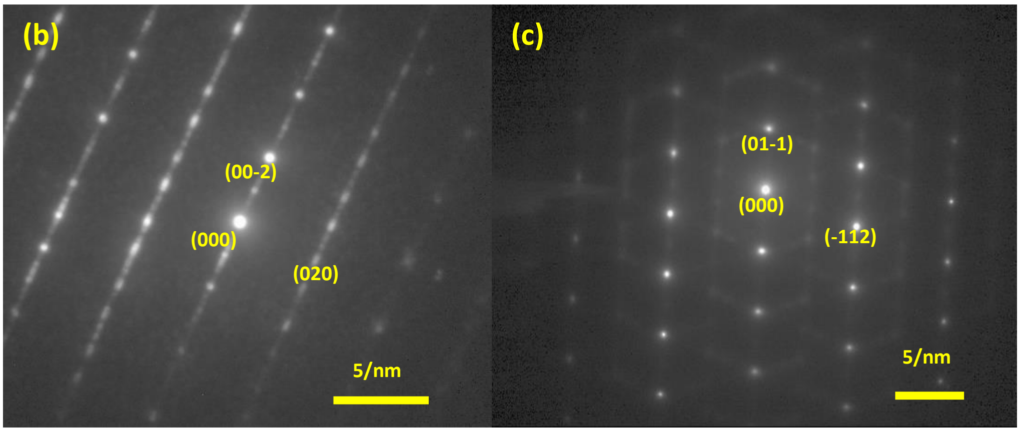

Figure 4.4. (a) Bright Field TEM image showing laths of α“ (martensite with orthorhombic structure) in a β-Ti matrix (body-centered cubic structure); (b) SAED pattern of the α“ martensite laths (zone axis: [100]); (c) SAED pattern of the β-Ti matrix at [311] zone axis.

It is possible to see streaking of diffraction spots. It occurs because the martensite laths are formed by very thin layers. The β-Ti matrix is also indexed in the SAED (Figure 4.4c). Therefore, the as-cast samples presented a two-phase microstructure, a β-Ti matrix, with a body-centered cubic structure and α” martensitic laths, with orthorhombic structure. Although suction casting is recognized as a high solidification process, a microsegregation resulted in a second phase formation in regions were the alloying content was different than in the matrix. The very fine martensitic laths and low volume fraction is the reason for not been possible to identify α” in the XRD experiments.

In order to study grain size, morphology and orientation, the microstructure of the as-cast samples was further investigated by electron back-scattered diffraction (EBSD) experiments. The analysis was performed at the middle of the sample, which was cut in the longitudinal direction (y-z, mould long axis). The inverse-pole figures (IPF) (Figure 4.5a-c) and pole figure in the {100}, {110} and {111} stereographic planes (Figure 4.5d) show that the grains are randomly oriented, absent of crystallographic texture. As in the XRD patterns, a β-Ti single phase was indexed in the EBSD experiment, which is related to low volume fraction and grain size of the α” martensitic laths, as seen in the TEM image. The crystallographic grain size of the β phase was determined from the EBSD experiments, and the linear intercept procedure was applied (ASTM E112). On this way, the mean transversal linear intercept length, $\overline{l}_t$, and mean longitudinal linear intercept length, $\overline{l}_l$, were determined and both were equal to 120 µm, which is related to the equiaxial grain structure of the as-cast sample.

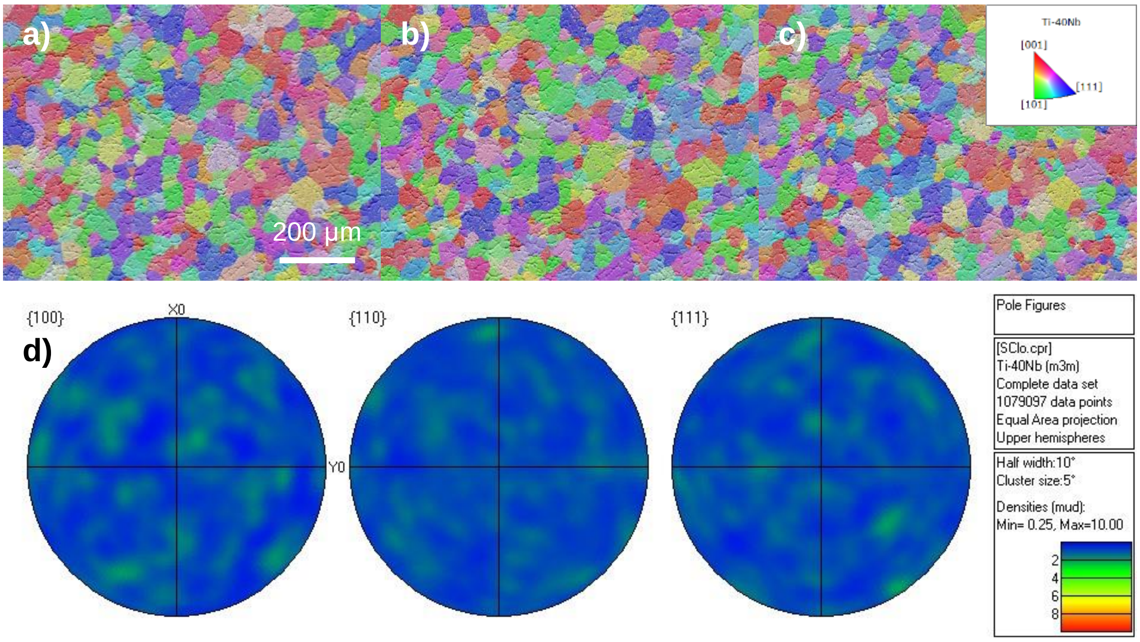

Figure 4.5. Electron back-scattered diffraction maps of an as-cast sample (*TNZT-as-cast*): Inverse-pole figure (IPF) in the x- (a), y- (b) and z- (c) axis, and pole figure in the {100}, {110} and {111} stereographic planes (d). The inset is the IPF orientation reference.

4.1.2 Homogenization heat treatment of suction-cast cylinders

In order to homogenize the microstructure and eliminate the microsegregation of the suction-casted samples of the TNZT alloy, a homogenization heat treatment was applied on the as-cast rods at 1000 °C for 24 h under Ar atmosphere, followed by water quenching. The crystal structure identified in the XRD pattern of the homogenized samples is β single phase (Figure 4.6) and, therefore, the heat treatment and following fast cooling resulted in a β metastable structure at room temperature, similarly to previously reported results [30]. Qazi et al. (2005) also shown a β single phase structure in solution-treated samples of the Ti-35Nb-7Zr-5Ta (wt%) alloy, with varying oxygen content for different treatment temperatures: 850°C (600 ppm), 840°C (4600 ppm), and 900°C (6800 ppm), heat-treated for 1 h followed by water quenching. An average grain size of 28, 23, and 60 µm, respectively, was reported by the authors [108].

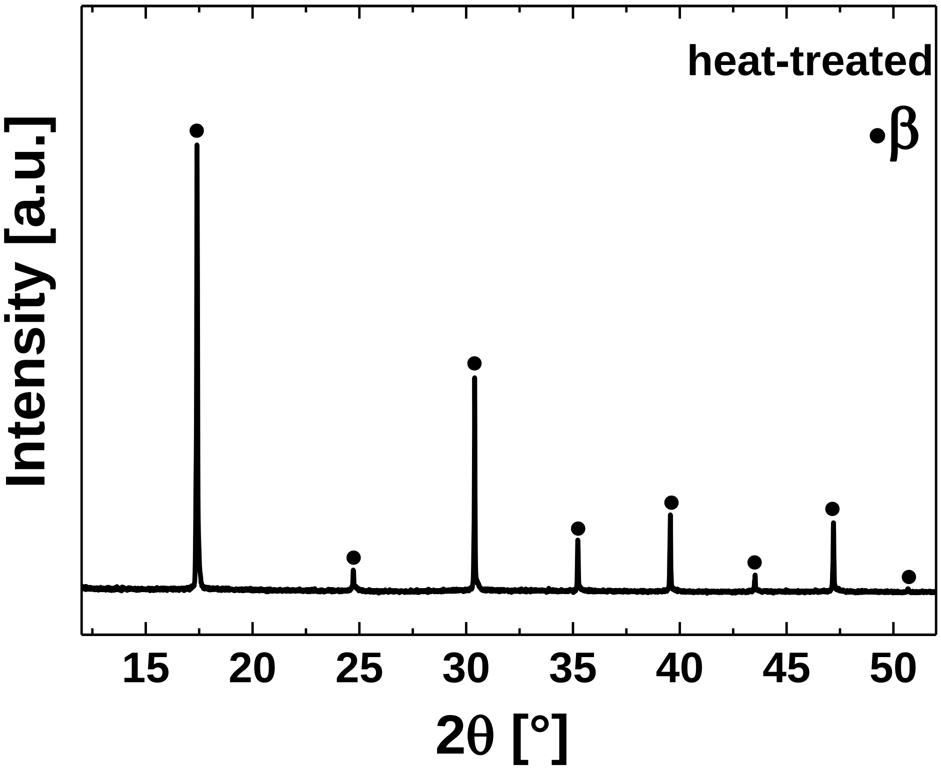

Figure 4.6. Diffractogram of the suction-casted sample submitted to a homogenization heat treatment at 1000 °C for 24 h, followed by water quenching.

An important outcome of the heat treatment was the chemical homogenization of the samples: The microstructure observed by scanning electron microscope with a back-scattered electrons (BSE) detector shows a homogeneous chemical distribution (Figure 4.7). Therefore, the solute redistribution obtained during the heat treatment was maintained in the subsequent cooling step, which is related to the high cooling rate imposed by water quenching the samples compared to suction casting, avoiding Ti depletion of the matrix. On this way, a second phase formation such as α” is less likely and the β single phase structure at room temperature is obtained [88, 111].

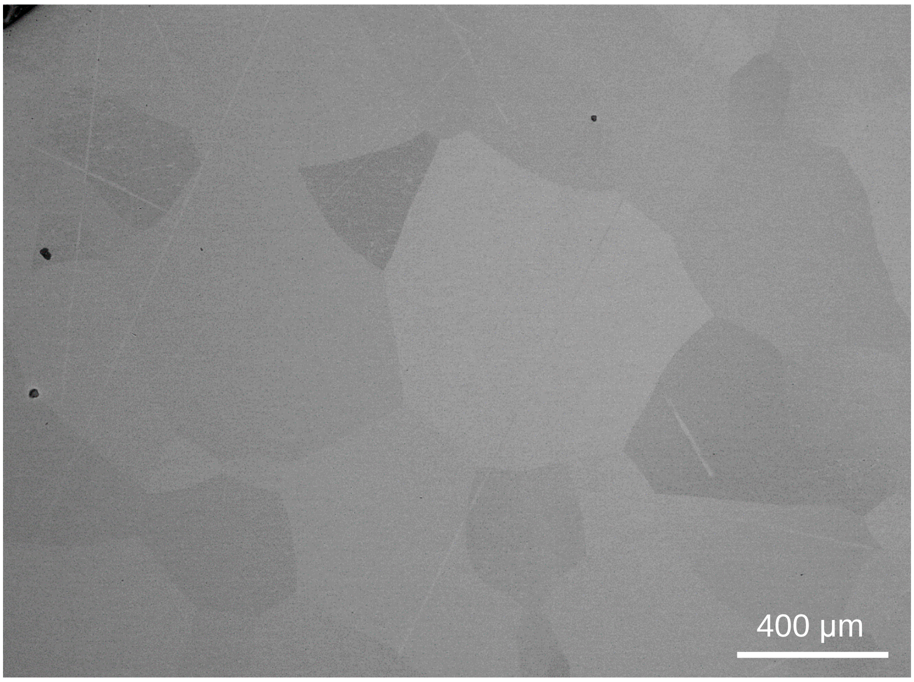

Figure 4.7. Micrograph of the suction-casted sample submitted to a homogenization heat-treatment at 1000 °C for 24 h, followed by water quenching, obtained with a scanning electron microscope in the BSE mode.

The homogenization heat treatment induced significant grain growth. This is an effect of an isothermal heat treatment of the samples at β phase region for long time, enough for the dendritic arms to merge as equiaxed grains [84]. Nonetheless, a heterogeneous grain structure is observed in the sample with coarse and fine grains (Figure 4.7 and 4.8). For the heat-treated samples, the grain size was determined by the comparison procedure following the ASTM E112-13 Standard: an ASTM grain size number, G = 1, was obtained, which means an average grain diameter of approximately 250 µm. Tahara et al. (2010) also reported significant grain growth in samples of Ti-35Nb-7Zr-5Ta (wt%) submitted to cold rolling, followed by recrystallization annealing at 900 °C for 1 h, resulting in a β single-phase microstructure with average grain size of

100 µm [31]. Meanwhile, Yaofeng (2014) reported an average grain size of 200 µm in a β single phase microstructure of a Ti-38Nb-4Sn (wt%) alloy, annealed at 1000 °C for 5 h, followed by furnace cooling [107].

The microstructure of the heat-treated samples was also analyzed by EBSD. The IPF maps (Figure 4.8a-c) show the absence of preferential orientation and, therefore, crystallographic texture is not observed. In addition, β-Ti single phase was indexed in the EBSD experiment, corroborating with the XRD patterns.

Figure 4.8. Electron back-scattered diffraction maps of a suction-casted sample of the TNZT alloy submitted to homogenization heat-treatment: Inverse-pole figure (IPF) in the x- (a), y- (b) and z- (c) axis. The inset is the IPF orientation reference.

4.1.3 Mechanical properties of as-cast and heat-treated samples

Compression tests in monotonic and cyclic modes were conducted on Ø 3 mm cylindrical specimens (aspect ratio ≈ 2), and the Young's modulus, E, yield strength (stress at 0.2% strain offset), σ_{YS}, and compressive stress at 35% strain, $\sigma_{35\%}$, were obtained (Table 4.2). The monotonic and cyclic uniaxial compression tests were performed on three specimens obtained from the as-cast and heat-treated TNZT samples at room temperature. The cyclic uniaxial compression test was carried out by loading-unloading the specimens up to 6.5% of strain on steps of 0.5% in order to attest the pseudolasticity of the specimens. The pseudoelasticity was defined as the maximum recoverable strain, ε_{se}, in the cyclic compression tests [31, 85]. The overall quality and internal soundness of the specimens from the as-cast rods were evaluated before the compression test, and, therefore, density measurements (Archimedes principle) and X-ray computed micro-tomography (µ-XCT) were performed: The as-cast samples presented a density of (5.75 ± 0.03) g/cm³ and a relative volume of 100.0%.

Table 4.2. Comparison of compression properties of the Ti-35Nb-7Zr-5Ta (wt%) alloy, in as-cast and heat-treated conditions.

Sample	**σ_{YS} (MPa)**	**$\sigma_{\varepsilon=35\%}$ (MPa)**	**E (GPa)**	**ε_{se} (%)**
TNZT-as-cast	469 ± 42	686 ± 76	48 ± 4	1.5
TNZT-heat-treated	517 ± 66	787 ± 24	59 ± 14	0.5
Ti-44.5Nb[88]	479 ± 60	-	67 ± 8	0
Ti–35Nb–5Zr–5Ta[31]	≈ 400*	-	-	0
Ti–35.3Nb–7.1Zr–5.1Ta[26]	550 ± 10	-	63 ± 2	-
Ti-35Nb-7Zr-5Ta-0.06O[98]	530	-	-	-
Ti-35Nb-7Zr-5Ta-0.16O[28]	669	-	-	-

*The yield strength was obtained from the stress-strain curve.

The first important result obtained in the monotonic compression test is the Young's modulus: a low value is obtained for the Cu-mould suction-casted specimens (*TNZT-as-cast*), E = (48 ± 4) GPa, with a higher Young's modulus in the homogenized (*TNZT-heat-treated*) specimens, E = (59 ± 14) GPa (Table 4.2). This is a highly desirable property for metallic implants, since it provides higher biomechanical compatibility, as the mismatch of elastic properties of an implant made of a such low Young's modulus alloy and the bone is reduced [15, 16]. Elias et al. (2006) reported an elastic modulus of 50 GPa for the Ti–35.3Nb–7.1Zr–5.1Ta (wt%) alloy. Some other works report a Young's modulus of 50-70 GPa [26-31] for alloys with same nominal composition. Elias et al. (2006) state that these values should be taken carefully, since the alloy shown a non-linear elastic behavior [26, 84].

The true stress-true strain curves of representative specimens from the as-cast and heat-treated conditions are presented (Figure 4.9). A continuous yielding is observed in the as-cast sample, and a sharp yield point is detected in the specimen submitted to homogenization heat treatment. Bönisch (2016) found similar results in a Ti-44.5Nb (wt%) alloy [84]. The non-continuos yield point is a phenomenon normally observed in interstitial solid solute strengthened alloys with body-centered cubic (BCC) structure, and it is related to interactions between interstitial solute atoms and dislocations in the onset of the plastic deformation of alloys, an effect known as Cottrell atmosphere, resulting in higher mechanical strength [109-111].

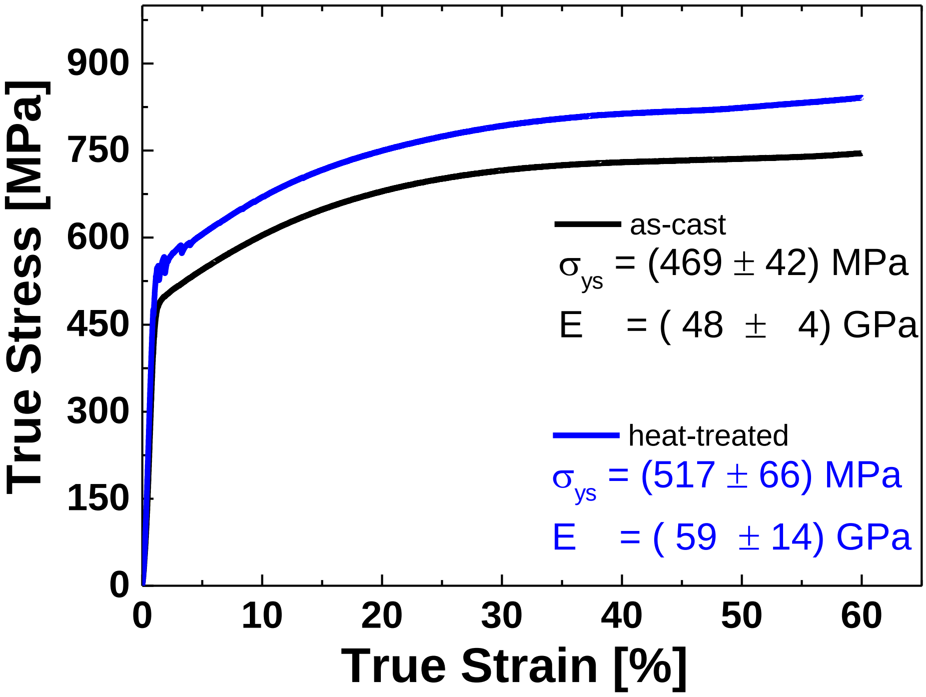

Figure 4.9. True stress-true strain curves of samples of the TNZT alloy produced by Cu-mould suction casting and submitted to homogenization heat-treatment.

The yield strength, σ_{YS}, and compressive stress at 35% strain, $\sigma_{35\%}$, are obtained from the compression tests for as-cast and heat-treated samples. On both conditions, the samples presented compressive strain above 60%, and the test had to be interrupted due to strain measurement issues, without breaking the specimens. The specimens in the heat-treated condition shown a higher mechanical resistance under compression (σ_{YS} = 517 MPa and $\sigma_{35\%}$ = 787 MPa) than the as-cast sample (σ_{YS} = 469 MPa and $\sigma_{35\%}$ = 686 MPa), and some strain hardening is observed for either cases, opposed to an elastic perfectly plastic behavior previously reported [26]. In the as-cast condition, a two-phase structure is observed: β-Ti matrix with α” laths. The grain structure was different on both conditions: the grain size was approximately two-fold greater in the heat-treated samples than in the as-cast samples. Therefore, in order to explain the compression properties of these samples, three important facts should be considered:

i) The homogenization heat treatment resulted in a solute redistribution, which was maintained in the subsequent water quenching. This caused a more powerful solid solute strengthening of the β-Ti phase, increasing the mechanical resistance of the alloy;

ii) The strengthening effect of fine martensitic laths in β-Ti alloys [25, 27, 84, 85] was not so evident, which should be related to a low volume fraction of α”;

iii) The heat treatment was performed at 1000 °C for 24 h, followed by water quenching. Although the samples were encapsulated in argon and the furnace atmosphere was kept with pure argon (99.99% of purity) throughout the whole treatment, the high affinity of the alloy may have led to oxygen pickup. In addition, it has been demonstrated that water quenching of Ti-Nb alloys induced higher oxygen content in the samples [107]. It is widely recognized that oxygen is an important interstitial solid solution strengthener of β-Ti alloys, and, therefore, a broad range of yield strength is achievable for Ti-35Nb-7Zr-5Ta (wt%) by controlling the oxygen content [28, 31, 108]. Therefore, a higher solid solution strengthening effect on the heat-treated condition, both by substitutional solid solution and especially by interstitial solid solution effect of oxygen, may have led to higher compressive stress in samples of the TNZT alloy submitted to heat treatment.

The pseudoelasticity of the Ti-35Nb-7Zr-5Ta (wt%) alloy produced by Cu-mould suction casting and submitted to homogenization heat-treatment was obtained by the recoverable strain, ε_{se}, in cyclic compression tests (Figure 4.10).

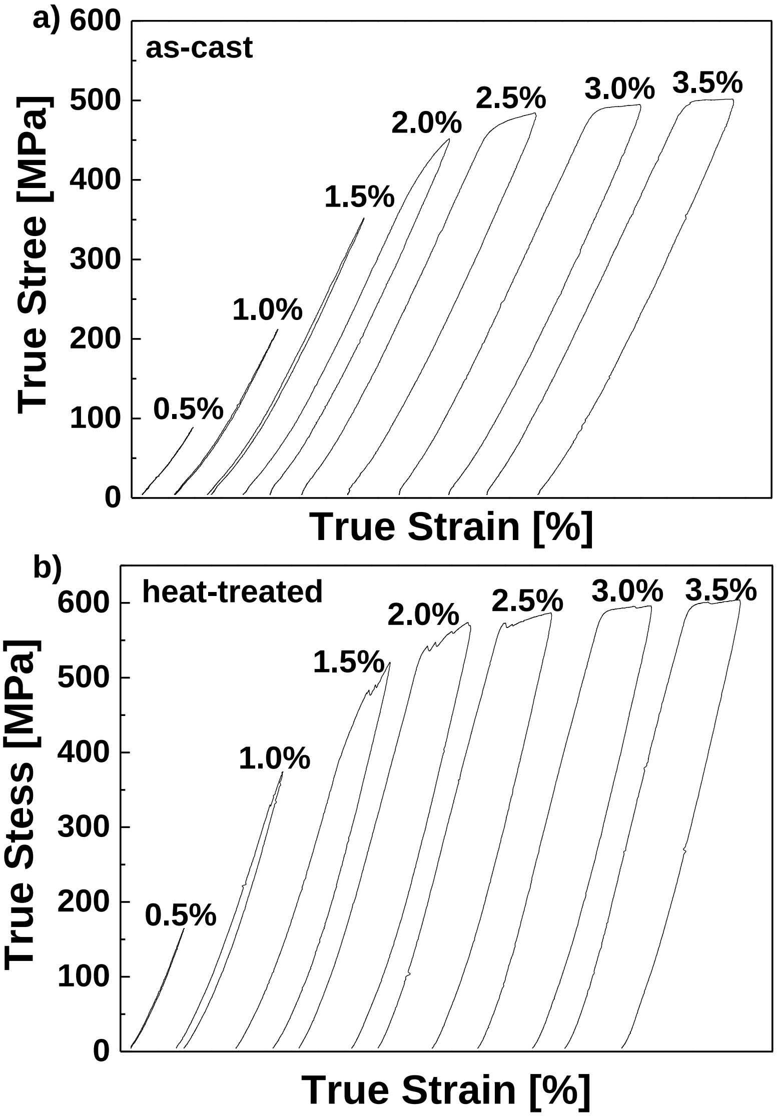

Figure 4.10. True stress-true strain curves obtained in cyclic compression tests of specimens of the TNZT alloy in the as-cast (a) and heat-treated (b) conditions.

It is known that the pseudoelastic behavior is based in a recoverable stress-induced austenite-martensite phase transformation, which is dependent on the chemical composition of the Ti-Nb-based alloy and the thermomechanical history of the sample [25, 27, 87].

In case of the as-cast samples, a recoverable strain ε_{se} = 1.5% is observed (Figure 4.10a), while in the homogenized specimens, the recoverable strain was limited to the first step of 0.5% strain (Figure 4.10b). For a binary alloy Ti-40Nb (wt%), a recoverable strain of 2.5% was reported at room temperature [25, 27], and Tahara et al. (2010) reported an elastic recoverable strain, ε_{se}, of 3.0% in a Ti–35Nb–5Zr–5Ta (wt%) annealed at 600 °C for 1 h after cold rolling [31]. Two competitive deformation mechanisms exist in Ti-Nb alloys: stress-induced martensitic transformation and permanent plastic deformation, with the dislocation structure playing a decisive role. The mechanism with lower critical stress starts first, which in turn decrease the extent of the other deformation mechanism [25, 27, 84, 85, 88]. Both as-cast and heat-treated samples have substitutional solid solution as main strengthening mechanism, although higher oxygen content may have had an important effect in the heat-treated samples. Therefore, the plastic deformation is possibly more favored than the stress-induced martensitic transformation, resulting in a modest pseudoelasticity of the samples.

4.2 Processing the Ti-35Nb-7Zr-5Ta (wt%) Alloy by Selective Laser Melting

4.2.1 Powder properties

The chemical composition of the powder, obtained via wet-chemical analysis (ICP-OES and CGHE), is Ti-34.5Nb-6.5Zr-4.5Ta-0.02O (wt%), with a slight difference from the nominal chemical composition and from the as-cast samples, although the oxygen content in the powder is lower than in the as-cast condition (Table 4.3). The bulk chemical analysis of Ti, Nb, Zr and Ta in the as-cast samples was performed by ICP-OES (Table 5.3).

Table 4.3. Chemical analysis of the Ti-35Nb-7Zr-5Ta (wt%) powder and as-cast samples.

Sample	**Ti (wt%)**	**Nb (wt%)**	**Zr (wt%)**	**Ta (wt%)**	**O (ppm)**
TNZT-as-cast	53.4 ± 0.5	34.7 ± 0.5	7.1 ± 0.3	4.6 ± 3.4	900 ± 30
TNZT-powder	53.9 ± 0.4	34.5 ± 0.3	6.5 ± 0.4	4.5 ± 0.4	160 ± 10

The phase constitution of the gas-atomized TNZT powder was investigated by XRD. It is noticed the resulting pattern of a β single phase structure (Figure 4.11). A similar result was observed in a gas-atomized Ti-42.6Nb (wt%) powder [112] and the high cooling rate associated to the gas atomization of the TNZT alloy, with a high content of β stabilizing elements, resulted in a β structure at room temperature.

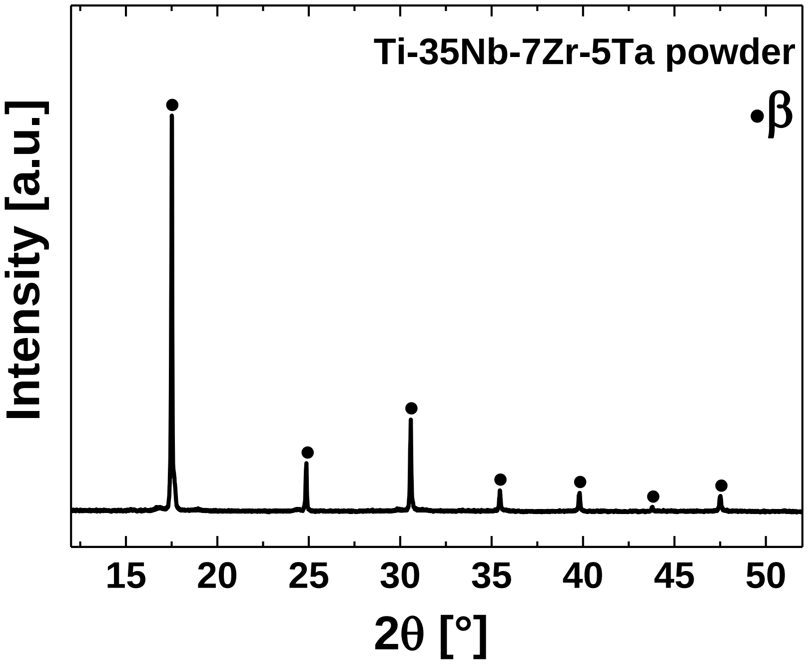

Figure 4.11. Diffractogram of the *TNZT-powder used* in the selective laser melting experiments.

The *TNZT-powder* was further characterized by TEM, and a β single phase structure was indexed in the SAED pattern (Figure 4.12), corroborating with the XRD pattern.

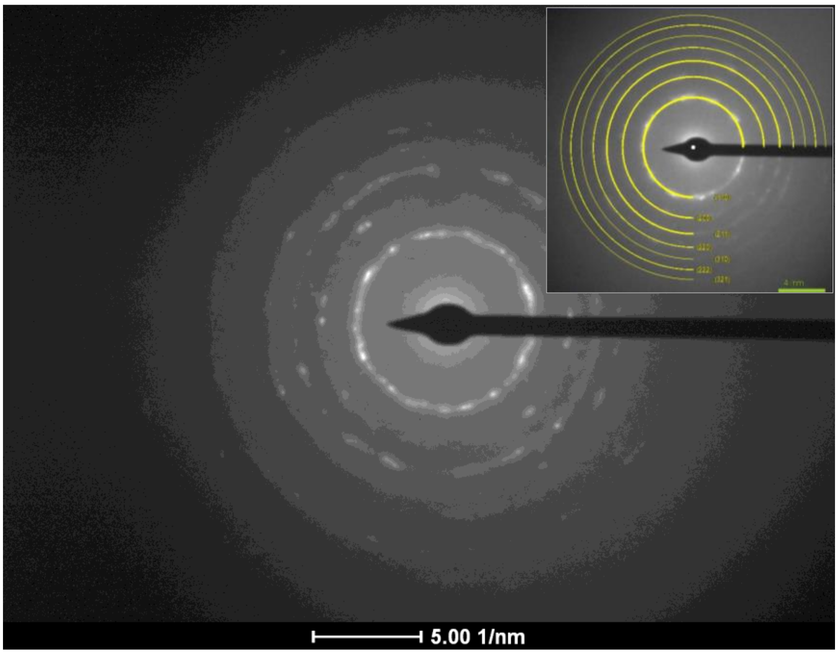

Figure 4.12. Selected area electron diffraction (SAED) pattern of β-Ti structure in the *TNZT-powder*.

The powder was analyzed by X-ray computed micro-tomography (μ-XCT) and a cross section of the powder sample is presented (Figure 4.13a). The morphology of the powder is mainly spherical. It may be also noticed that some particles appear brighter than others. This is directly related to the chemical composition of the particle: elements with higher atomic mass (Nb and Ta, for instance), when exposed to X-ray absorbs more energy, resulting in the contrast observed in the image. The same explanation applies for pores: as the voids are filled with air, the interaction with X-ray yields black spots in the image (no energy absorption), and, therefore, pores are not observed in the tomography of the powder.

The morphology of the powder is further assessed by scanning electron microscopy (SEM). The powder discloses spherical shape (Figure 4.13b), with a smooth surface without cracks (inset in Figure 4.13b). A slight presence of satellites is observed, which is related to particles adherence to the surfaces of larger ones due to collisions during atomization. Those features are somehow common seen in gas-atomized powders of Ti and Ti-based alloys [44, 112]. Pores or voids within the particle are not observed. In addition, chemical microanalysis in a sample of powder metallographically prepared was performed with the energy-dispersive X-ray (EDX) detector in the SEM (Figure 4.13c-f). The results seen in the μ-XCT image is confirmed: a chemical inhomogeneity in the TNZT powder particles is noticed, with some particles richer in Ti-Ta and lower content or absent of Nb and Zr.

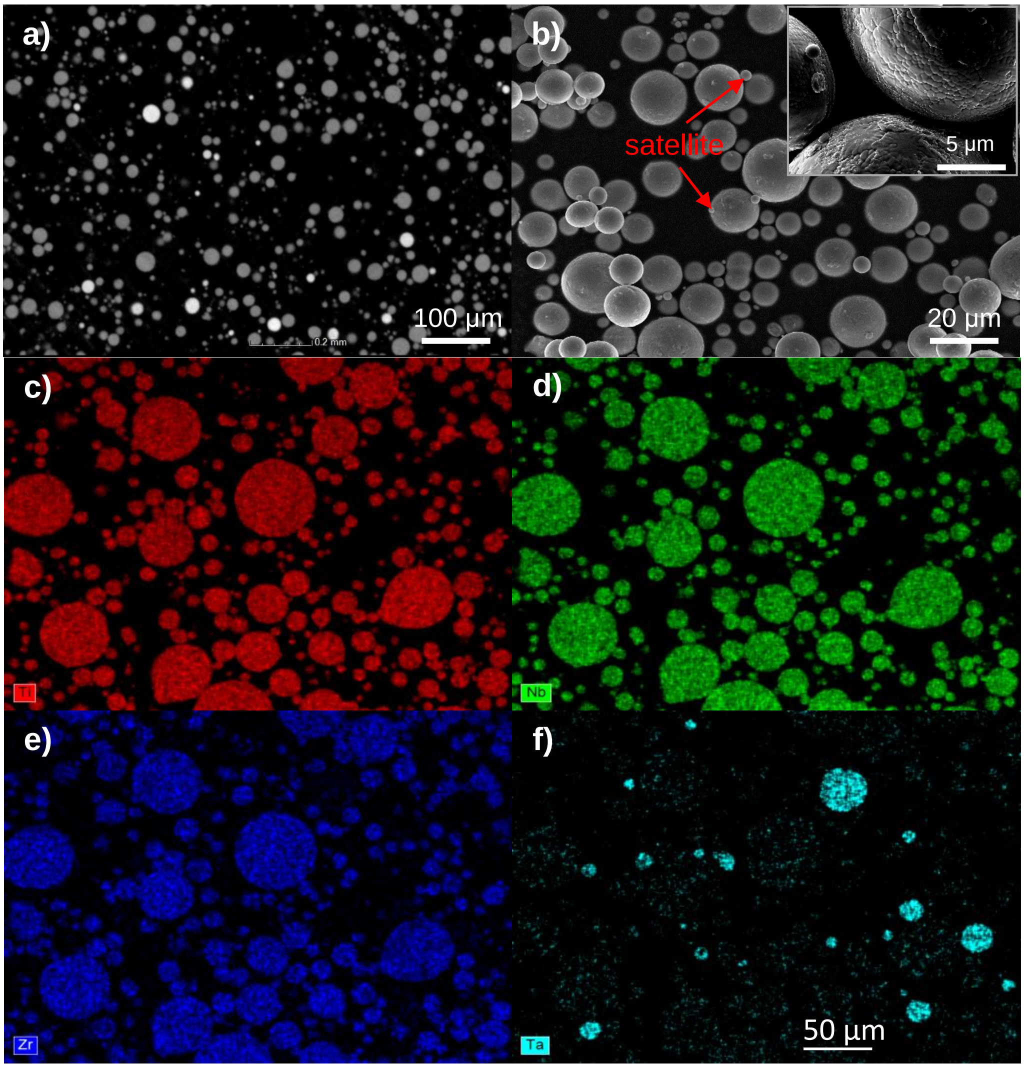

Figure 4.13. μ-XCT slice image of the powder (a); SEM image of the gas-atomized TNZT powder (b) and EDX maps in a metallographically prepared sample (c-f).

Furthermore, it is known that selective laser melting requires powder characteristics which are important for ensuring reproducibility and repeatability. The main characteristics of the powder for SLM are particle size and shape, surface morphology, composition and internal porosity, which dictates the powder flowability and packing behavior. These powder characteristics impact the bulk material properties of the fabricated component such as density and porosity [41-44]. The particle size distribution of the TNZT-powder (PSD) used in the selective laser melting was assessed by μ-XCT and is plotted in Figure 4.14a as relative and cumulative frequencies of the equivalent spherical diameter, which approximates the particle to an equivalent sphere [44].

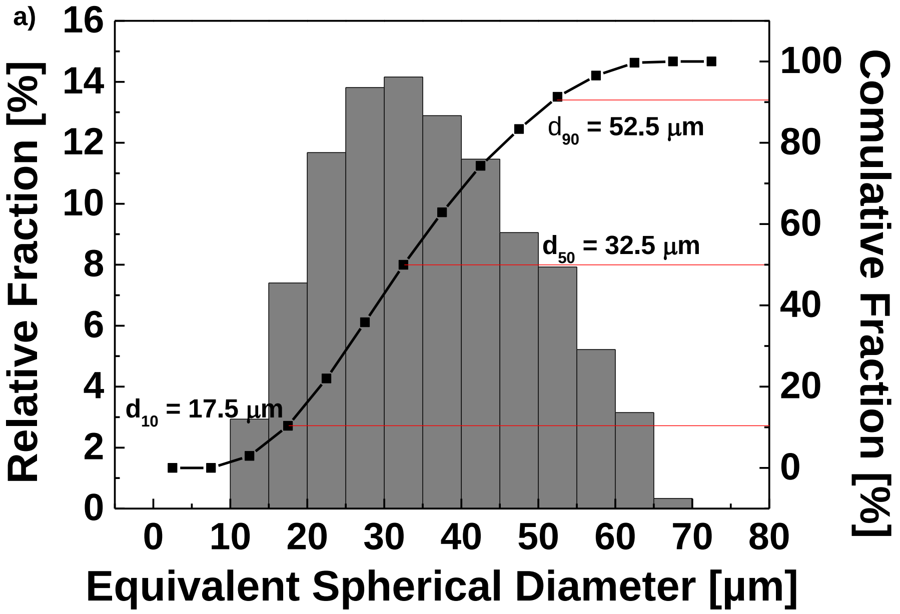

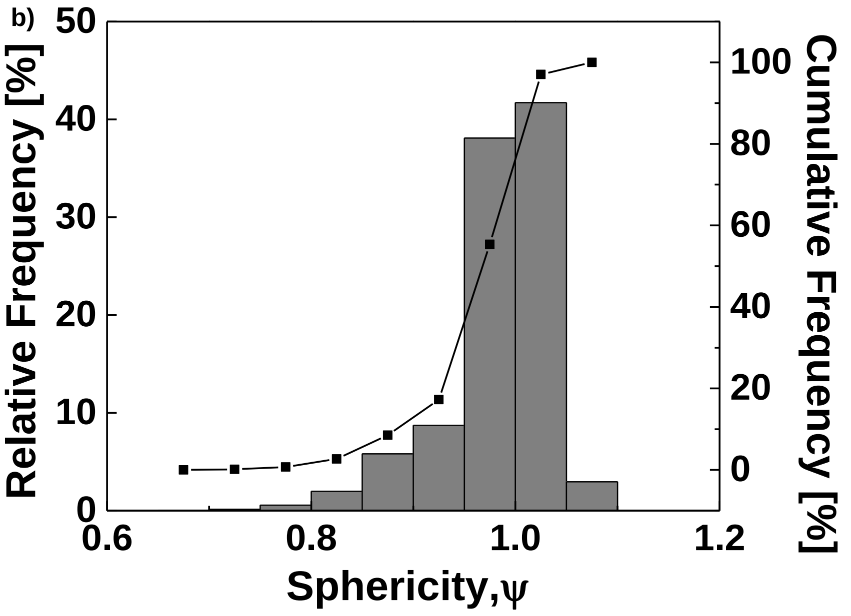

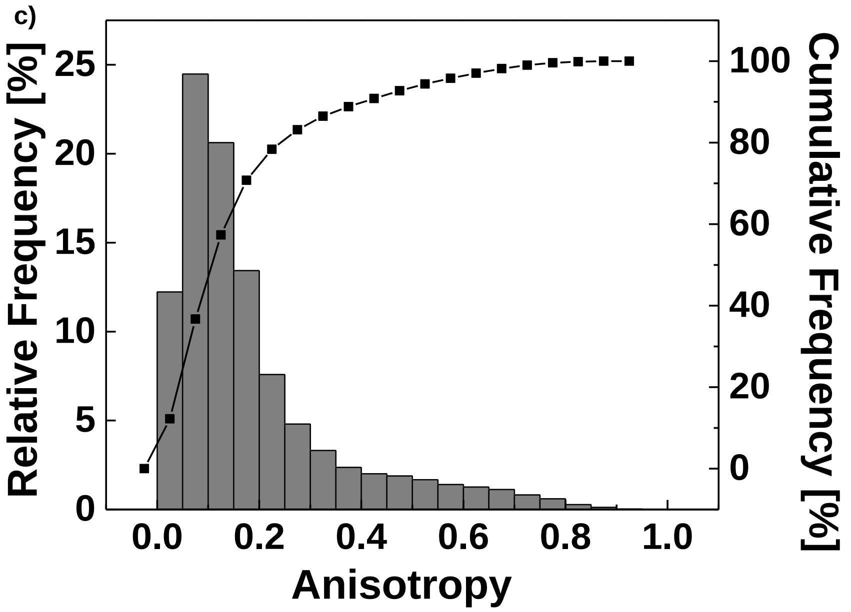

Figure 4.14. (a) Particle size distribution (PSD) of the TNZT powder used in the selective laser melting process; (b) sphericity (c) and anisotropy of the particles.

The PSD follows a Gaussian distribution, slightly positively skewed (dislocated to the left, predominantly small particles), with d_{50} = 32.5 μm. The 10th and 90th percentile of particles, d_{10} = 17.5 μm and d_{90} = 52.5 μm, demonstrate a narrow particle size distribution of the TNZT powder, normally desirable to be used in selective laser melting: the ratio $d_{90}/d_{10} = 3$, means a good balance of small particles that results in higher densification with coarse particles which improves the powder flowability during the recoating step in the selective laser melting process [44, 112-116]. The sphericity, Ψ, (Figure 4.14b) and anisotropy (Figure 4.14c) of the powder particles are also plotted. It is noticed the majority of particles present sphericity, $\Psi = 1$, and are predominantly isotropic (ratio of particle width, W, and particle length, L, equal to 1).

4.2.2 Parameters Optimization

Selective laser melting is a complex transformation process, which follows a routine from a “line” to a “layer” and to a “bulk” [4]. In order to attest the processability of the Ti-35Nb-7Zr-5Ta (wt%) alloy by selective laser melting and identify the optimum processing parameters to manufacture highly densified bulk samples of the TNZT alloy, single tracks (20 mm of length) are firstly produced using two different laser power 61 and 129 W and varying the scanning speed between 0.30 and 4.0 m/s. The aspects related to the quality of the tracks are of utmost importance in defining the optimized SLM parameters. The tracks must be uniform and continuous [117-120]. In the case of single tracks produced with 61 W and scanning speed of 0.75 m/s discontinuities and the balling effect occurs, as result of melt pool instability (Figure 4.15a). With a laser power of 129 W, discontinuities appear on single tracks of the TNZT alloy with scanning speed of 1.0 m/s (Figure 4.15b). The linear energy input effect on the track widths is investigated and the correlation between the linear energy input and track width shows that the track width increases as the scanning speed decreases in a similar fashion for both laser power used (Figure 4.16). As scanning speed is reduced in a fixed laser power, the energy applied to the powder is higher, resulting in a wider melt pool [117-120].

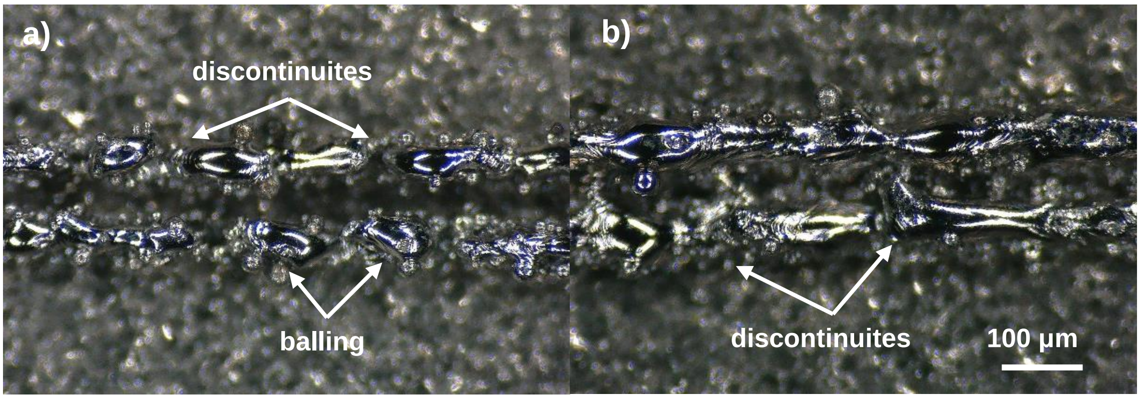

Figure 4.15. Deposited single tracks by selective laser melting of the TNZT powder, with laser power 61 W and scanning speed 0.75 m/s (a) and 129 W and scanning speed 1.0 m/s (b).

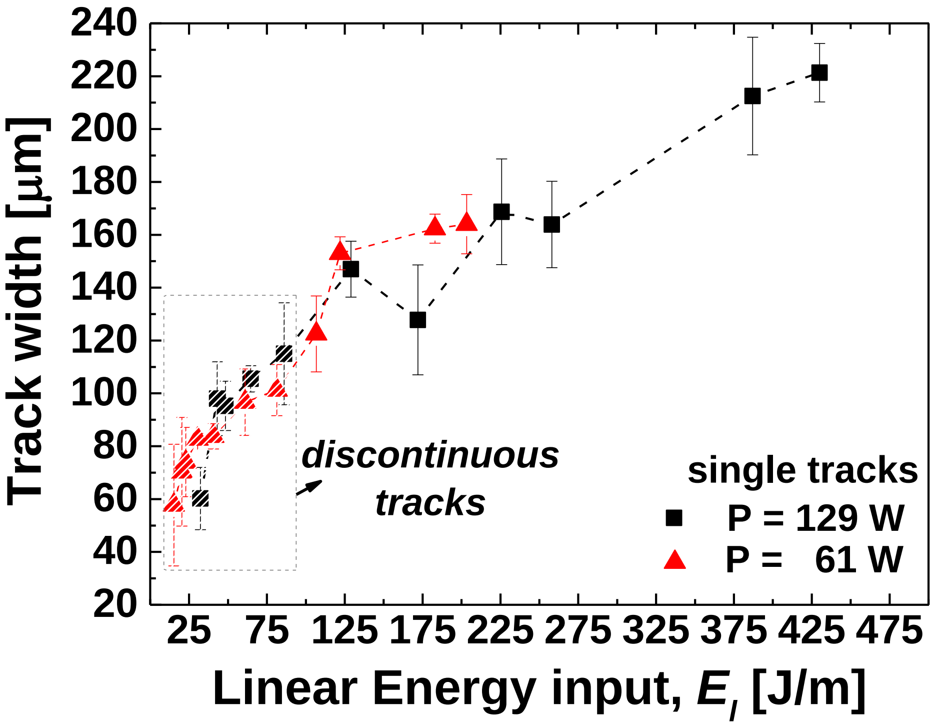

Figure 4.16. Track width as a function of linear energy input of single tracks of the Ti-35Nb-7Zr-5Ta (wt%) powder (SLM single tracks), with laser power 61 and 129 W and varying scanning speed from 0.30-4.0 m/s. The linear energy input is given by: $E_l = P_l/v_s$.

Outer-shell of cylinders (SLM-contours) with 3 mm external diameter and 6 mm height were melted without defining a hatching distance. This sample geometry was selected since the contours resemble more closely bulk samples than single tracks. The laser power was kept 129 W with scanning speed in the range 0.33-4.00 m/s. The same relationship between scanning speed and wall thickness is obtained: as the scanning speed increases, the contours' wall thickness decreases, which is related to the SLM processing parameters, the alloy itself and, therefore, the melt pool [117, 118]. The micrographs of the contours are shown in Figure 4.17.

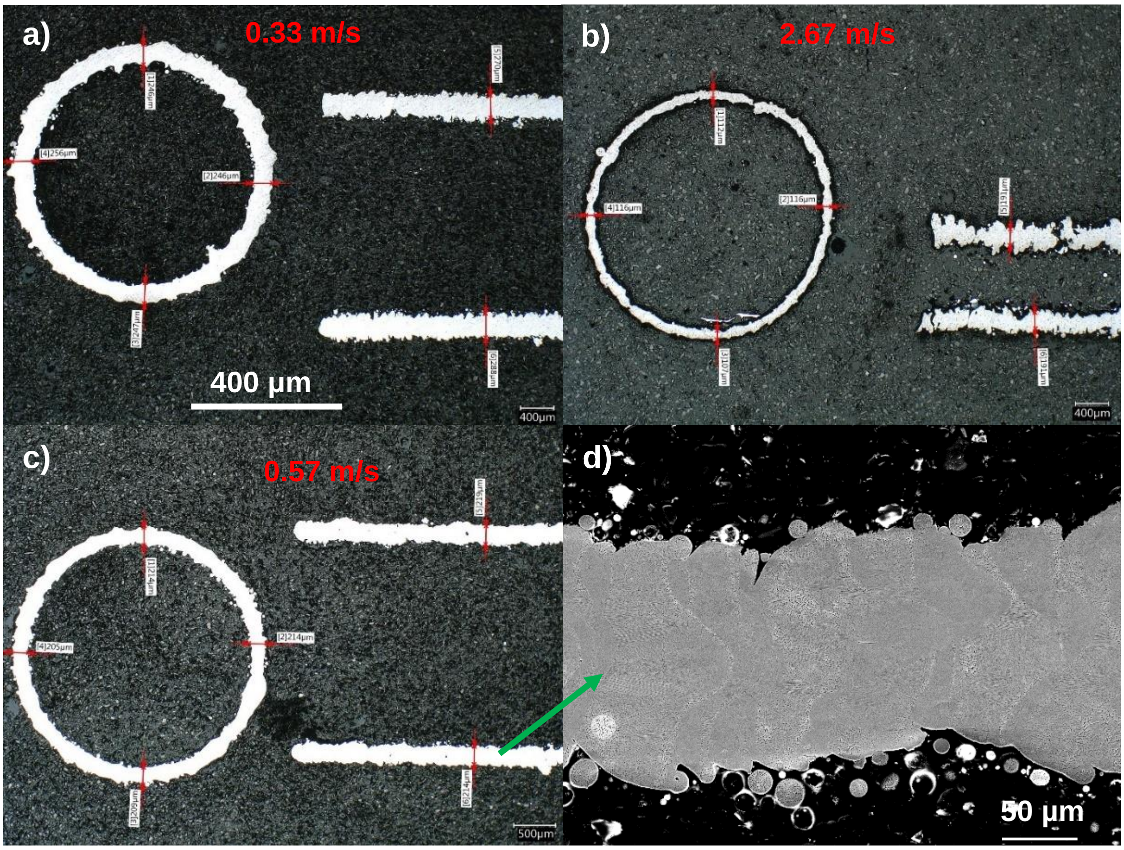

Figure 4.17. Micrographs of SLM-contours of the Ti-35Nb-7Zr-5Ta (wt%) alloy manufactured by selective laser melting, with 129 W and varying scanning speed: 0.33 m/s (a); 2.67 m/s (b); 0.57 m/s (c) and SEM image of the contour produced with 0.57 m/s (d).

The thickness, uniformity and continuity of the contours were assessed by optical and scanning electron microscopy. On this manner, the stability (stable, unstable, and balling) and shape of the melt paths could be assessed. A wide and continuous wall thickness with a width of (267 ± 13) µm is formed, characterized by an irregular track at scanning speed of 0.33 m/s (Figure 4.17a), which corresponds to a linear energy input of 387 J/m. The higher linear energy input leads to an increase of the melt pool volume with a lower liquid melt viscosity, resulting in irregularities on the contour [117, 118]. A scanning speed of 0.57 m/s leads to a track width of (215 ± 11) µm, with a uniform and smooth surface (Figure 4.17c and d). If the energy input becomes 48 J/m (P_L = 129 W, v_s = 2.7 m/s), a track width of (161 ± 24) µm is formed, discontinuities and the so-called balling effect appear in the melted track (Figure 4.17b). A further decrease of the linear energy input (32 J/m) at the highest scanning speed of 4.00 m/s leads to a smaller melt volume and the energy input is no longer enough to melt the powder.

In the next step and based on single tracks and contours evaluation, bulk samples (Figure 4.18) were produced with scanning speed of 0.33, 0.57 and 2.67 m/s, and overlapping of 25, 50 and 75% on each scanning speed, while keeping the laser power of 129 W, layer thickness of 40 µm and unidirectional scanning strategy with 79° scanning vector rotation between successive layers (cross-hatching).

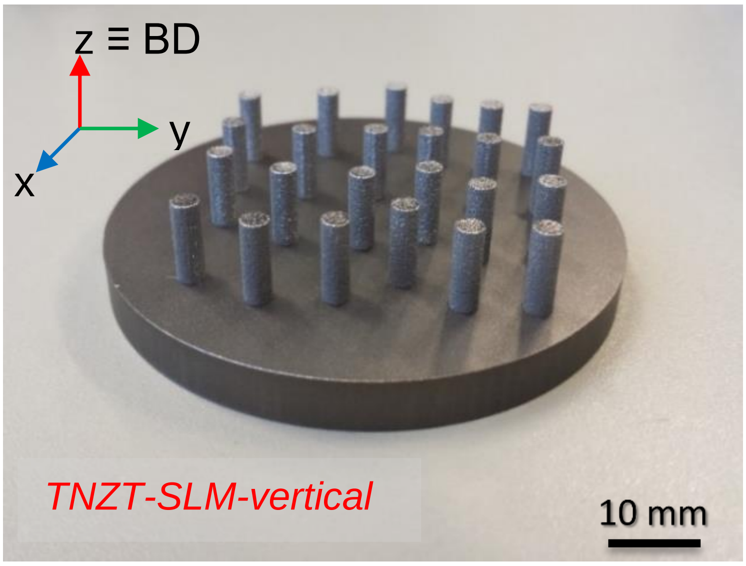

Figure 4.18. Bulk cylinders of the TNZT alloy manufactured by selective laser melting. BD is the building direction.

Next, the hatching distance (distance between tracks) is further optimized keeping the scanning speed at 0.57 m/s and an overlapping range of 10-75%. Therefore, the energy input was varied in a broad range and its effect on densification of the bulk samples is evaluated.

The porosity of the as-built cylinders was evaluated by means of X-ray computed micro-tomography (μ-XCT). The density of the samples is measured by the Archimedes technique and related to the Cu-mould suction-cast sample with porosity < 0.01%. The results are plotted as function of the volumetric energy input, E_v (Figure 4.19).

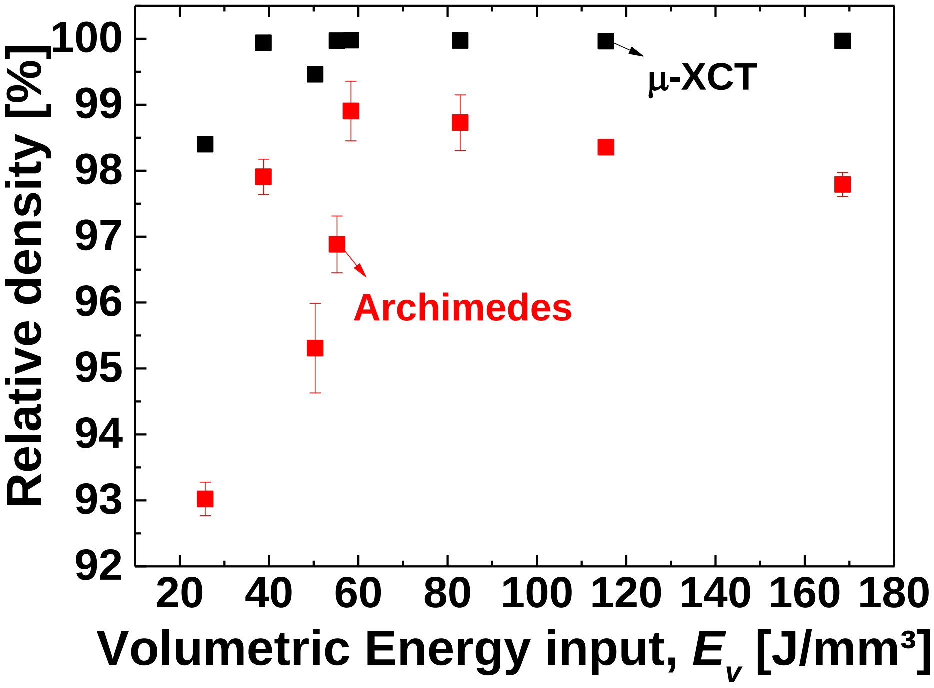

Figure 4.19. Dependence of relative density of bulk samples measured by Archimedes technique and computed micro-tomography (μ-XCT) on energy input of selective laser melted samples. The volumetric energy input is given by: $E_v = \frac{P_l}{v_s h_s l_z}$.

The relative densities of the specimens (Archimedean) are within 93.0-99.0% and the relative density obtained from μ-XCT reconstruction amounts to 98.4%–99.9%. The results for the two techniques deviate, with greater relative density measured by tomography, which is related to the fact that the μ-XCT technique has a limited resolution. Furthermore, the surface roughness of the as-built cylinders, results in air bubbles sticking to the sample surface during the density measurements by Archimedean method, which can also influence the measured density of the samples. The surface roughness is related to the melt pool stability, and the higher the scanning speed the less stable is the melt pool, which may explain the greater discrepancies in the relative densities of samples produced with lower energy input.

In order to produce samples with highest density, an optimal combination of laser power, scanning speed, layer thickness, and hatching distance (converted here to overlapping) is required to minimize porosity [40, 50, 52]. As was seen, the powder presented practically no voids or porosities and, therefore, powder-induced porosity is not observed in the selective laser melted parts. The porosity is high in samples produced with scanning speed of 2.67 m/s and overlapping of 50%, resulting in an energy input of 25.7 J/mm^3, which is not enough to completely melt the powder, resulting in samples with the lowest relative density of 93.0% of the as-cast reference sample (Figure 4.20a and b). It is known that pores induced by processing technique, known as process-induced porosity, are formed when the applied energy is not enough for complete melting or spatter ejection occurs. These pores are typically non-spherical due to a lack of fusion and appear in a variety of sizes (sub-micron to macroscopic), which may be identified with un-melted powder particles visible in or near the pore [2, 3, 7, 9, 11, 38-40]. This is the case of the samples produced with lowest energy input (*TNZT-LE*).

Furthermore, it may be noticed that samples produced with higher energy not necessarily presented higher density. This is because when the energy input is too high, spatter ejection may occur in a process known as keyhole formation, resulting in higher porosity due to powder evaporation in the melt pool [2, 3, 7, 9, 11, 38-40]. This is the case of samples produced with highest energy input of 168.5 J/mm^3 (*TNZT-HE*), with a scanning speed of 0.33 m/s and overlapping of 75%, resulting in a density of 97.8% relative to the reference sample (Figure 4.20c and d). The maximum density of bulk samples is attained when the scanning speed of 0.57 m/s and overlapping of 50% are adjusted to the laser power of 129 W, layer thickness of 40 µm and unidirectional hatching strategy 79° rotation between layers, resulting in an energy input of 58.3 J/mm³ (*TNZT-SLM-vertical*). With this set of parameters, the part achieved the highest density of 99.0% relative to the as-cast reference sample (Archimedean method), and pores are hardly seen in the microstructure (Figure 4.20e and f). This is recognized as the optimized parameters set for selective laser melting of the Ti-35Nb-7Zr-5Ta (wt%) alloy on this work.

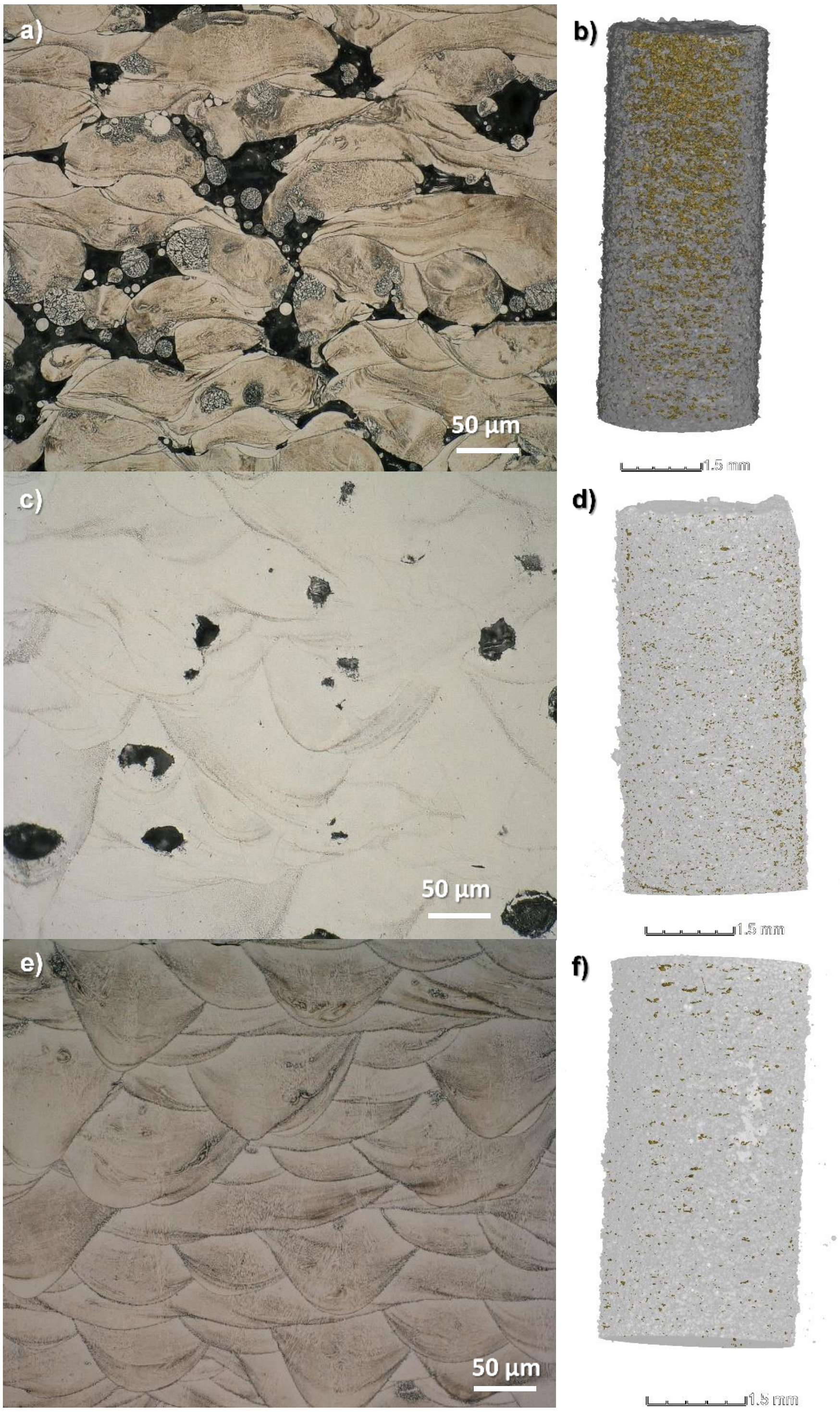

Figure 4.20. Micrographs and µ-XCT reconstructed 3D images of the selective laser melted samples produced with 129 W and three set of parameters: (a) and (b) 2.67 m/s, 50%, 25.7 J/mm³ (*TNZT-LE*); (c) and (d) 0.33 m/s, 75%, 168.5 J/mm³ (*TNZT-HE*) and (e) and (f) 0.57 m/s, 50%, 58.3 J/mm³ (*TNZT-SLM-vertical*).

4.2.3 Microstructure of bulk samples of the Ti-35Nb-7Zr-5Ta (wt%) alloy manufactured by selective laser melting

The chemical composition of the *TNZT-SLM-vertical* sample, obtained via wet-chemical analysis (ICP-OES and CGHE), is shown in Table 4.3. The composition of the samples is approximately equal to the *TNZT-powder* composition. An oxygen pickup is observed in the selective laser melted samples. Nonetheless, the oxygen content in the *TNZT-SLM-vertical* sample is approximately equal to the *TNZT-as-cast* sample, and within the alloy specification [28].

Table 4.3. Chemical analysis of the TNZT powder, as-cast and as-built samples.

Sample	**Ti (wt%)**	**Nb (wt%)**	**Zr (wt%)**	**Ta (wt%)**	**O (ppm)**
TNZT-as-cast	53.4 ± 0.6	34.7 ± 0.5	7.1 ± 0.3	4.6 ± 3.4	900 ± 30
TNZT-powder	53.9 ± 0.4	34.5 ± 0.3	6.5 ± 0.4	4.5 ± 0.4	160 ± 10
TNZT-SLM-vertical	53.3 ± 0.3	34.1 ± 0.3	6.4 ± 0.3	5.5 ± 0.7	990 ± 20

The phase constitution of the selective laser melted bulk samples of the TNZT alloy was analyzed by X-ray diffraction and the resulting pattern of a representative sample is shown in Figure 4.21. A β single-phase structure is identified in the as-built sample, which means that the high cooling rate of SLM led to fully stabilized β phase in the Ti-35Nb-7Zr-5Ta (wt%) alloy at room temperature. Therefore, it is seen that the selective laser melting process maintained the crystal structure of the powder, similarly to results reported in selective laser melting of a Ti-42Nb (wt%) [112] and a Ti-45Nb powder [82]. Zhang et al (2018) reported that a Ti-30Nb-5Ta-3Zr (wt%) processed by SLM consisted of a majority β phase and a minority of α” phase, which is related to the lower amount of β stabilizing elements, especially Nb content, than the alloy investigated on the present work [121].

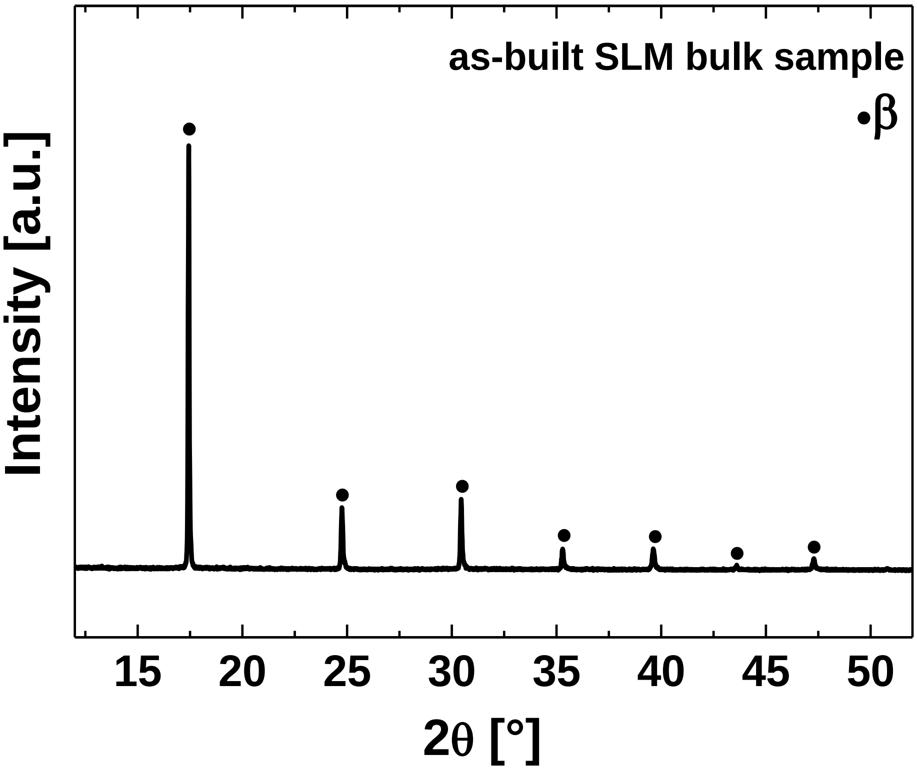

Figure 4.21. Diffractogram of the *TNZT-SLM-vertical* sample produced by selective laser melting.

The microstructure of the as-built sample produced by SLM with the optimized parameters set (*TNZT-SLM-vertical*) is shown in metallographic prepared samples of the building direction cross-section (Figure 4.22a-b), with a semiquantitative chemical analysis obtained by energy-dispersive X-ray spectroscopy (EDX) microanalysis (Figure 4.22c-f). The melt pools are clearly observed and the melt pool boundaries are identified in the micrograph, which is related to microsegregations (dash lines in Figure 4.22a) and has been observed in micrographs of other systems, e.g., AlSi10Mg, 316L, 18Ni300 maraging steel, and Inconel 718, produced by SLM [36].

The overview image (Figure 4.22a) shows that the as-built sample is homogeneously densified. The chemical contrast of the image obtained in SEM with BSE detector shows some brighter regions in the part, related to elements with higher atomic mass, seen in more detail in Figure 5.22b.

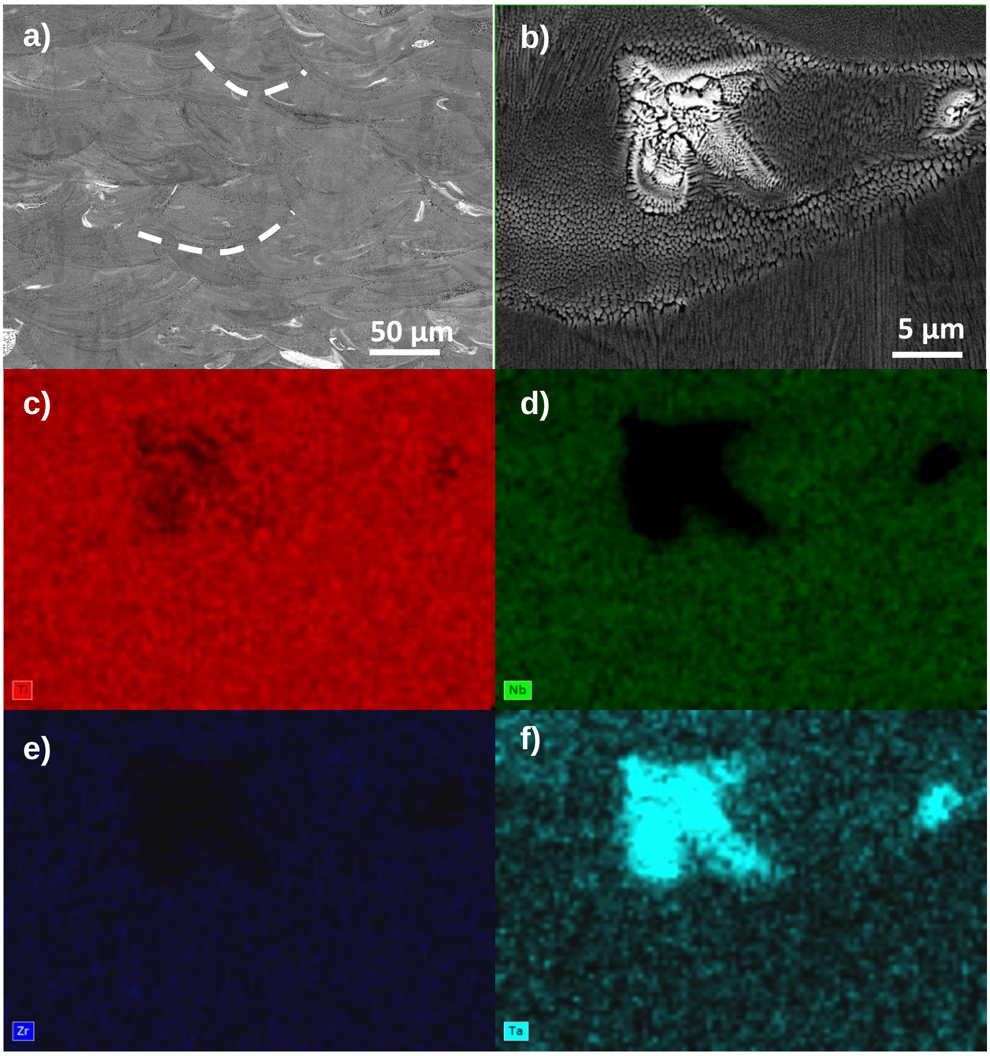

Figure 4.22. Microstructure of as-built sample produced by SLM (*TNZT-SLM-vertical*) observed with scanning electron microscopy: (a) Chemical contrast obtained by back-scattered electrons (BSE); (b) secondary electron image of a Ta-enriched region (c-f) and energy-dispersive X-ray spectroscopy (EDX) maps.

With the EDX maps, it is confirmed that Ta-enriched powder particles, which were detected in the TNZT-powder characterization, results in Ta-enriched regions of the SLM part, as they are not completed dissolved in the matrix. A similar result is reported by Sing et al (2018), with a Ti-Ta alloy processed by selective laser melting. The authors report that fully dense Ti-Ta parts were produced, with laser power of 360 W, scan speed of 400 mm/s, powder layer thickness of 50 µm and hatch spacing of 125 µm, resulting in an energy input of 144 J/mm^3, which is higher than the energy input used in the present work to produce high density bulk TNZT samples (58.3 J/mm³). Nonetheless, it was reported that un-melted Ta particles are observed and a further increase in energy density is necessary to completly melt tantalum particles, due to the high melting point of tantalum (3020 °C) [122].

The solidification structure of the SLM samples is shown in Figure 4.23. It is seen that the solidification microstructure of the as-built selective laser melted samples is distinct from the Cu-mould suction-cast sample: A fine columnar-dendritic structure is observed in the SLM samples (Figure 4.23a) and an equiaxed dendritic structure was seen in the as-cast samples. It is reported that such columnar-dendritic structures are widely observed solidification microstructures in additive manufacturing of metals, and it is related to thermal gradients on the order of 10^6 K/m and cooling rates of the order of 10^6 K/s of the selective laser melting process [7, 11, 38, 39, 66, 74, 112, 123]. About the two mentioned parameters, the thermal gradient in the liquid G_L has influence on the solidification front stability and it is material dependent: it is higher for low conductive materials (e.g., Ti and its alloys). It is also dependent on the process, as it is known to be higher for high energy input processes such as laser or electron beam melting.

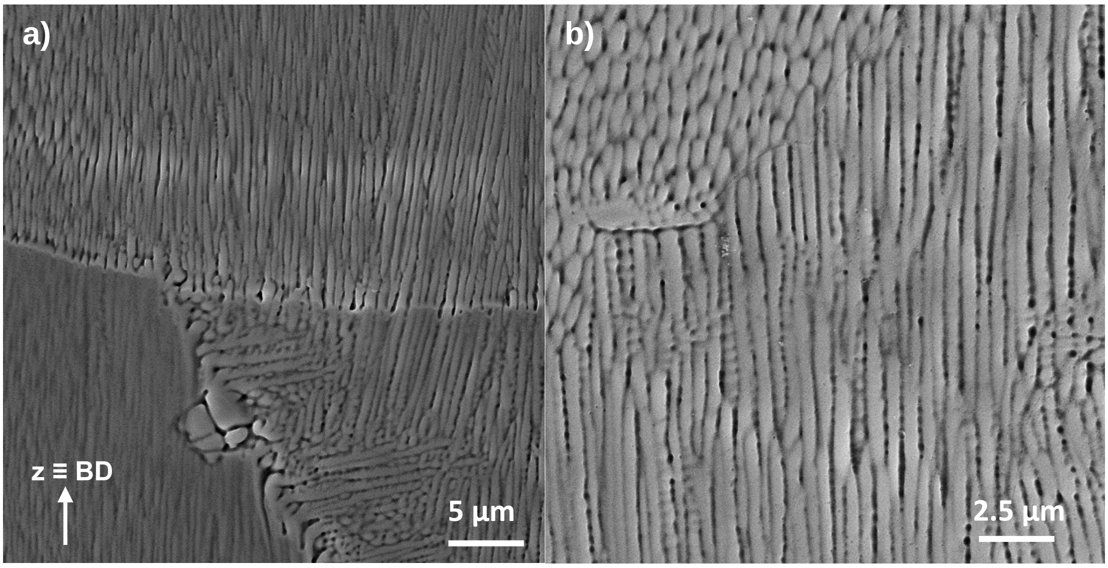

Figure 4.23. Solidification structure of as-built samples of the TNZT alloy produced by selective laser melting: (a) competitive growth of dendrites with epitaxial growth; (b) columnar dendritic structure inside the melt pool.

For polycrystalline materials, the grain growth direction is parallel to the maximum heat flow direction, which is normal to the solidifying surface of the melt pool [58] Therefore, columnar grains grow from the boundary of the melt pool towards the center along location dependent directions during solidification in selective laser melting of the Ti-35Nb-7Zr-5Ta (wt%) alloy. On this way, dendrites with easy-growth directions aligned closely with the maximum heat flow direction at the solid/liquid interface achieve competitive growth during the solidification process (Figure 4.23b). Bright field TEM image of the SLM bulk sample, with selected area electron diffraction (SAED) pattern is shown in Figure 4.24. A β-Ti single phase was indexed, corroborating with the XRD patterns.

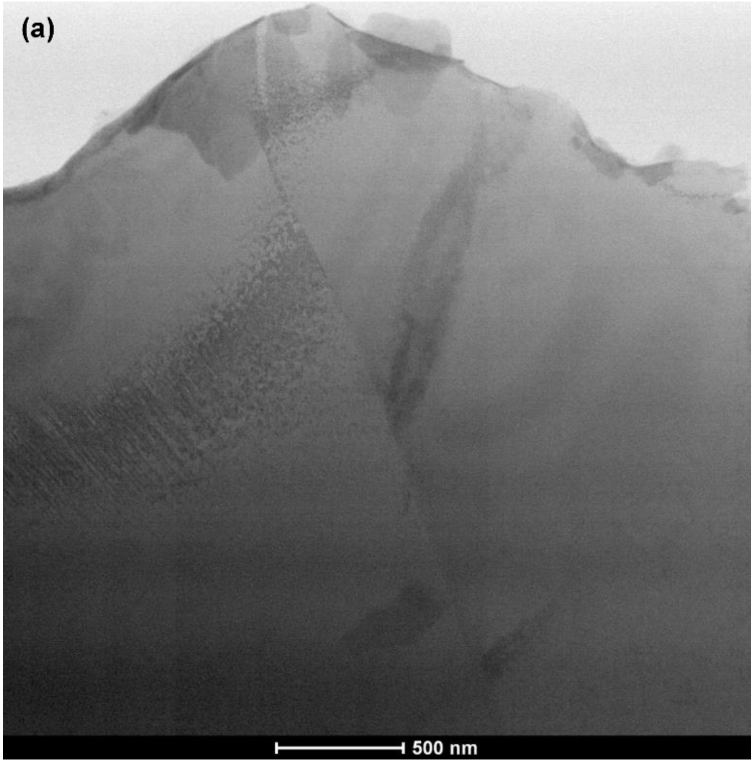

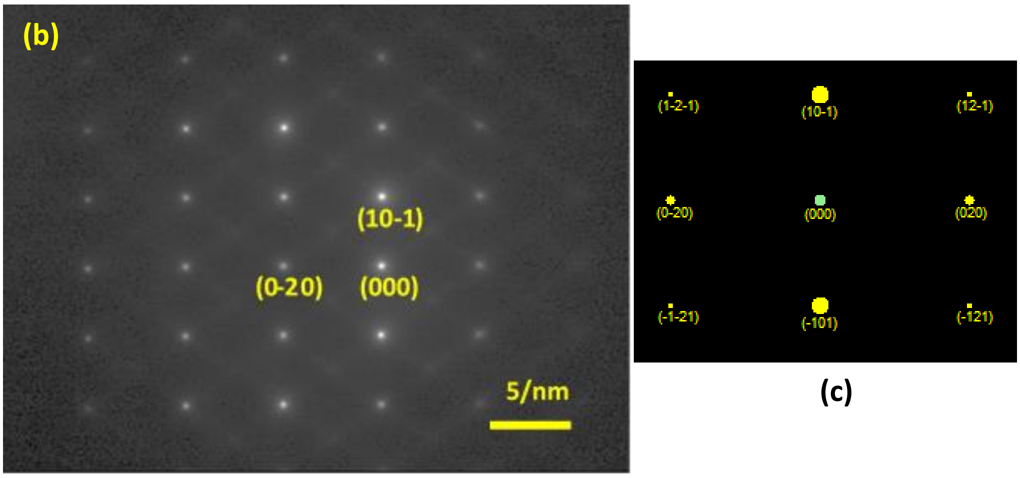

Figure 4.24. (a) Bright Field TEM image; (b) SAED patterns of the β-Ti grains shown in the previous images and (b) simulated SAED pattern for zone axis [101]. The diffractions confirm the presence of only β-Ti.

The grain size, morphology, orientation and crystallographic texture of the as-built SLM samples was further investigated by electron back-scattered diffraction (EBSD) experiments. The analysis was performed at the middle of the sample, which was cut in the longitudinal direction (y-z, building plane). β-Ti single phase was indexed in the EBSD experiment. The inverse-pole figures (IPF) show columnar grains growing epitaxially through several layers, oriented in the building direction (Figure 4.25a-c). In addition, it is observed that the columnar grains are slightly tilted away from the building direction. The explanation is that as the layers are scanned with a rotating scanning strategy, the grain growth is affected in the melt pool for each layer, with a tilting angle dependent on the scanning strategy. Thijs et al. (2010) and Simonelli et al. (2014) observed similar results in SLM of a Ti-6Al-4V (wt%) alloy [8, 124].

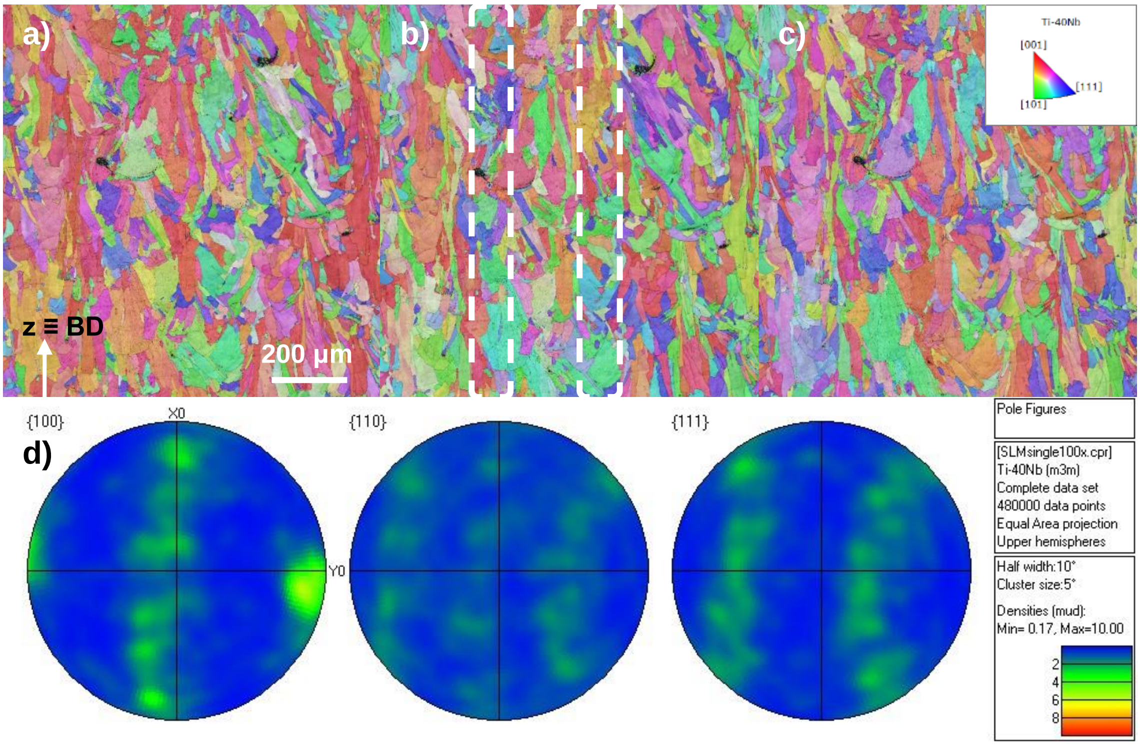

Figure 4.25. Electron back-scattered diffraction maps of as-built SLM sample: Inverse-pole figure (IPF) in the x- (a), y- (b) and z- (c) axis, and pole figure in the {100}, {110} and {111} stereographic planes (d). The inset is the IPF orientation reference.

It is known that grain grows in SLM during solidification from previously deposited layers, and ultimately determines the crystallographic texture of the structure through partial or complete melt-back of the previously formed underlying layer [74]. The growth direction and velocity of the solidification structure of the AM component are dependent on both crystallographic orientation and local heat flow direction [11], and the preferential growth direction for cubic crystals is the <100> direction. The pole figure in the {100}, {110} and {111} stereographic planes (Figure 4.25d) show a crystallographic texture in selective laser melting of the TNZT alloy, with preferential direction of grain growth closely aligned in the <001> build direction, opposed to randomly oriented grains observed in the Cu-mould suction-cast samples. Similar behavior has been reported in a Ti-Nb-Sn [123], Ti-6Al-4V [8, 68, 124] Ti-45Al-2Cr-5Nb [125], Ti–15Mo–5Zr–3Al [126], and Ti-5553 [127] alloys processed by

SLM, with a columnar-dendritic growth along the <100> crystallographic orientation with {001} texture confirmed by the pole figure.

The crystallographic grain size was also determined from the EBSD experiments. Since the grain presents an elongated morphology the linear intercept procedure was applied (ASTM E112-13), and the mean transversal linear intercept length, $\bar{l}_t$ = 72 µm, and mean longitudinal linear intercept length, $\bar{l}_l$ = 327 µm, were determined. This result is related to an epitaxial growth of the columnar grains oriented in the building direction, with grains growing through several layers, since the layer thickness used was 40 µm. Antonysamy et al. (2013) and Thijs et al. (2010) reported columnar grains with 100 µm up to millimeter of length in a Ti-6Al-4V produced by SLM [8, 68]. As a comparison, the $\bar{l}_t = \bar{l}_l$ = 120 µm was obtained in the Cu-mould suction-cast samples, which is directly related to the difference in the solidification conditions of selective laser melting and Cu-mould suction casting techniques. Furthermore, there appears to be a secondary grain formation mode and a fine-grained region is observed between the columnar grains, with no specific texture as seen in the colors of the IPF maps (regions limited by dash lines in Figure 5.25b). This is related to a higher energy input due to overlapping between tracks, where the laser re-melts an adjacent solid track resulting in a higher cooling rate if compared to a track of powder being melted. A similar feature has been reported by in a nickel superalloy [128] and a Cu-11.85Al-3.2Ni-3Mn (wt.%) alloy processed by selective laser melting [120].

4.2.4 Sample orientation and laser remelting effect on the microstructure of SLM samples

Although, the TNZT alloy presents good processability by SLM, the microstructure is formed by columnar grains aligned in the building direction, which is expected to result in considerable mechanical properties anisotropy. Therefore, samples oriented at 0° (*TNZT-0°horizontal*) and 45° (*TNZT-45°degree*) related to the base plate were produced by selective laser melting with the optimized parameters set: laser power 129 W, scanning speed 0.57

m/s, layer thickness 40 µm, 50% of overlapping and unidirectional scanning strategy rotating 79° between each layer (Figure 4.26). The grain size, morphology, orientation and the formation of crystallographic texture were assessed.

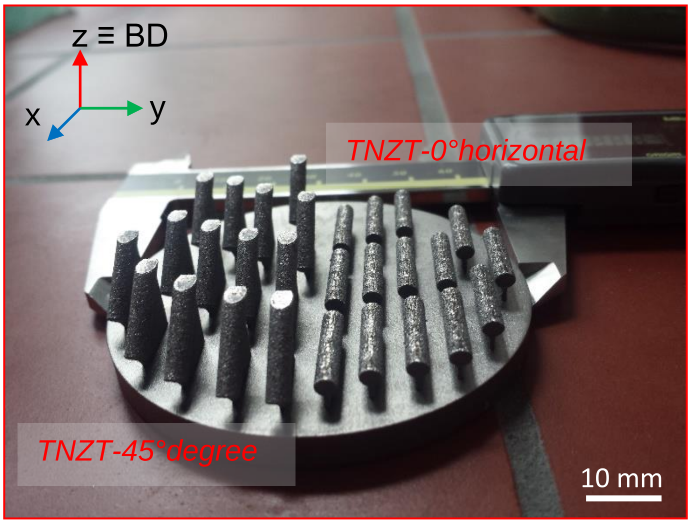

Figure 4.26. Samples of the Ti-35Nb-7Zr-5Ta (wt%) alloy produced by SLM in different orientation. BD is the building direction.

The microstructure of the samples was investigated by electron back-scattered diffraction (EBSD) experiments. The analysis was performed in the y-z building plane. The inverse-pole figure (IPF) in the y-axis (Figure 4.27a-b) and pole figure in the {100}, {110} and {111} stereographic planes (Figure 4.27c-d) are presented. A β-Ti single phase structure was indexed in the EBSD experiment for both conditions.

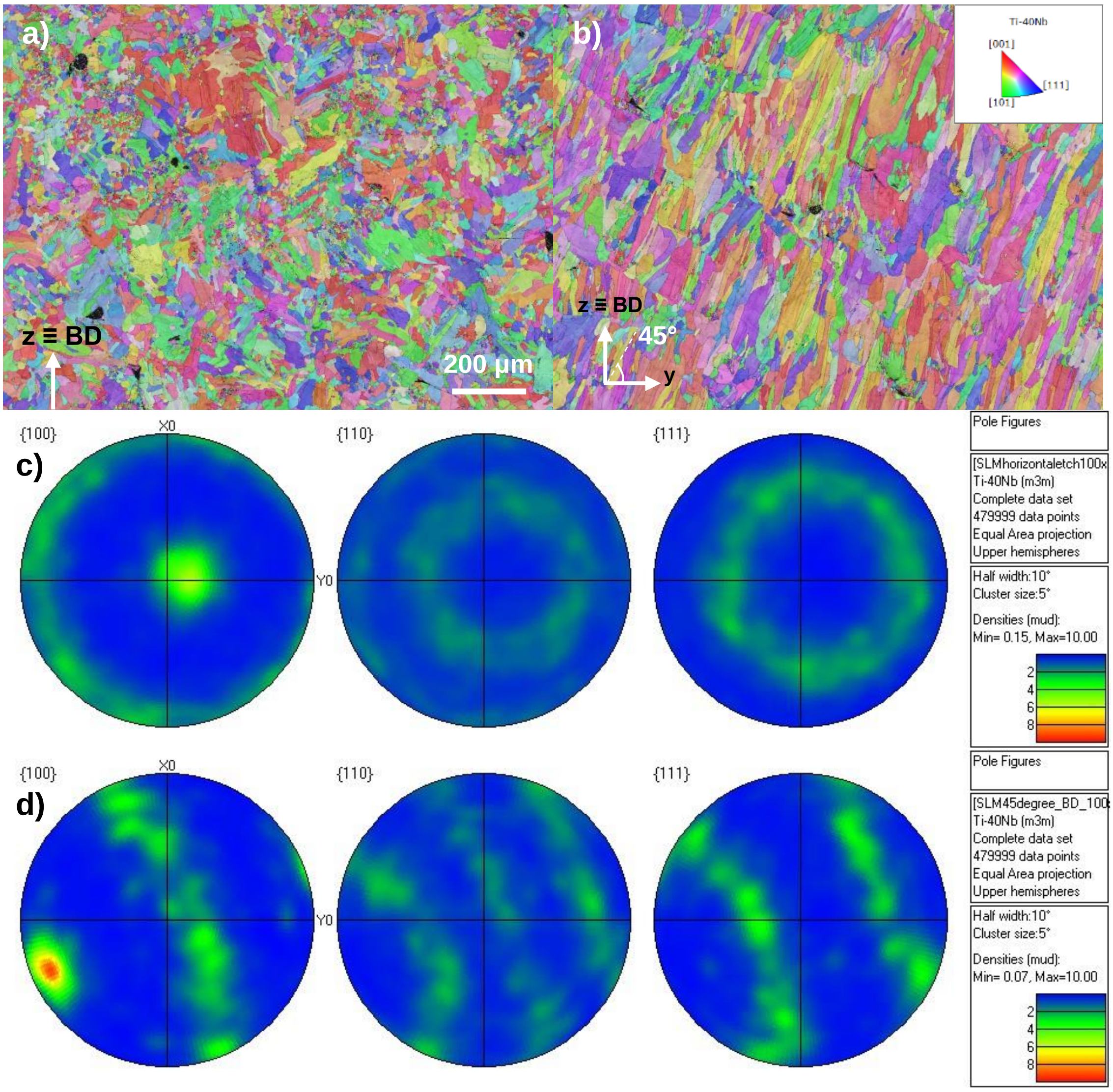

Figure 4.27. Inverse-pole figure (IPF) in the y-axis of samples of the TNZT alloy produced by SLM: (a) *TNZT-horizontal*, (b) *TNZT-45°degree*, and respective pole figures for the (c) *TNZT-0°horizontal* and (d) *TNZT-45°degree* samples. The inset is the IPF orientation reference.

It may be seen that different grain structure and crystallographic textures are developed. For the *TNZT-horizontal* sample a fine grain structure randomly oriented is observed, which confirms the effect of building orientation in the microstructure of selective laser melted samples of the Ti-35Nb-7Zr-5Ta (wt%) alloy. Meanwhile, in the *TNZT-45°degree*, columnar grains are seen growing epitaxially through several layers. On this case, the pole figures (Figure 4.27d) show a similar texture seen in the *TNZT-SLM-vertical* sample, but with a tilting angle, which is a result of the melt-pool directional solidification following the building direction [126].

The crystallographic grain size was determined from the EBSD experiments: The mean longitudinal linear intercept length/mean transversal linear intercept length of the *TNZT-0°horizontal* sample and *TNZT-45°degree* were 115/91 and 129/89, respectively. In the case of the *TNZT-0°horizontal*, a more equiaxed morphology with smaller grain size than in the *TNZT-45°degree* is seen, although on both cases, the mean longitudinal linear intercept length was significantly reduced in comparison *TNZT-SLM-vertical* sample ($\bar{l}_l$ = 327 µm). For the *TNZT-45°degree*, what may explain the finer grain structure (as indicated with the mean longitudinal linear intercept length), is related to the need of supports to sustain the overhanging sample geometry in the SLM process, which affect the thermal history and cooling rate of the samples [129]. Therefore, it shows that the building orientation of the samples in selective laser melting affected the grain size, morphology and orientation, and, therefore, the part properties and their anisotropy could be different according to the manufacturing strategy followed.

The effect of part orientation on the microstructure of selective laser melted samples may be explained as follows. The thermal history in selective laser melting is related to the path the laser follows and, thus, the aspect ratio of a sample relative to the building direction has significant effect on its thermal history [77, 130-133]. Hence, the *TNZT-SLM-vertical* (tall and narrow) and *TNZT-0°horizontal* (short and wide) samples present distinct thermal conditions, affecting the microstructure. In fact, A. Yadollahi et al. (2017) observed that samples of 17-4PH stainless steel built in horizontal and vertical orientations presented distinct microstructure in terms of grain size and phase fractions. [133].

In order to investigate the effect of a laser remelting scanning strategy on the microstructure of samples processed by SLM, a second laser melting step was applied (*TNZT-remelting*). This involves, after scanning a layer and melting the powder, the same layer is scanned again before depositing a new layer of powder [103]. The parameters used were identical to the ones used in the

TNZT-SLM-vertical samples (referred as the optimized SLM parameters set): laser power 129 W, scanning speed 0.57 m/s, layer thickness 40 µm and 50% of overlapping. The laser remelting scanning strategy is aimed at improving the densification and surface finishing of parts produced by selective laser melting. Although, this strategy increases the production time and costs, it has the potential to eliminate post-processing steps as e.g. hot-isostatic pressing [103, 134, 135].

The solidification structure of the SLM samples *TNZT-SLM-vertical* (used here as reference) and *TNZT-remelting* is shown in Figure 4.28. A columnar-dendritic morphology (inset in Figure 4.28) is observed in a β single phase solidification structure (confirmed by XRD).

Some important effects of layer remelting on the part microstructure are detected. Firstly, the Ta-enriched regions are not so evident after applying the remelting step, meaning the higher energy input resulted in a more thorough mixing of Ta in the matrix. In addition, it is seen a shallower melt pool in the *TNZT-remelting* samples. This is related to the fact that the laser remelting step means melting a solid layer, with different thermal diffusivity than a powder layer in a single melting routine [134, 135]. On this sense, the higher thermal conductivity of the solid material resulted in smaller melt pool, a feature also reported on laser remelting of an Al-Si base alloy (A360.0), a M2 tool steel and a 18Ni300 maraging steel [103]. An important aspect is also observed in the solidification structure of the *TNZT-remelting* samples. Although the columnar-dendritic morphology is maintained, a finer structure is formed. In fact, since a solid material is melted in the remelting step, a higher cooling rate is expected, resulting in a finer microstructure.

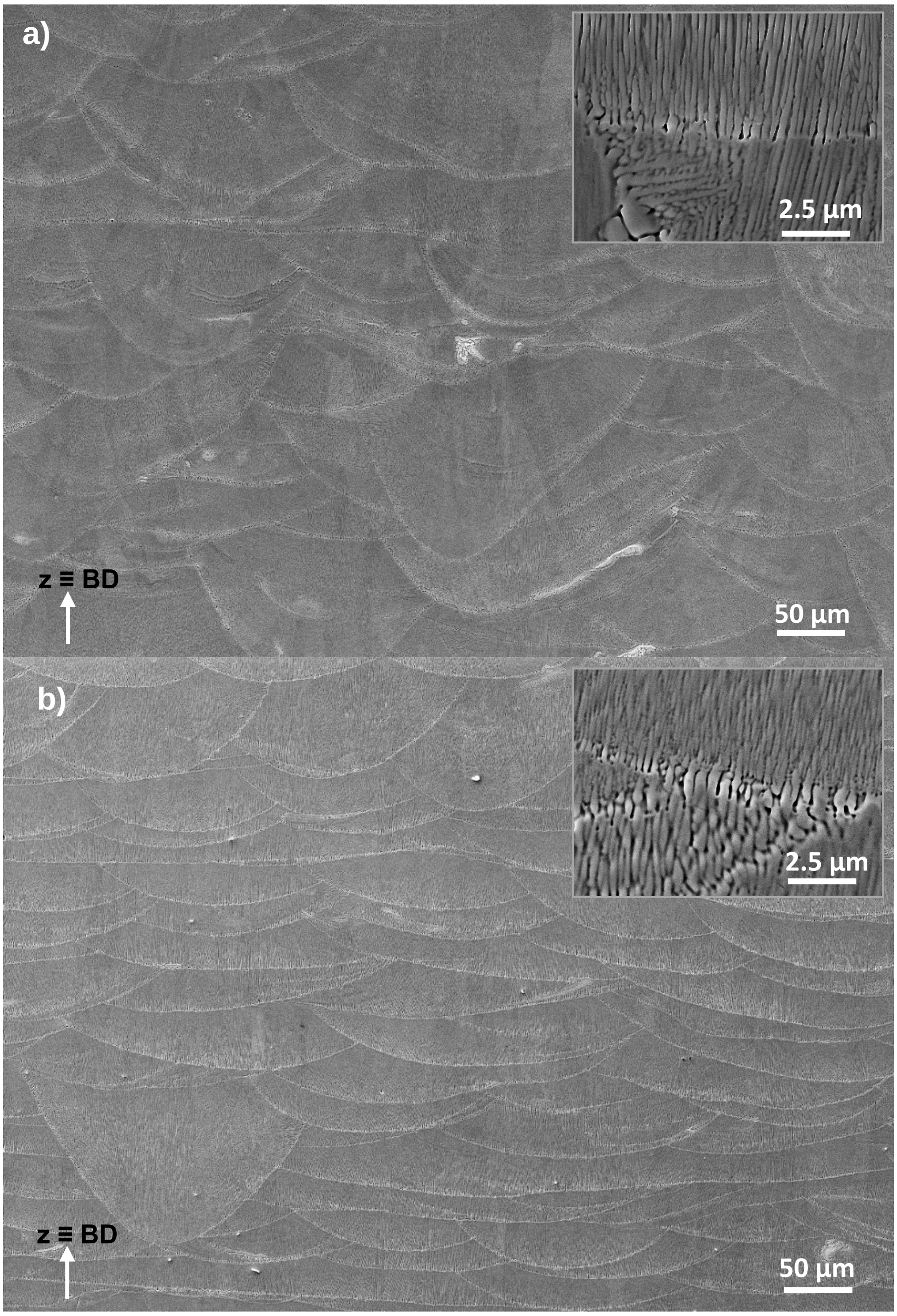

Figure 4.28. (a) Microstructure of the *TNZT-SLM-vertical* and (b) samples produced by SLM with a remelting step (*TNZT-remelting*). The insets shown the solidification structure with higher magnification.

The microstructure of the *TNZT-remelting* samples was investigated by EBSD experiments in the y-z building plane (Figure 4.29), and the grain size, morphology, orientation and crystallographic texture is obtained. A β-Ti single phase structure was indexed in the EBSD experiment, which means that phase transformation related to the remelting step is not detected.

The inverse-pole figures (IPF) show columnar grains growing epitaxially through several layers, oriented in the building direction (Figure 4.29a-c) and a strong predominance of grains colored with red in the IPF-x image is seen (Figure 4.29a), which means a strong grain alignment effect. In fact, the pole figure in the {100}, {110} and {111} stereographic planes confirm the crystallographic texture (Figure 5.29d). On this case, a similar feature to *TNZT-SLM-vertical* sample is seen, but with stronger texture, as result of the layer remelting procedure.

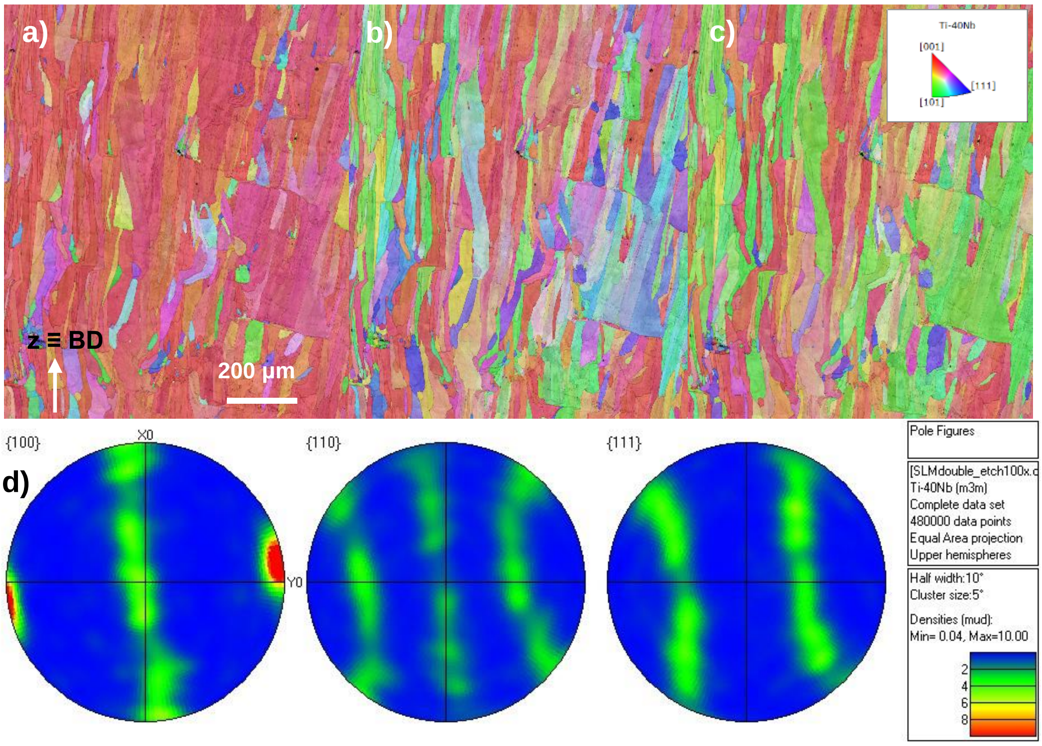

Figure 4.29. EBSD maps of a sample of samples submitted to laser remelting scanning strategy: Inverse-pole figure (IPF) in the x- (a), y- (b) and z- (c) axis, and pole figure in the {100}, {110} and {111} stereographic planes (d). The inset is the IPF orientation reference.

In addition, crystallographic grain size was determined from the EBSD experiments: The mean transversal linear intercept length of the *TNZT-*

remelting sample was $\bar{l}_l$ = 220 µm. It is seen that, even with a higher energy input applied by adding a remelting step, the columnar grains are smaller than in the *TNZT-SLM-vertical* sample ($\bar{l}_l$ = 327 µm) with a single melting routine. This is related to the processing conditions on each case, with deeper melt pool produced when a layer of powder is melted in contrast to a layer of solid material in the remelting condition. In addition, a bimodal grain structure, with fine-grained region between columnar grains, is no longer observed after laser remelting, which is related to a uniform melting subsequent tracks, instead of remelting solid tracks (overlapping) when first melting the powder layer. Therefore, it is seen that the laser-material interaction had a decisive influence in the melt pool and, therefore, in the grain size of samples of the TNZT alloy produced by SLM, when comparing single melting and laser remelting scanning strategies.

4.2.5 Homogenization heat treatment of SLM samples

In order to homogenize the microstructure of the as-built selective laser melted samples of the Ti-35Nb-7Zr-5Ta (wt%) alloy, a homogenization heat treatment was applied at 1000 °C for 24 h under Ar atmosphere, followed by water quenching (*TNZT-SLM-HT*). The crystal structure identified in the XRD pattern of the homogenized samples is β single phase (Figure 4.30) and, therefore, the heat-treatment and following fast cooling did not change the phase constitution of the samples produced by selective laser melting.

The microstructure observed by scanning electron microscope with a back-scattered electrons (BSE) detector shows a homogeneous chemical distribution (Figure 4.31). Therefore, it is seen that the Ta-enriched regions are no longer present, since a solute redistribution was obtained in the heat-treatment.

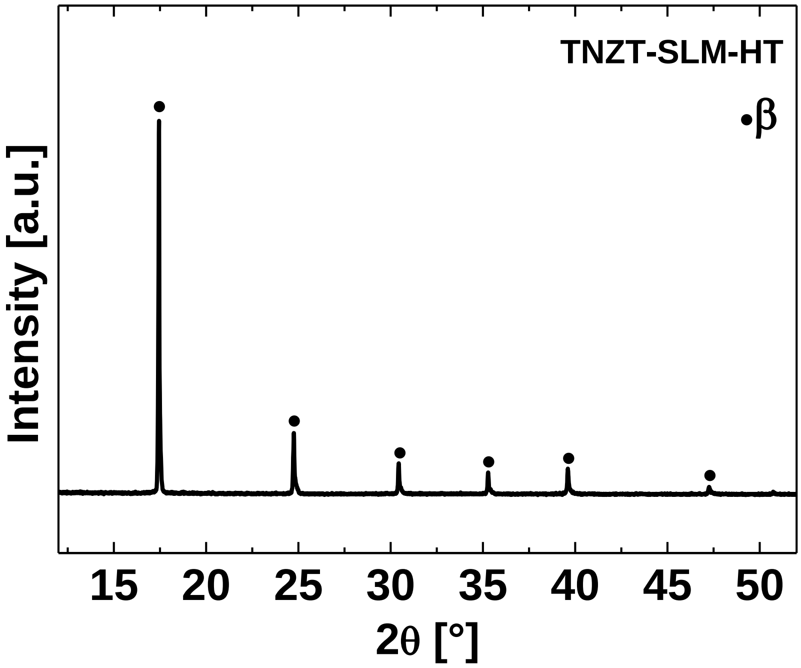

Figure 4.30. Diffractogram of the selective laser melted sample submitted to a homogenization heat-treatment at 1000 °C for 24 h, followed by water quenching (*TNZT-SLM-HT*).

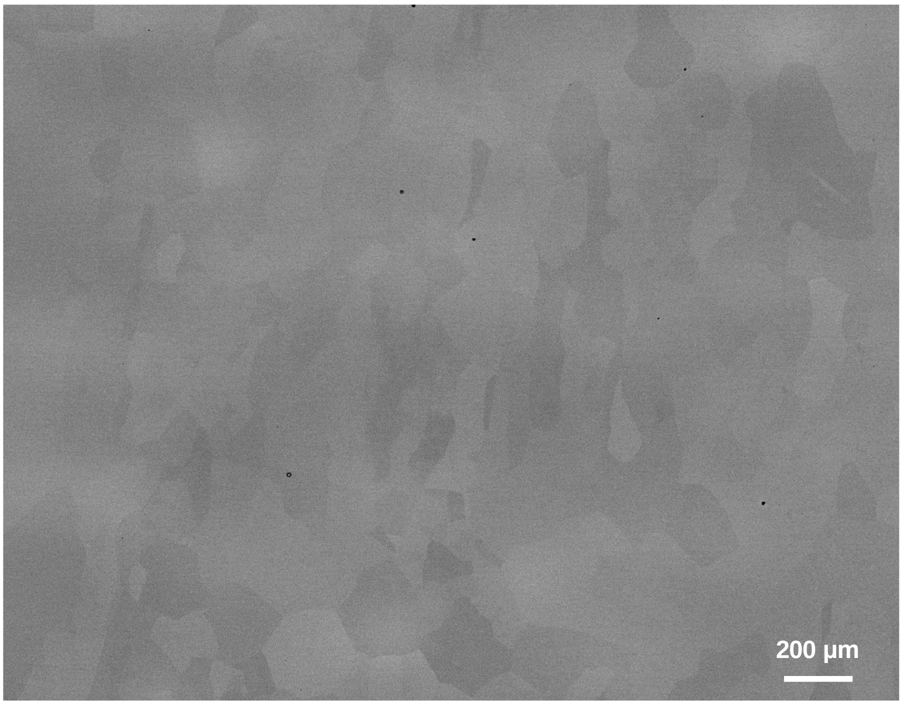

Figure 4.31. Micrograph of the selective laser melted sample submitted to a homogenization heat-treatment at 1000 °C for 24 h, followed by water quenching (*TNZT-SLM-HT*).

The homogenization heat treatment applied in the SLM sample resulted in an equiaxed grain structure, eliminating the columnar morphology seen in the as-built SLM samples. Nonetheless, a heterogeneous grain structure is observed with coarse and fine grains (Figure 4.31 and 4.32). The grain size was determined by the comparison procedure following the ASTM E112-12 Standard. An ASTM grain size number, G = 3, was obtained, which means an average grain diameter of approximately 125 µm, with a different grain morphology compared to *TNZT-SLM-vertical* condition. In addition, the grain size in the selective laser melted samples submitted to homogenization heat-treatment is smaller than the observed in the suction-casted samples heat-treated in the same conditions (G = 1; 250 µm). Therefore, the initial solidification microstructure presented a direct influence on the grain growth mechanism during the heat treatment. The crystal orientation in the *TNZT-SLM-HT* samples was also analyzed by EBSD. The IPF maps (Figure 5.32a-c) show absence of preferential orientation and, therefore, crystallographic texture is no longer observed after homogenization heat treatment of the selective laser melted samples, offering an important alternative to eliminate the microstructural anisotropy in the SLM samples.

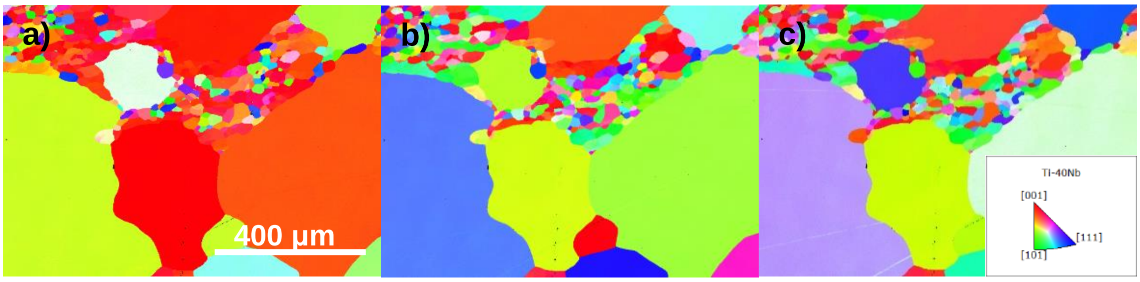

Figure 4.32. Electron back-scattered diffraction maps of the *TNZT-SLM-HT* sample: Inverse-pole figure (IPF) in the x- (a), y- (b) and z- (c) axis. The inset is the IPF orientation reference.

4.2.6 Mechanical properties of bulk samples of the TNZT alloy manufactured by selective laser melting

Compression test was performed in selective laser melted samples of Ti-35Nb-7Zr-5Ta with three parameters set and energy input values: v_s = 0.33 m/s, overlapping = 75%, E_v = 168.5 J/mm^3 (*TNZT-SLM-HE*); v_s = 0.57 m/s; overlapping = 50%; E_v = 58.3 J/mm^3 (*TNZT-SLM-vertical*), and v_s = 2.67 m/s; overlapping = 50%; E_v = 25.7 J/mm^3 (*TNZT-SLM-LE*), which corresponds to three different bulk densities. The truss stress-true strain curves are presented in Figure 4.33.

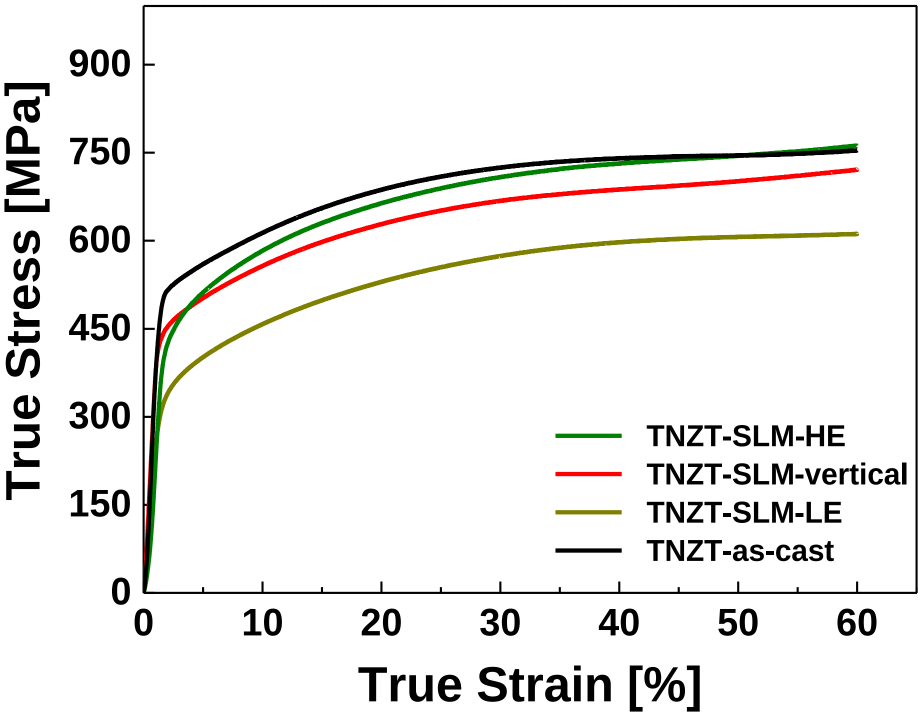

Figure 4.33. True stress-true strain curves from compression tests of specimens produced by selective laser melting. *HE* and *LE* means high energy and low energy, respectively.

The Young's modulus, E, yield strength (stress at 0.2% strain offset), σ_{YS}, and compressive stress at 35% strain, $\sigma_{35\%}$, were obtained and results from the *TNZT-as-cast* condition and reported in literature are also presented for comparison (Table 4.4).

The first important result is the effect of porosity on compression strength of the selective laser melted samples. It is well known that density is a crucial factor for strength in SLM bulk samples, and higher porosity means lower mechanical strength [7, 11, 38, 39]. Still, there was no premature failure even in samples with high porosity and a compressive deformability above 60% was observed, and therefore, the samples present high ductility under compressive stress, similarly to the results reported by Schwab et al. [82] and Zhang et al. [121]. Another important impact of porosity is seen in the Young's modulus (E) of the selective laser melted samples (Figure 4.34), where samples produced with highest scanning speed of 2.67 m/s, resulting in 7% of porosity, presented a Young's modulus, E = (25 ± 4) GPa.

Table 4.4. Compression properties of bulk samples of the TNZT alloy produced by SLM. σ_{YS} is the yield strength; $\sigma_{35\%}$ is the compressive stress at 35% strain; E is the Young's modulus; $\bar{l}_t$ is the transverse intercept length; $\bar{l}_l$ is the longitudinal intercept length; ε_{se} is the recoverable strain (pseudoelasticity).

Sample	**σ_{YS} (MPa)**	**$\sigma_{\varepsilon=35\%}$ (MPa)**	**E (GPa)**	**ε_{se} (%)**	**$\bar{l}_l$ / $\bar{l}_t$ (μm)**	**Relative density (%)**
TNZT-as-cast (reference)	469 ± 42	686 ± 76	48 ± 4	1.5	30 / 30	100.0
TNZT-SLM-HE	389 ± 26	702 ± 54	32 ± 1	-	-	97.8 ± 0.2
TNZT-SLM-vertical	430 ± 38	682 ± 05	45 ± 5	0.5	327 / 72	99.0 ± 0.4
TNZT-SLM-LE	293 ± 20	589 ± 03	25 ± 4	-	-	93.0 ± 0.3
Ti-45Nb [82]	≈ 380	≈ 723	-	-	-	97.7 ± 1.3
Ti-30Nb-5Ta-7Zr-0.1O [121]	664	-	59.5	-	-	99.2
Ti-34Nb-5Zr-11Sn [136]*	563 ± 38	-	53 ± 1	-	-	99.0

*Tensile test.

The Young's modulus of the SLM samples are shown in Figure 4.34. It is noticed that highest density (*TNZT-SLM-vertical*) samples presenting a Young's modulus of (45 ± 5) GPa, close to the as-cast condition. Nonetheless, the Young's modulus values obtained must be taken carefully and a more precise technique such as nanoindentation should be performed to confirm. Zhang et al. (2018), processed TNTZ lattice structure samples with porosity of 77.23% and Young's modulus of ~19.0 GPa by selective laser melting [121]. Therefore, the results in the present work disclosure an important alternative to tune the mechanical biocompatibility in terms of stiffness of samples of the Ti-35Nb-7Zr-5Ta (wt%) alloy, since a wide range of Young's modulus is obtained.

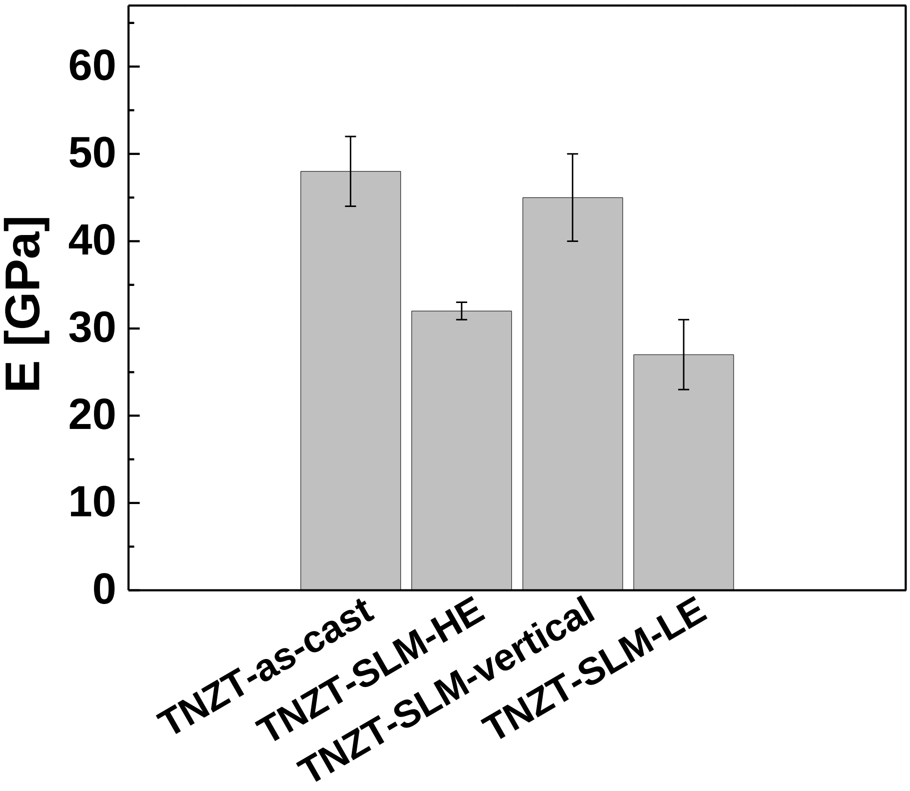

Figure 4.34. Young's modulus (E) of bulk samples of the Ti-35Nb-7Zr-5Ta (wt%) alloy produced by SLM.

The *TNZT-SLM-vertical* sample, which shown highest density, presented slightly lower mechanical strength (σ_{YS} = 430 MPa and $\sigma_{35\%}$ = 682 MPa) than the Cu-mould suction-cast samples (σ_{YS} = 469 MPa and $\sigma_{35\%}$ = 686 MPa).

Strain hardening is observed for either cases and no distinct yield point is seen. This is mainly related to the distinct solidification structure, grain size, morphology and orientation resulted from the two manufacturing processes. In fact, a equiaxed dendritic solidification structure is observed in the *TNZT-as-cast* sample with randomly oriented equiaxed grains ($\bar{l}_l$ / $\bar{l}_t$ = 120/120), and a fine columnar dendritic solidification structure is seen in the *TNZT-SLM-vertical* samples, with columnar grains ($\bar{l}_l$ / $\bar{l}_t$ = 327/72) preferably oriented in the building direction. In addition, a low volume fraction of α” was formed in the as-cast samples, which results in a strengthening effect of the β matrix, while a β single phase structure was observed in the SLM samples. Plus, since the solid dissolved in the matrix is enhanced in selective laser melting, the microsegregatioin observed in the Cu-mould suction-casted is no longer seen in the selective lase melted samples.

Zhang et al. (2018) reported mechanical properties of a Ti-30Nb-5Ta-7Zr-0.11O (wt%) biocompatilble alloy, in samples processed by SLM with 99.2% of relative density [121]. The authors report a Young’s modulus of 59.5 GPa and yield strength of 664 MPa, which are higher than the obtained in the *TNZT-SLM-vertical* samples of the present work. The authors show that the as-printed part consisted of a majority β phase and a minority of fine α” martensitic laths (average length 0.8 μm), which is related to the lower Nb content, a powerful β stabilizer element [121]. It is known that α” martensitic laths increase the mechanical properties of Ti-Nb-based alloys [27, 84, 85], which explains the higher yield strength reported by the authors.

In another work, Zhang et al. (2011) processed a Ti–34Nb–5Zr–11Sn (wt%) biocompatible alloy by SLM, with oxygen content measured by carrier gas hot extraction of 2100 ppm [136]. The authors report that the samples tested under tensile loading applied on the build direction presented a Young’s modulus of ≈ 53 GPa, an ultimate tensile strength of ≈ 660 MPa and a ductility exceeding 10%. The authors states that the building direction is the weakest direction for samples produced by SLM. This could explain the lower yield strength observed in the Ti-35Nb-7Zr-5Ta (wt%) alloy compared to as-cast samples, although the compression properties were comparable to a Ti–35Nb–

5Zr–5Ta alloy (wt%) (σ_{YS} = 400 MPa), a similar composition processed by conventional methods [31].

The pseudoelasticity of the TNZT alloy produced by selective laser melting with relative density of 99.0% (*TNZT-SLM-vertical*) was obtained in cyclic compression tests (Figure 4.35). The recoverable strain was limited to the first step of strain, ε_{se} = 0.5%, lower than in the as-cast samples (ε_{se} = 1.5%). This result is related to the β phase stability, since solute concentration in the matrix is enhanced in selective laser melting and the microsegregatioin observed in the Cu-mould suction-cast is no longer seen. Another aspect is the lower yield strength of the selective laser melted samples compared to the as-cast samples, since permanent plastic deformation competes with the stress-induced phase transformation mechanism [25-28, 88, 107].

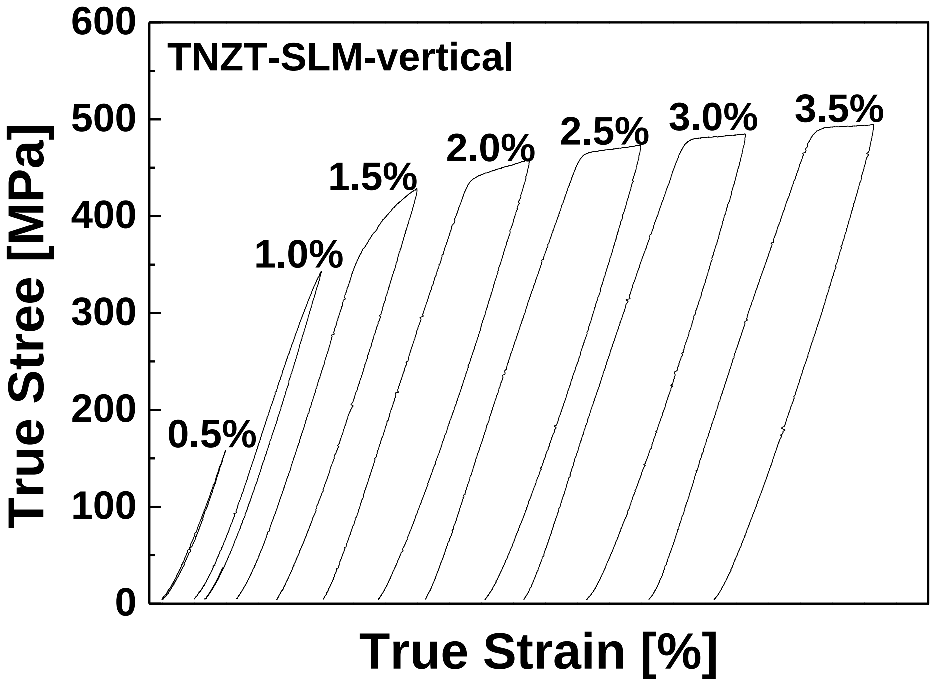

Figure 4.35. True stress-true strain curves obtained in cyclic compression tests of specimens produced by SLM.

A similar result is reported for a Ti–34Nb–5Zr–11Sn (wt%) samples processed by SLM [136]. According to the authors, the absence of pseudoelasticity was caused by a high oxygen content (2100 ppm), enhancing the β phase stability and preventing the phase transformation, which is not necessarily the case here, since the oxygen of the SLM samples were practically the same as the as-cast sample. However, this feature, combined with higher cooling rates in SLM and, thus, enhanced β phase stability at room temperature in the *TNZT-SLM-vertical* samples, contributed for the lower pseudoelasticity in the as-built samples.

Although the TNZT alloy presented good processability by SLM, it was seen that the microstructure of the *TNZT-SLM-vertical* samples is formed by columnar grains aligned in the building direction, and different grain structure and crystallographic textures develops depending on sample orientation. For the *TNZT-0°horizontal* sample a fine grain structure randomly oriented was observed, and in the *TNZT-45°degree*, columnar grains are seen following the part orientation. Furthermore, samples with laser remelting scanning strategy also shown effect on the microstructure (*TNZT-remelting*). On this case, although the columnar-dendritic morphology is maintained, a finer structure and stronger crystallographic texture is observed, when compared to the *TNZT-SLM-vertical* samples. Finally, a homogenization heat treatment was applied on the as-built selective laser melted samples (*TNZT-SLM-HT*). The grain size, morphology, orientation and crystallographic texture analysis showed equiaxial grains absent of preferential orientation and, therefore, crystallographic texture is no longer observed after homogenization heat treatment of the selective laser melted samples.

In order to investigate those effects on the mechanical properties of the Ti-35Nb-7Zr-5Ta (wt%) alloy processed by selective laser melting, compression test was performed, and true stress-true strain curves are shown in Figure 4.36 and the properties are summarized on Table 4.5.

Table 4.5. Compression properties of bulk samples produced by SLM in different orientations, with laser remelting strategy and submitted to heat treatment.

Sample	**σ_{YS} (MPa)**	**$\sigma_{\varepsilon=35\%}$ (MPa)**	**E (GPa)**	**ε_{se} (%)**	**$\bar{l}_l$ / $\bar{l}_t$ (μm)**	**Relative density (%)**
TNZT-SLM-vertical (reference)	430 ± 38	682 ± 05	45 ± 5	0.5	327 / 72	99.0 ± 0.4
TNZT-0°horizontal	442 ± 16	696 ± 02	50 ± 7	0.5	115 / 91	98.7 ± 0.6
TNZT-45°degree	476 ± 10	734 ± 12	54 ± 4	0.5	129 / 89	99.0 ± 0.4
TNZT-remelting	455 ± 40	721 ± 14	43 ± 5	0.5	220 / 99	99.4 ± 0.5
TNZT-SLM-HT	471 ± 09	820 ± 07	44 ± 2	0.5	125*	-

*ASTM grain size number, G = 3, which means an average grain diameter of approximately 125 μm.

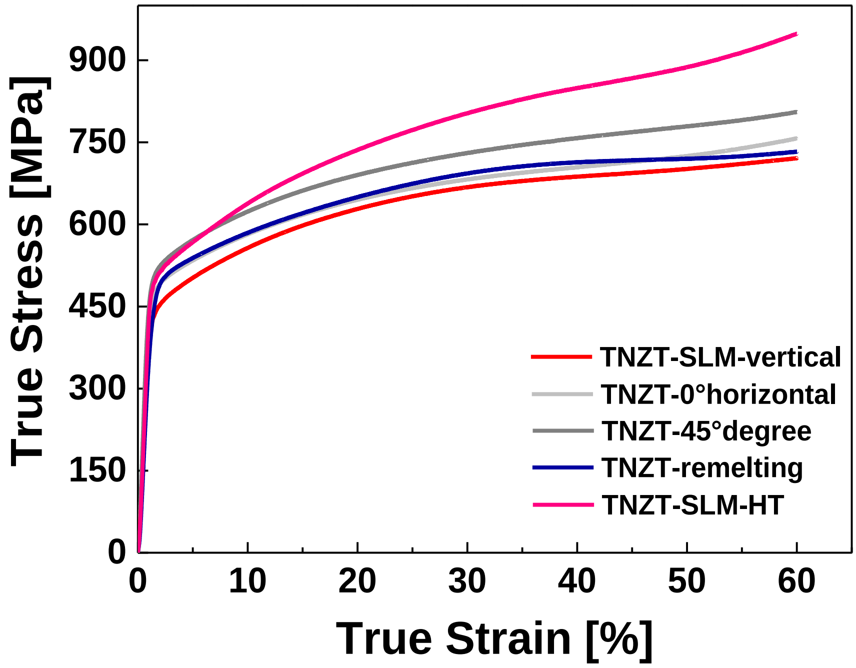

Figure 4.36. True stress-true strain curves from compression tests specimens produced by selective laser melting in different orientations, laser remelting strategy and submitted to heat treatment.

Strain hardening is observed, and no distinct yield point is seen in the investigated conditions. It may be seen that the specimens built in different orientations, with laser remelting and heat-treated presented higher compressive stress than in the as-built *TNZT-SLM-vertical* condition. A first important aspect is the grain size: in all cases the grains are finer than in the *TNZT-SLM-vertical* conditions, which contributes to higher mechanical strength of the samples. Another important fact is that the samples oriented at 0° (horizontal) and 45° were produced together, but in a different batch than the vertical samples, reusing the *TNZT-powder* for the 5th time. The chemical analysis indicated an oxygen content of 270 ppm in the powder used for producing the *TNZT-0°horizontal* and *TNZT-45°degree* samples. In the case of the *TNZT-SLM-remelting*, it is seen a slight densification improvement, which is known as the main advantage of laser remelting strategy and explains the higher compressive stress than the *TNZT-SLM-vertical* samples with single melting routine [103, 134, 135]. The specimens submitted to homogenization heat treatment shown a higher strain hardening effect, although a discontinuous yield point is not seen this time, in contrast of the Cu-mould suction-cast samples heat-treated in same conditions. However, even with the samples being encapsulated in argon and the heat treatment furnace atmosphere being kept with pure argon (99.99% of purity), an oxygen uptake might have happened, which combined to the equiaxed grain structure, resulted in higher mechanical strength than the as-built SLM samples.

It was expected that, the *TNZT-0°horizontal* specimens with equiaxial grain structure ($\bar{l}_l$ / $\bar{l}_t$ = 115 / 91) and the *TNZT-45°degree* specimens with columnar grains ($\bar{l}_l$ / $\bar{l}_t$ = 129 / 89) oriented in 45° (easy dislocation slip direction), would present the highest and lowest compressive stress, respectively. In fact, Dadbakhsh et al. (2016) produced samples of a NiTi alloy oriented horizontal (0°), at an angle (45)°, and vertical (90°) on the SLM baseplate, and reported that the resistance of the material against the compressive force was highest in the horizontal direction and lowest in the vertical direction, since the vertical samples developed a strong <100> texture formed along the building direction [77]. According to the authors, the [100] orientation is characterized as “soft” direction under compression (the loading direction in the compression tests).

As another example, Edwards et al. (2015) showed that the fracture toughness of Ti-6Al-4V (wt%) samples produced by SLM was higher when the cracks propagated perpendicularly to the building direction (horizontal) than in the case of vertical samples, where the crack is in the same plane as the build layers [137]. Nonetheless, the samples oriented at 0°horizontal presented higher porosity (≈ 2%) than the samples produced at 45°degree (≈ 1%), as may be seen in Figure 4.37. A clear lack of fusion type of porosity was observed in the *TNZT-0°horizontal* samples, as a result of the scanning strategy (stripes of 3.0 x 3.0 mm², with a 50% of overlap between each island), and it was the dominant aspect explaining the lower mechanical strength of this condition compared to the *TNZT-45°degree*.

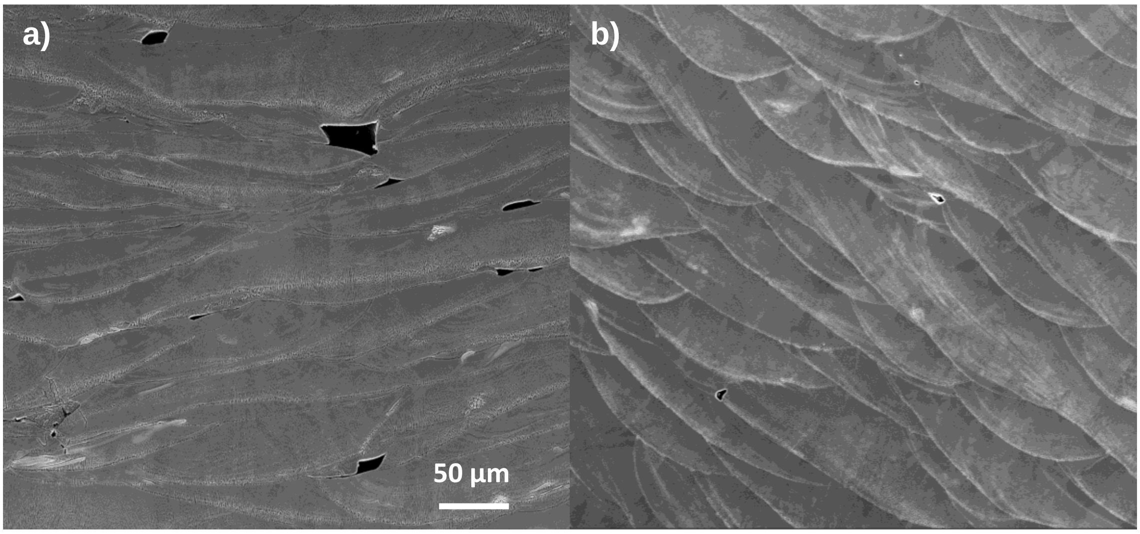

Figure 4.37. Microstructure of samples produced by SLM with different orientation: *TNZT-0°horizontal* (a) and *TNZT-45°degree* (b).

Another important effect of sample orientation and laser remelting scanning strategy is seen on the Young’s modulus (E) of the selective laser melted samples, (Figure 4.38). The Young's modulus is known to present a crystallographic orientation dependency, even in highly symmetrical crystal structure such as body-centered cubic structure. In fact, a strong orientation dependence of the Young's modulus has been demonstrated for a Ti–15Mo–5Zr–3Al (wt%) alloy, with the highest value (~120 GPa) along the <111> orientation and the lowest value (44.4 GPa) along the <001> orientation, in case of single crystals [138], and (68.7 ± 0.9) GPa and (99.6 ± 4.8 GPa) for samples manufactured by SLM in vertical and horizontal orientations, respectively [126].

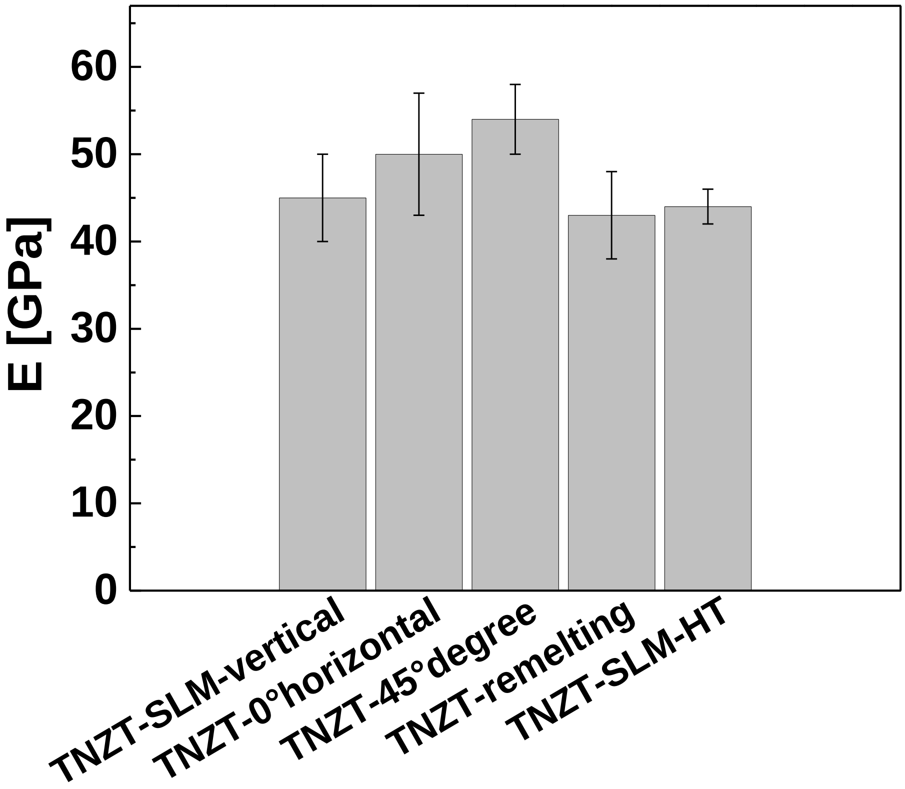

Figure 4.38. Young’s modulus of bulk samples of the TNZT alloy produced by SLM in different orientations, laser remelting strategy and submitted to heat treatment.

The Young’s modulus of the *TNZT-45°degree* was the highest (E = 54 GPa) between the investigated conditions, followed by the *TNZT-0°horizontal* (E = 50 GPa). The other conditions show Young’s modulus close to the *TNZT-SLM-vertical* samples (E = 45 GPa), and therefore, not significant changing occurred related to laser remelting (E = 43 GPa) and homogenization heat treatment (E = 44 GPa), as may be seen in Figure 4.38. Therefore, it is seen that sample orientation and the crystallographic texture formed in selective laser melting of samples of the TNZT alloy has an important effect on the Young's modulus of the samples.

The pseudoelasticity of the TNZT alloy produced by SLM with different sample orientation, adding a layer remelting step in the scanning strategy and applying a homogenization heat treatment was obtained in cyclic compression tests (Figure 4.39). The recoverable strain was limited to the first step of strain for all conditions, ε_{se} = 0.5%. This result is related to the β phase stability, and a stress-induced martensitic transformation does not occur in the as-built and heat-treated samples, which is the mechanism behind the pseudoelastic effect.

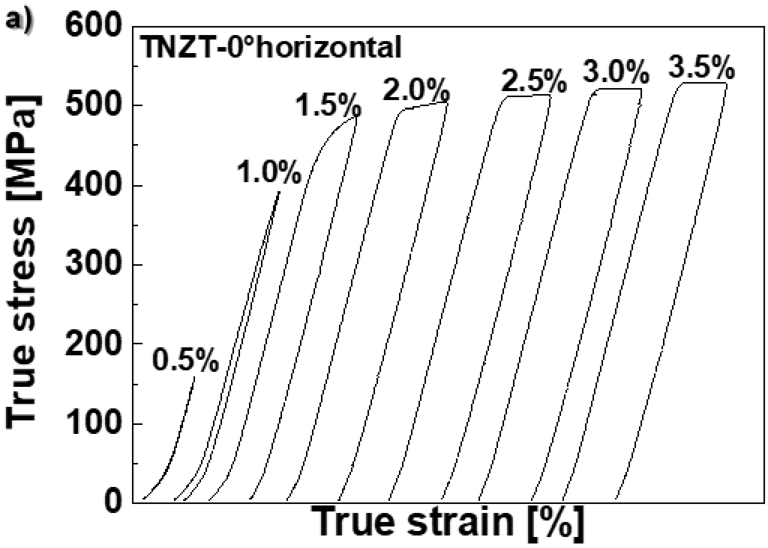

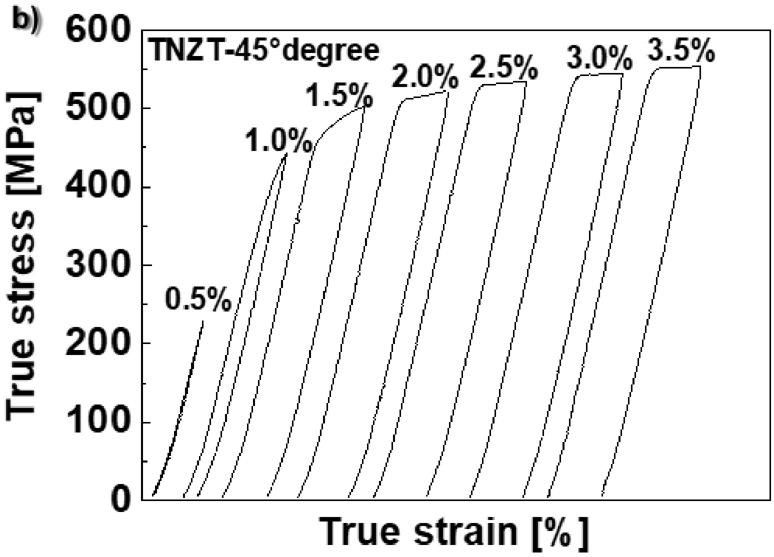

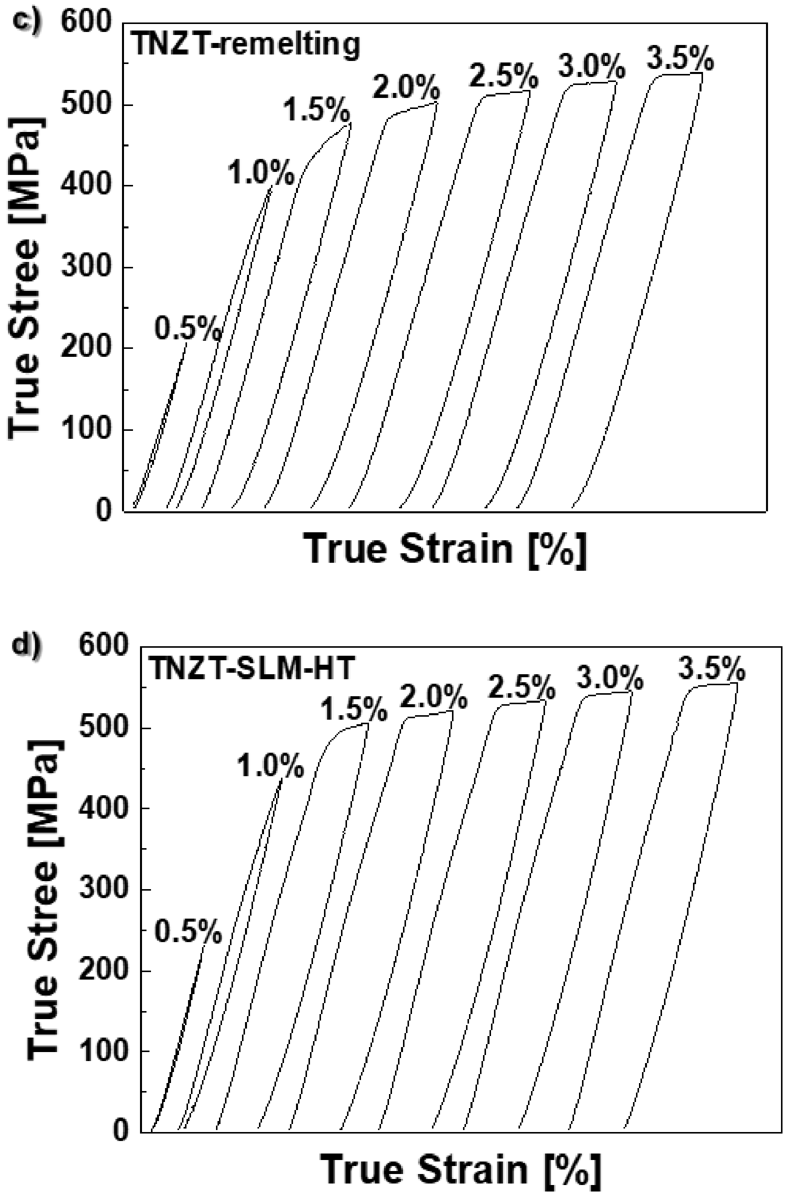

Figure 4.39. True stress-true strain curves obtained in cyclic compression tests of samples produced by selective laser melting, in horizontal (a) and 45° (b) orientations, with a laser remelting strategy (c) and submitted to heat treatment (d).

Therefore, it is seen that the highest recoverable strain is observed in the Cu-mould suction-casted samples, in the as-cast condition, with a fine equiaxed grain structure. In fact, it was seen that the solidification microstructure of the as-cast sample presented microsegregation, with Ti depletion from the matrix, which results on a Ti-β matrix with some martensitic laths, enhancing the possibility to occur a stress-induced martensitic transformation. In addition, the refined grain structure of the as-cast samples resulted in higher mechanical strength than the as-built SLM samples, which also contributed to a higher pseudoelasticity in those samples. Another possibility would be to test the samples under tensile loading, as it has been reported that samples of NiTi manufacture by SLM, presented opposite mechanical response compared to compressive loading, related to the <100> preferential orientation of grains, acting differently under tension as a ‘hard’ direction [77].

4.2.7 Selective laser melting of prototypes

It is known that additive manufacturing is very suitable to applications where complex geometry, low volume and strong individualization are required [139, 140]. Therefore, some prototypes were produced in order to attest the feasibility of processing the Ti-35Nb-7Zr-5Ta (wt%) alloy in near-net-shape parts with more complex geometry by selective laser melting. A dental mini implant with threads (Figure 4.40a) and a stent (Figure 4.40b) were manufactured with the optimized parameters set (layer thickness of 40 µm, laser power of 129 W and scanning speed of 0.57 m/s). For the mini implant, an overlapping of 50% was applied and the prototype was built as a bulk sample with unidirectional scanning strategy with 79° rotation between layers. In the case of the stent, hatching distance was not defined due to its open geometry and struts dimension corresponding to a single track, but a remelting step was applied in order to improve the surface finishing of the stent with same parameters used in the first melting.

In order to evaluate the quality of the prototypes, µ-XCT was performed and the reconstructed 3D images are shown in Figure 4.40. The mini implant presents a rough surface, with a relative density of 99.3%, and details of the threads are not clearly distinguished. This means that the process resolution was not enough to process the part geometry with details, which may be tuned by reducing the size of the laser beam spot size, the powder size distribution, and the layer thickness [141]. For the stent, some struts are melted together, resulting in a closed structure. On this case, the SLM parameters set should be further optimized to produce thin-walled samples. Therefore, although specific parameters optimization is necessary to improve the surface quality and tune the process resolution of the prototypes, the parts could be successfully produced by selective laser melting, showing that it is possible to obtain final near-net-shape parts of the TNZT alloy by an additive manufacturing technology.

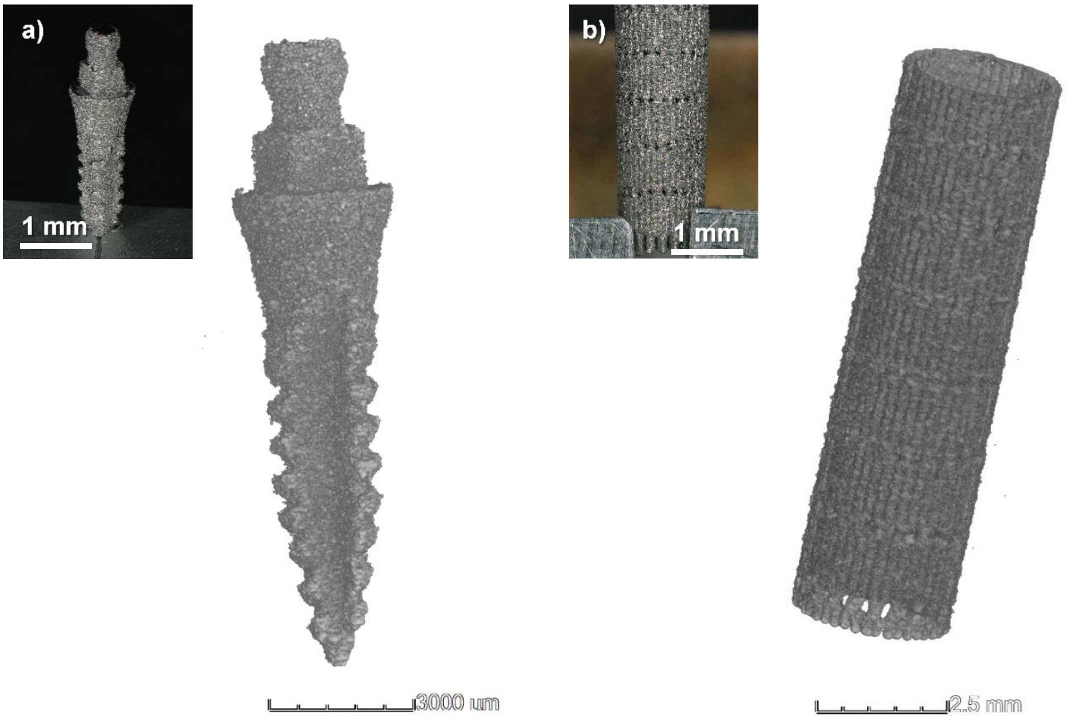

Figure 4.40. Prototypes of the Ti-35Nb-7Zr-5Ta (wt%) alloy produced by SLM: (a) dental mini implant; (b) stent.

4.3 Oligocrystalline Structure Formation

One of the drawbacks of Ti-Nb-based alloys is the low recoverable strain when compared to the Ni-Ti system, which limits the applicability of Ti-Nb alloys in biomedical parts when pseudolelasticy is required [85]. An alternative, proposed to improve pseudoelasticity of Cu-based, Fe-based and Ni-based shape-memory alloys, is to induce an oligocrystalline structure formation (oligo – few; crystalline – crystals), also known as bamboo structure [32-35, 90-96, 99, 100].

On this work, an innovative approach is proposed to obtain a bamboo-like structure formation in a β-Ti-35Nb-7Zr-5Ta alloy in thin-walled samples produced by selective laser melting, an additive manufacturing technology. The thin-walled samples (hollow tubes with 3 mm of external diameter, wall thickness of 200 µm and 12 mm height) are presented in (Figure 4.41). The samples were produced by SLM with the following parameters: laser power of 129 W, scanning speed of 0.57 m/s, with a layer thickness of 40 µm. Hatching distance was not defined and the wall thickness corresponded to a single track (*TNZT-single-tube*). The samples were heat-treated by a simple isothermal heat treatment (1000 °C for 24 h, followed by water quenching) in order to investigate grain growth mechanism and the formation of the bamboo (oligocrystalline) structure (*TNZT-tube-HT*).

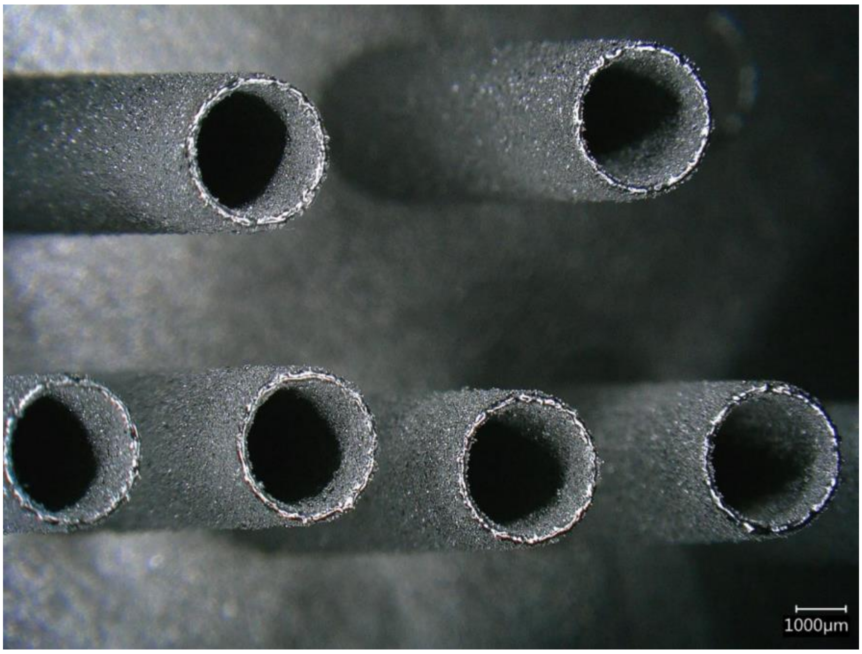

Figure 4.41. Thin-walled tubes of the TNZT alloy manufactured by selective laser melting.

The tubes exhibit considerable roughness, estimated using the arithmetical mean deviation of the assessed profile method as (14 ± 10) µm. Figure 5.42 shows the microstructure of the thin-walled tubes before and after heat treatment. Before treatment (Figure 4.42a), the tubes exhibit a bimodal polycrystalline structure with elongated columnar grains around the wall center with (12 ± 3) µm of width and (240 ± 90) µm of length, and small near-equiaxed grains at the surface with (9 ± 3) µm diameter. The elongated columnar grains span several layers of deposited material and are oriented in the build direction, similar as observed for the bulk samples (Figure 4.25). Considering that the laser beam presents a Gaussian energy distribution, the energy decreases moving away from the beam center. It will decrease up to be not enough to melt the material but enough to sinter the powder at the outer region. The near-equiaxed grains are formed from the sintered powder at this region. It is confirmed by the large amount of porosity found in this region (Figure 4.42a).

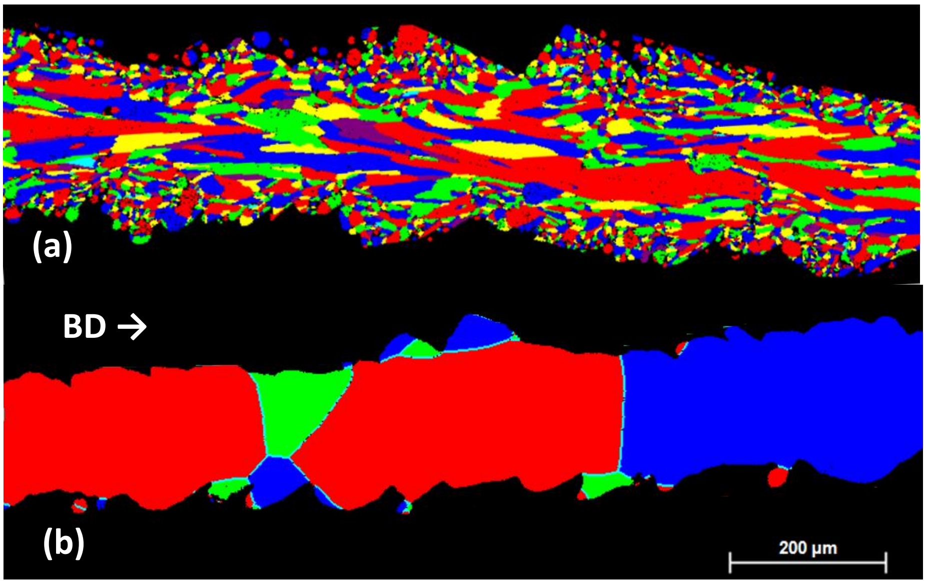

Figure 4.42. (a) Electron back-scattered diffraction maps of the thin-walled tubes vertical cross section before (*TNZT-single-tube*) and (b) after heat treatment (*TNZT-tube-HT*). BD is the building direction.

A β-Ti bimodal microstructure (columnar/center and near-equiaxed/surface) is observed in the as-prepared tubes and an oligocrystalline structure was formed in the heat-treated tubes.

During annealing an oligocrystalline microstructure forms and the grains have a length of around (350 ± 50) µm (Figure 4.42b). This is a result of the initial bimodal structure and surface effects: The large columnar grains grow excessively during the thermal treatment on the expense of the smaller grains. The driving force is the reduction of the grain boundary energy and, hence, some grains grow until they cover the entire thickness of the wall. On the contrary, if only grains with similar size are present, these grains will grow with the same rate and it will form a conventional polycrystalline structure with several triple junctions.

Therefore, the bimodal structure observed is essential for the formation of the oligocrystalline structure. The oligocrystalline grains tend to minimize their surface energy by adapting to a specific orientation [142]. This favors the formation of large grains with lower surface energy and contributes for the oligocrystalline structure formation. Similar oligocrystalline microstructures are expected for other systems with a comparable bimodal microstructure after selective laser melting. The observed columnar microstructure (Figure 5.42a) is very common in SLM because of the high thermal history inherent in this process [7] and it was observed already in several Al-, Fe- and Ti-based alloys [7, 36, 59, 75, 143].

The compression properties of *TNZT-single-tube* and *TNZT-tube-HT* samples were investigated, and cyclic compression curves are presented in Figure 5.43. The annealed sample reveals a higher strength than the as-prepared thin-walled tube even considering that the former exhibits larger grains, which should promote a lower strength as suggested by the Hall-Petch relation [144]. The reason might originate from the oxygen content in the samples. It was measured to be 1370 and 2700 ppm for the thin-walled tubes before and after annealing, respectively. Oxygen is known to increase the strength of titanium by solid solution hardening and explain the difference observed in strength [145].

Another important feature from Figure 4.43 is the recoverable strain. The annealed thin-walled tubes (*TNZT-tube-HT*) presents a larger recoverable strain than the as-prepared sample (*TNZT-single tube*). For example, if we compare the recoverable strain in the second strain cycle, it was measured 0.057 mm for the *TNZT-tube-HT* and 0.035 mm for *TNZT-single tube*, which corresponds to a recoverable strain 65% larger. This larger recoverable strain is explained by the larger strength and the oligocrystalline structure of the *TNZT-tube-HT* sample, which alloys a larger elastic and pseudoelastic strain, respectively. Another important aspect is related to the oxygen effect in phase stability of Ti-Nb-based alloys. As shown by Obbard et al. (2011) for a Ti-33Nb-5Zr-14Sn (wt%), the addition of oxygen reduces the recoverable strain because it raises the critical stress for α'' formation and reduces the volume fraction of α''. It also reduces the β→α'' transformation strains and shortens the stress plateau [144]. The authors also stated that this mechanism is not fully comprehended. Nonetheless, it proposed that this effect superimposed the beneficial effect of the oligocrystalline structure formation and decreased the pseudoelasticity of the alloy.

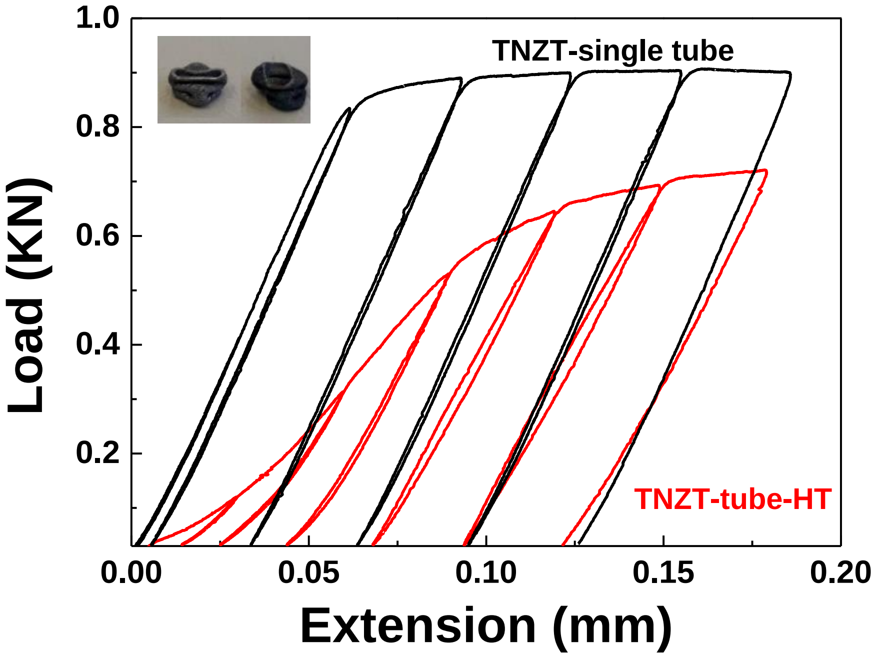

Figure 4.43. True stress-true strain curves obtained in cyclic compression tests of the Ti-35Nb-7Zr-5Ta thin-walled tubes (a) before (TNZT-single tube) and (b) after heat treatment (TNZT-single tube-HT). The inset shows samples after uniaxial compression up to 75% of strain (left: as-prepared tube; right: thermal-treated tube).

In order to attest the effect of the oligocrystalline structure on ductility, the samples were tested under uniaxial compression up to 4.5 mm of extension.

Both samples did not break, which confirms their high ductility. The inset of Figure 4.43 shows the samples after compression, where no cracks are observed. The high strength, large recoverable strain and high ductility observed for the oligocrystalline samples, combined with their biocompatibility, make these materials promising for biomedical applications as in scaffolds and stents.

5. CONCLUSIONS AND OUTLOOK

On this work, a novel manufacturing route for processing parts of a biocompatible alloy is proposed. Therefore, a biocompatible Ti-35Nb-7Zr-5Ta (wt%) alloy is processed by SLM.

Firstly, the TNZT powder is investigated and it is seen that the powder presents a β single phase structure. The morphology of the powder is mainly spherical, with, d_{50} = 32.5 µm and a narrow particle size distribution. A chemical inhomogeneity in the powder particles is noticed, with some particles richer in Ti-Ta and lower content or absent of Nb and Zr.

The laser parameters are optimized to process the TNZT powder by SLM. The maximum relative density of 99.0% is attained in the bulk samples when an energy input of 58.3 J/mm^3 is employed, which was defined as the best set of parameters to process the TNZT alloy by SLM. The melt pools are seen in the micrographs of the SLM samples and Ta-enriched regions are observed, as a result of not completely dissolved Ta-enriched powder particles in the matrix. A β-Ti single phase structure was identified by XRD and confirmed by TEM experiments.

The solidification microstructure of the as-built selective laser melted samples is distinct from the Cu-mould suction-cast sample, related to the different thermal history on both processes: A fine columnar-dendritic structure is formed in the SLM samples and an equiaxed dendritic structure was formed in the as-cast samples. The EBSD analysis of the as-built samples shown columnar grains growing epitaxially through several layers (length = 327 µm and width = 72 µm), with preferential direction of grain growth, opposed to randomly oriented grains observed in the Cu-mould suction-cast samples (average grain diameter = (120 ± 24) µm). The as-built SLM samples were submitted to a homogenization heat treatment and the grain size, morphology, orientation and crystallographic texture analysis showed equiaxial grains absent of preferential orientation and, therefore, crystallographic texture was no longer observed after homogenization heat treatment of the selective laser melted samples.

The effect of porosity on mechanical properties of the selective laser melted samples is clearly detected and Young’s modulus in the range of 25-48 GPa is obtained in bulk SLM samples with porosity varying between 1-7%. There was no premature failure even in samples with high porosity and a compressive strain above 60% was obtained. The SLM samples, which shown highest density, presented slightly lower compressive stress (σ_{YS} = 430 MPa and $\sigma_{35\%}$ = 682 MPa) than the Cu-mould suction-cast samples (σ_{YS} = 469 MPa and $\sigma_{35\%}$ = 686 MPa). Strain hardening is observed for either cases and no distinct yield point is seen. The pseudoelasticity of the TNZT alloy produced by SLM was measured in cyclic compression tests and recoverable strain, ε_{se} = 0.5% is obtained, lower than in the as-cast samples (ε_{se} = 1.5%).

Bulk samples were produced by SLM with different orientations. For the *TNZT-0°horizontal* sample a fine grain structure randomly oriented was observed (length = 115 µm and with = 91 µm), and in the *TNZT-45°degree*, columnar grains are seen following the part orientation. Although a higher compressive stress was expected in the horizontal samples, it was seen that lack of fusion type of porosity resulted in lower yield strength of the horizontal samples (442 MPa) than the 45° samples (476 MPa).

Prototypes of the TNZT alloy were produced by SLM. The mini implant presented a rough surface, with a relative density of 99.3%, and the stent had some struts melted together, resulting in a closed structure, showing that, even though specific parameters optimization is necessary to improve the surface quality of the prototypes, parts with complex geometry could be processed by SLM.

Finally, an attempt to maximize the pseudoelastic properties of the Ti-35Nb-7Zr-5Ta (wt%) alloy is performed and an innovative approach is proposed to obtain parts with complex geometries and oligocrystalline structure, combining an additive manufacturing technology and a simple heat treatment. It was seen that an initial bimodal polycrystalline structure with elongated columnar grains around the wall center and small near-equiaxed grains at the surface of thin-walled tubes produced by SLM, results in an oligocrystalline after annealing, reducing grain boundary energy and minimizing the materials free energy. This innovative processing route emerges as an interesting alternative for different types of alloys and permits to obtain oligocrystalline materials with complex shapes and geometries.

Although several aspects have been explored in the present thesis, it is recognized that the subject is not exhausted, and some future works are suggested.

Firstly, the mechanical properties of the samples were investigated by compression tests and it was seen that the samples shown high ductility under compression. Mechanical tests under tensile are important to determine the fracture strength and plastic deformation up to fracture in the TNZT alloy processed by SLM. Besides that, another method (e.g. nanoindentation) should be employed to measure the elastic properties of the TNZT alloy manufactured by SLM. In addition, abrasion resistance, fracture toughness, and fatigue resistance were not addressed here, but those are important properties on applications such as orthopedic implants and should be correlated to processing conditions in selective laser melting.

It was seen that the microstructure of the as-built SLM samples presented columnar grains, aligned in the building direction. It is known that such structure is not desirable in terms of mechanical properties, since it is associated to anisotropy. Nonetheless, it was seen that varying sample orientation modified the crystallographic texture of the samples. Therefore, an alternative approach would be to investigate the effect of varying scanning strategy on the microstructure of the samples, which could also be associated to a study of residual stress in selective laser melted parts. Besides that, the addition of second phase particles, such as TiB_2, could induce a more equiaxed grain structure, reducing the observed anisotropy.

The dislocation structure of SLMed samples may be investigated in more detail to understand its effect on mechanical properties of the samples, especially after heat treatment.

Finally, since the TNZT alloy is a biocompatible alloy, corrosion resistance and citotoxicity tests could be performed, correlating to different microstructures and part geometries possibly obtained by SLM.

6. REFERENCES

[1]. ISO/ASTM Standard 52900 – Standard Terminology for Additive Manufacturing – General Principles – Part 1: Terminology, ASTM, West Conshohocken, PA, 2015.

[2]. W. J. Sames, F. A. List, S. Pannala, R. R. Dehoff & S. S. Babu, The metallurgy and processing science of metal additive manufacturing, International Materials Reviews, 2016. http://dx.doi.org/10.1080/09506608.2015.1116649.

[3]. J.-P. Kruth, S. Dadbakhsh, B. Vrancken, K. Kempen, J. Vleugels, J. V. Humbeeck, Additive Manufacturing of Metals via Selective Laser Melting: Process Aspects and Material Developments. In: T. S. Srivatsan; T. S. Sudarschan, Additive Manufacturing: Innovations, Advances, and Applications, CRC Press Taylos & Francis Group, Florida, 2016. p. 448.

[4]. D. Gu, Laser Additive Manufacturing of High-Performance Materials. Berlim: Springer-Verlag Berlin Heidelberg, 2015. p. 322.

[5]. L. E. Murr, E. Martinez, K. N. Amato, S. M. Gaytan, J. Hernandez, D. A. Ramirez, P. W. Shindo, F. Medina, R. B. Wicker, Fabrication of Metal and Alloy Components by Additive Manufacturing: Examples of 3D Materials Science, Journal of Materials Research and Technology (2012).

[6]. F. H. Froes, B. Dutta, The Additive Manufacturing (AM) of Titanium Alloys. Advanced Materials Research, 1019, 2014, p. 19–25. https://doi.org/10.4028/www.scientific.net/AMR.1019.19.

[7]. D. Herzog, V. Seyda, E. Wycisk, C. Emmelmann. Additive manufacturing of metals. Acta Materialia, 117 (2016). http://dx.doi.org/10.1016/j.actamat.2016.07.019.

[8]. L. Thijs, F. Verhaeghe, T. Craeghs, J. V. Humbeeck, J. P. Kruth, A study of the microstructural evolution during selective laser melting of Ti-6Al-4V. Acta Materialia, 58(9), (2010), 3303–3312. https://doi.org/10.1016/j.actamat.2010.02.004.

[9]. S. A. M. Tofail, E. P. Koumoulos, A. Bandyopadhyay, S. Bose, L. O. Donoghue, C. Charitidis, Additive manufacturing: scientific and technological challenges, market uptake and opportunities. Materials Today, (2017). https://doi.org/10.1016/j.mattod.2017.07.001.

[10]. I. Gibson, D. Rosen, B. Stucker. Additive Manufacturing Technologies: 3D printing, Rapid Prototyping, and Direct Digital Manufacturing, second ed.,

Springer Science+Business Media, New York, 2015. https://doi.org/10.1007/978-1-4939-2113-3.

[11]. T. Debroy, H. L. Wei, J. S. Zuback, T. Mukherjee, J. W. Elmer, J. O. Milewski, A. M. Beese, A. Wilson-Heid, A. De, W. Zhang. Additive manufacturing of metallic components – Process, structure and properties. Progress in Materials Science, 92, (2018), p. 112–224. DOI 10.1016/j.pmatsci.2017.10.001.

[12]. S. L. Sing, J. An, W. Y. Yeong, F. E. Wiria, Laser and electron-beam powder-bed additive manufacturing of metallic implants: A review on processes, materials and designs. Journal of Orthopaedic Research, 34(3), (2016), 369–385. https://doi.org/10.1002/jor.23075.

[13]. B. Vandenbroucke, J. P. Kruth. Selective Laser Melting of biocompatible metals for rapid manufacturing of medical parts. Rapid Prototyping Journal, 13(4), 2007, p.196-203. https://doi.org/10.1108/13552540710776142.

[14]. A. A. Antonysamy, Microstructure, Texture and Mechanical Property Evolution During Additive Manufacturing of Ti6Al4V Alloy for Aerospace Applications. Doctoral Thesis, University of Manchester, 2012, p. 316.

[15]. Y. Zheng, X. Xu, Z. Xu, J. Wang, H. Cai. Metallic Biomaterials: New Directions and Technologies, first ed., Wiley-VCH Verlag GmbH & Co. KGaA. (2017).

[16]. M. Niinomi, Metals for biomedical devices, CRC Press Woodhead Publishing Limited, Cambridge, UK, 2010. p. 430. https://doi.org/10.1533/9781845699246.

[17]. M. A. -H. Gepreel, M. Niinomi, Biocompatibility of Ti-alloys for long-term implantantion. Journal of the Mechanical Behavior of Biomedical Materials, 2013. http://dx.doi.org/10.1016/j.jmbbm.2012.11.014.

[18]. M. Niinomi; M. Nakai; J. Hieda, Development of new metallic alloys for biomedical applications. Acta Biomaterialia, 8(12), 2012. http://dx.doi.org/10.1016/j.actbio.2012.06.037.

[19]. F. H. Froes, Titanium: Physical Metallurgy Processing and Applications. 1st. ed. ASM International, Ohio, 2015.

[20]. M. Niinomi, Recent research and development in titanium alloys for biomedical applications and healthcare goods. Science and Technology of Advanced Materials, 4, 2003.

[21]. C. N. Elias, J. H. C. Lima, R. Valiev, M. A. Meyers. Biomedical applications of titanium and its alloys. The Journal of The Minerals, Metals & Materials Society, (2008).

[22]. A. Biesiekierski, J. Wang, M. A. -H. Gepreel, C. Wen, A new look at biomedical Ti-based shape memory alloys. Acta Biomaterialia, 8, 2012.

[23]. R. Boyer, G. Welsch, E. W. Collings, Materials Properties Handbook: Titanium Alloys. 4ª. ed. ASM International, 2007.

[24]. C. Leyens, M. Peters. Titanium and Titanium Alloys: Fundamentals and Applications. Winheim: WILEY-VCH Verlag GmbH & Co, 2003. p. 532.

[25]. H. Y. Kim, Y. Ikehara, J. I. Kim, H. Hosoda, S. Miyazaki, Martensitic transformation, shape memory effect and superelasticty of Ti-Nb binary alloys. Acta Materialia, 54(23), 2006.

[26]. L. M. Elias, S. G. Schneider, S. Schneider, H. M. Silva, F. Malvisi, Microstructural and mechanical characterization of biomedical Ti-Nb-Zr(-Ta) alloys. Materials Science and Engineering A, 432, 2006.

[27]. H. Y. Kim, H. Satoru, J. I. Kim, H. Hosoda, S. Miyazaki, Mechanical Properties and Shape Memory Behavior of Ti-Nb Alloys. Materials Transactions, 45(7), 2004, p. 2443-2448.

[28]. V. R. Jablokov, N. G. D. Murray, H. J. Rack, H. L. Freese, Influence of Oxygen Content on the Mechanical Properties of Titanium-35Niobium-7Zirconium-5Tantalum Beta Titanium Alloy. Journal of ASTM International, 2(8), 2005.

[29]. P. L. Ferrandini, F. F. Cardoso, S. A. Souza, C. R. Afonso, R. Caram. Aging response of the Ti-35Nb-7Zr-5T and Ti-35Nb-7Ta alloys. Journal of Alloys and Compounds, 433, 2007.

[30]. D. J. Bryan, E. D. Keys, J. V. Mantione, H. L. Freese, Structural Titanium Biomedical Alloys for Aerospace Applications. Titanium, Orlando, 2010, p. 19.

[31]. M. Tahara, H. Y. Kim, H. Hosoda, T. Nam, S. Miyazaki, Effect of nitrogen addition and annealing temperature on superelastic properties of Ti-Nb-Zr-Ta alloys. Materials Science and Engineering A, 527, 2010.

[32]. Y. Sutou, T. Omori, K. Yamauchi, N. Ono, R. Kainuma, K. Ishida, Effect of grain size and texture on pseudoelasticity in Cu-Al-Mn-based shape memory wire. Acta Materialia, 53, 2005, p.4121-4133.

[33]. S. M. Ueland, Y. Chen, C. A. Schuh, A. Oligocrystalline Shape Memory Alloys. Advanced Functional Materials, 22(10), 2012, p.2094-2099.

[34]. Y. Chen, X. Zhang, D. C. Dunand, C. A. Schuh. Shape memory and superelasticity in polycrystalline Cu-Al-Ni microwires. Applied Physics Letters, (2009), 95(17), p. 2007–2010. https://doi.org/10.1063/1.3257372.

[35]. I. W. Donald, Production, properties and applications of microwire and related products. Journal of Materials Science, 22, 1987, p.2661-2679.

[36]. D. Bourell, J. Pierre, M. Leu, G. Levy, D. Rosen, A. M. Beese, A. Clare, Materials for additive manufacturing, CIRP Annals - Manufacturing Technology, 66(2), 2017, p. 659–681. https://doi.org/10.1016/j.cirp.2017.05.009.

[37]. S. M. Yusuf, N. Gao, Influence of energy density on metallurgy and properties in metal additive manufacturing. Materials Science and Technology, 33(11), 2017, 1269–1289. https://doi.org/10.1080/02670836.2017.1289444.

[38]. W. E. Frazier, Metal additive manufacturing: A review, Journal of Materials Engineering and Performance, 23(6), 2014. https://doi.org/10.1007/s11665-014-0958-z.

[39]. C. Y. Yap, C. K. Chua, Z. L. Dong, Z. H. Liu, D. Q. Zhang, L. E. Loh, S. L Sing. Review of Selective Laser Melting: Materials and applications. Applied Physics Reviews, 2(4), 2015. https://doi.org/10.1063/1.4935926.

[40]. A. Kreitcberg, V. Brailovski, S. Prokoshkin. New biocompatible near-beta Ti-Zr-Nb alloy processed by laser powder bed fusion: Process optimization. Journal of Materials Processing Technology, 252, 2018. https://doi.org/10.1016/j.jmatprotec.2017.10.052.

[41]. J. A. Slotwinski, E. J. Garboczi, P. E. Stutzman, C. F. Ferraris, S. S. Watson, M. A. Peltz, Characterization of Metal Powders Used for Additive Manufacturing. Journal of Research of the National Institute of Standards and Technology, 119, 2014. http://nvlpubs.nist.gov/nistpubs/jres/119/jres.119.018.pdf.

[42]. C. T. Shade; T. F. Murphy, C. Walton, Development of atomized powders for additive manufacturing. World Congress on Powder Metallurgy and Particulate Materials, 2014.

[43]. A. B. B. Spierings, N. T. B. Buchs, G. Levy, N. Herres, G. Levy, Influence of the particle size distribution on surface quality and mechanical properties in AM steel parts. Rapid Prototyping Journal, 17(3), 2011, 195–202. https://doi.org/10.1108/13552541111124770.

[44]. J. H. Tan, W. L. E. Wong, K. W. Dalgarno, An overview of powder granulometry on feedstock and part performance in the Selective Laser Melting process. Additive Manufacturing, 18, 2017. http://dx.doi.org/10.1016/j.addma.2017.10.011.

[45]. H. F. Fischmeister, A. D. Ozerskii, L. Olsson, Solidification structure of gas atomized high-speed steel powders, Powder Metallurgy, 25(1), 1982, p. 1–9. DOI 10.1179/pom.1982.25.1.1.

[46]. D. Sun, D. Gu, K. Lin, J. Ma, W. Chen, J. Huang, X. Sun, M. Chu, Selective laser melting of titanium parts: Influence of laser process parameters on macro- and microstructures and tensile property, Ptec (2018), doi:10.1016/j.powtec.2018.09.090.

[47]. B. Ferrar, L. Mullen, E. Jones, R. Stamp and C. J. Sutcliffe: Gas flow effects on selective laser melting (SLM) manufacturing per- formance, J. Mater. Process. Technol., 212, 2012, p.355–364.

[48]. V. S. Sufiiarov, A. A. Popovich, E. V. Borisov, I. A. Polozov, D. V. Masaylo, A. V. Orlov, The Effect of Layer Thickness at Selective Laser Melting. Procedia Engineering, 174, 2017, p. 126–134. https://doi.org/10.1016/j.proeng.2017.01.179.

[49]. P. Karimi, T. Raza, J. Anderson, L. E. Svensson, Influence of laser exposure time and point distance on 75-μm-thick layer of selective laser melted Alloy 718. International Journal of Advanced Manufacturing Technology, 94(5–8), 2018.

[50]. T. Kurzynowski, E. Chlebus, B. Kuźnicka, J. Reiner, Parameters in selective laser melting for processing metallic powders. In Proc. SPIE 8239: High Power Laser Materials Processing: Lasers, Beam Delivery, Diagnostics, and Applications, 8239, 2012, p. 823914. https://doi.org/10.1117/12.907292.

[51]. N.T. Aboulkhair, N. M. Everitt, T. C. Ashcroft, Reducing porosity in AlSi10Mg parts processed by selective laser melting. Addit. Manuf. 1, 2014, p.77–86.

[52]. X. Su, Y. Yang, Research on track overlapping during Selective Laser Melting of powders. Journal of Materials Processing Technology, 212(10), 2012, p.2074–2079. https://doi.org/10.1016/j.jmatprotec.2012.05.012.

[53] K. G. Prashanth, S. Scudino, T. Maity, J. Das, J. Eckert, Is the energy density a reliable parameter for materials synthesis by selective laser melting?, Materials Research Letters, 5(6), 2017, p.386-390, DOI: 10.1080/21663831.2017.1299808.

[54]. T. Mukherjee, W. Zhang, T. DebRoy, An improved prediction of residual stresses and distortion in additive manufacturing. Comp Mater Sci, 126, 2017, p.360–72.

[55]. S. A. David, T. DebRoy, Current issues and problems in welding science. Science, 257(5069), 1992, p.497–502.

[56]. T. DebRoy, S. A. David, Physical processes in fusion welding. Rev Mod Phys, 67(1), 1995, p.85–112.

[57]. M. Markl, C. Korner, Multiscale modeling of powder bed-based additive manufacturing. Ann Rev Mater Res, 46, 2016, p.93–123.

[58]. S. Kou. Welding metallurgy. 2nd ed. John Wiley & Sons. Hoboken, NJ, 2003.

[59]. J. C. Lippold, Welding metallurgy and weldability. John Wiley and Sons Hoboken, NJ, 2014.

[60]. G. J. Davies, J. G. Garland, Solidification Structures and Properties of Fusion Welds. International Metallurgical Reviews, 20, 1975.

[61]. A. David, J. M. Vitek, Correlation between solidification parameters and weld microstructures. International Materials Reviews, 34(5), 1989.

[62]. A. Garcia, Solidificação: Fundamentos e Aplicações. 2ª. ed. Campinas: Unicamp, 2007, p.399.

[63]. D. A. Porter, K. E. Easterling, M. Y. Sherif, Phase Transformations in Metals and Alloys. 3ª. ed. CRC Press Taylor & Francis Group, 2009, p.538.

[64]. V. Manvatkar, A. De, T. DebRoy, Heat transfer and material flow during laser assisted multi-layer additive manufacturing, J Appl Phys,116(12), 2014.

[65]. L. Thijs, Microstructure and Texture of Metal Parts Produced by Selective Laser Melting, Doctoral Thesis, KU Leuven, Belgium, 2014.

[66]. V. Manvatkar, A. De, T. DebRoy, Spatial variation of melt pool geometry, peak temperature and solidification parameters during laser assisted additive manufacturing process. Mater Sci Tech.,31(8), 2015, p.924–930.

[67]. L. Thijs, M. L. M. Sistiaga, R. Wauthle, Q. G. Xie, J. -P. Kruth, J. V. Humbeeck, Strong morphological and crystallographic texture and resulting yield strength anisotropy in selective laser melted tantalum, Acta Mater., 61(12), 2013, p.4657–68.

[68]. A. A. Antonysamy, J. Meyer, P. B. Prangnell, Effect of build geometry on the β-grain structure and texture in additive manufacture of Ti6Al4V by selective electron beam melting. Materials Characterization, 84, 2013. https://doi.org/10.1016/j.matchar.2013.07.012.

[69]. L. Thijs, K. Kempen, J. -P. Kruth, J. V. Humbeeck, Fine-structured aluminium products with controllable texture by selective laser melting of pre-alloyed AlSi10Mg powder, Acta Mater, 61(5), 2013, p.1809–19.

[70]. N. Raghavan, R. Dehoff, S. Pannala, S. Simunovic, M. Kirka, J. Turner, Numerical modeling of heat-transfer and the influence of process parameters on tailoring the grain morphology of IN718 in electron beam additive manufacturing. Acta Mater, 112, 2016, p.303–14.

[71]. T. Wang, Y. Y. Zhu, S. Q. Zhang, H. B. Tang, H. M. Wang, Grain morphology evolution behavior of titanium alloy components during laser melting deposition additive manufacturing. J. Alloy. Comp., 632, 2015, p.505–13.

[73]. B. Vrancken, R. Wauthlé, J. -P. Kruth, J. Van Humbeeck, Study of the Influence of Material Properties on Residual Stress in Selective Laser Melting. Proceedings of SFF Symposium, Austin TX USA, 2013, p.393–407.

[74]. A. Basak, S. Das, Epitaxy and microstructure evolution in metal additive manufacturing. Ann Rev Mater Res, 46(1), 2016, p.125–49.

[75]. H. L. Wei, J. W. Elmer, T. DebRoy, Origin of grain orientation during solidification of an aluminum alloy. Acta Mater, 115, 2016, p.123–31.

[76]. L. Thijs, M. L. M. Sistiaga, R. Wauthle, Q. Xie, J. -P. Kruth, J. Van Humbeeck, Strong Morphological and Crystallographic Texture and Resulting Yield Strength Anisotropy in Selective Laser Melted Tantalum. Acta Materialia, 61, (2013), p.4657–4668.

[77]. S. Dadbakhsh, B. Vrancken, J. -P. Kruth, J. Luyten, J. Van Humbeeck, Texture and Anisotropy in Selective Laser Melting of NiTi Alloy. Materials Science and Engineering: A, 650, 2016, p.225–232.

[78]. M. Garibaldi, I. Ashcroft, M. Simonelli, R. Hague, Metallurgy of high-silicon steel parts produced using Selective Laser Melting. Acta Mater, 110, 2016, p.207–16.

[79]. H. Helmer, A. Bauereiß, R. F. Singer, C. Körner, Grain structure evolution in Inconel 718 during selective electron beam melting. Mater Sci Eng A, 668, 2016, p.180–7.

[80]. S. Saedi, A. Sadi, M. Taheri, N. Shayesthe, Texture, aging, and superelasticity of selective laser melting fabricated Ni-rich NiTi alloys. Materials Science and Engineering A, 686, n. A, 2017.

[81]. M. Fischer, D. Joguet, L. Peltier, P. Laheurte, In situ titanium alloy elaborated by selective laser melting of Ti-Nb mixed powder. Proceedings of the 13th World Conference on Titanium, The Minerals, Metals & Materials Society, 2016.

[82]. H. Schwab, K. G. Prashanth, L. Löber, U. Kühn, J. Eckert, Selective Laser Melting of Ti-45Nb Alloy. Metals, 5, 2015.

[83]. C. Baker, The Shape-Memory Effect in a Titanium-35wt% Niobium Alloy. Metal Science Journal, 5, 1971.

[84]. M. Bönisch, Structural properties, deformation behavior and thermal stability of martensitic Ti-Nb alloys, Doctoral Thesis, Dresden University of Technology, 2016. p. 160.

[85]. H. Y. Kim; S. Miyazaki, Several Issues in the Development of Ti-Nb-based Shape Memory Alloys. Shape Memory and Superelasticity, 2(4), 2016.

[86]. D. L. Moffat and D. C. Larbalestier, The competition between martensite and omega in quenched Ti-Nb alloys. Metall. Trans. A, 19, 1988, p.1677–1686.

[87]. A. Ramarolahy et al. Microstructure and mechanical behavior of superelastic Ti-24Nb-0,5O and Ti-24Nb-0,5N biomedical alloys. Journal of the Mechanical Behavior of Biomedical Materials, 9, 2012.

[88]. D. C. Zhang et al. Effect of ternary alloying elements on microstructure and superelasticity of Ti-Nb alloys. Materials Science and Engineering A, 559(A), 2013.

[89]. C. R. M. Afonso, P. L. Ferrandini, A. J. Ramirez, R. Caram, High resolution transmission electron microscopy study of the hardening mechanism through phase separation in a beta-Ti-35Nb-7Zr-5Ta alloy for implant application. Acta Biomaterialia, 6, 2010.

[90]. S. M. Ueland, C. A. Schuh, Superelasticity and fatigue in oligocrystalline shape memory alloy microwires. Acta Materialia, 60, 2012.

[91]. N. Tuncer, C. A. Schuh, Melt-cast microfibers of Cu-based shape memory alloy adopt a favorable texture for superelasticity. Scripta Materialia, 117, 2016.

[92]. Y. Chen, C. A. Schuh, Size effects in shape memory alloy microwires. Acta Materialia, 59, 2011.

[93]. Y. Sutou, T. Omori, R. Kainuma, K. Ishida, Grain size dependence of pseudoelasticity in polycrystalline Cu-Al-Mn-based shape memory sheets. Acta Materialia, 61, 2013.

[94]. J. Boeslau, D. Raabe, Development of microtextures in cold rolled iron-oligocrystals. Materials Science Forum\Proceedings of the 10th International Conference on Textures of Materials. Part 2 (of 2), 1994, p.501–506.

[95]. M. F. Qian, X. X. Zhang, L. S. Wei, L. Geng, H. X. Peng, Structural, Magnetic and Mechanical Properties of Oligocrystalline Ni-Mn-Ga Shape Memory Microwires. Materials Today: Proceedings, 2, 2015, S577–S581.

[96]. B. Chen, J. Jiang, F. P. E. Dunne, Microstructurally-sensitive fatigue crack nucleation in Ni-based single and oligo crystals. Journal of the Mechanics and Physics of Solids, 106, 2017, 15–33.

[97]. S. Weiss, G. Gottstein, Evolution of microstructure during high temperature low cycle fatigue of high purity aluminium oligocrystals. Materials Science and Technology, 14(11), 1998, 1169–1174.

[98]. H. R. Z. Sandim, A. F. Padilha, V. Randle, W. Blum. Grain subdivision and recrystallization in oligocrystalline tantalum during cold swaging and subsequent annealing. International Journal of Refractory Metals and Hard Materials, 17(6), 1999, p.431–435.

[99]. T. Kusama, T. Omori, T. Saito, S. Kise, T. Tanaka, Y. Araki, R. Kainuma. Ultra-large single crystals by abnormal grain growth. Nature Communications, (2017), 8(1), p. 1–8. https://doi.org/10.1038/s41467-017-00383-0.

[100]. T. Omori, T. Kusama, S. Kawata, I. Ohnuma, Y. Sutou, Y. Araki, R. Kainuma. Abnormal Grain Growth Induced by Cyclic Heat Treatment. Science, (2013), 341(6153), p. 1500–1502. https://doi.org/10.1126/science.1238017.

[101]. P. Gargarella. Phase formation, thermal stability and mechanical behaviour of TiCu-based alloy. Doctoral Thesis. Dresden University of Technology, 2013.

[102]. P. Karimi, T. Raza, J. Andersson, L. E. Svensson, Influence of laser exposure time and point distance on 75-μm-thick layer of selective laser melted Alloy 718. International Journal of Advanced Manufacturing Technology. 2018. Vol. 94, no. 5–8, p. 2199–2207. DOI 10.1007/s00170-017-1019-1.

[103]. K. Kempen, Expanding the materials palette for Selective Laser Melting of metals, Doctoral Thesis, University of Luven, 2015.

[104]. J. A. Slotwinski, E. J. Garboczi, P. E. Stutzman, C. F. Ferraris, S. S. Watson, M. A. Peltz, Characterization of Metal Powders Used for Additive Manufacturing. Journal of Research of the National Institute of Standards and Technology, 119, 2014. http://nvlpubs.nist.gov/nistpubs/jres/119/jres.119.018.pdf.

[105]. A. du Plessis, I. Yadroitsev, I. Yadroitsava, S. G. Le Roux, X-Ray Microcomputed Tomography in Additive Manufacturing: A Review of the Current Technology and Applications. 3D Printing and Additive Manufacturing, 5(3), 2018. https://doi.org/10.1089/3dp.2018.0060.

[106]. J. A. Slotwinski, E. J. Garboczi, K. M. Hebenstreit. Porosity Measurements and Analysis for Metal Additive Manufacturing Process Control. Journal of Research of the National Institute of Standards and Technology, 119(494), 2014. https://doi.org/10.6028/jres.119.019.

[107]. Y. Guo. Beta-BCC et Alliages Amorphes Biocompatibles à Base de Titane pour les Implants, (2014).

[108]. J. I. Qazi, V. Tsakiris, B. Marquardt, H. J. Rack, Effect of Aging Treatments on the Tensile Properties of Ti-35Nb-7Zr-5Ta-(0,06-0,7)O Alloys. Journal of ASTM International, 2, n. 8, 2005.

[109]. R.E. Reed-Hill, R. Abbaschian, Physical Metallurgy Prin- ciples, 3rd ed. Boston, MA: PWS Publishing Company; 1994, p 284–285.

[110]. A.H. Cottrell; B. A. Bilby, Dislocation Theory of Yielding and Strain Ageing of Iron. Metallurgy Department, University of Birmingham. [S.l.]. 1948.

[111]. A.H. Cottrell; M. A. Jaswon, Distribution of Solute Atoms Round a Slow Dislocation. Proceedings of the Royak Society of London, Serie A, Mathematical and Physical Sciences, 1949. 104-114.

[112]. C. Schulze, M. Weinmann, C. Schweigel, O. Keßler, R. Bader, Mechanical properties of a newly additive manufactured implant material based on Ti-42Nb. Materials, 11(124), 2018. https://doi.org/10.3390/ma11010124.

[113]. G. Yablokova, M. Speirs, J. Van Humbeeck, J. P. Kruth, J. Schrooten, R. Cloots, J. Luyten, Rheological behavior of β-Ti and NiTi powders produced by atomization for SLM production of open porous orthopedic implants. Powder Technology, 283, 2015. https://doi.org/10.1016/j.powtec.2015.05.015.

[114]. F. Thummler and R. Oberacker, Introduction to Powder Metallurgy [online]. 1995. ISBN 0-901716-26-X. Available from: http://linkinghub.elsevier.com/retrieve/pii/1044580395800379A.

[115]. A.B. Spierings, N. Herres and G. Levy, Influence of the particle size distribution on surface quality and mechanical properties in AM steel parts. Rapid Prototyping Journal [online]. 2011. Vol. 17, no. 3, p. 195–202. DOI 10.1108/13552541111124770. Available from: http://www.emeraldinsight.com/doi/10.1108/13552541111124770.

[116]. C. T. Schade, T. F. Murphy, C. Walton, Development of atomized powders for additive manufacturing. World Congress on Powder Metallurgy and Particulate Materials, PM 2014, May 18, 2014 - May 22, 2014. 2014. P. 215–226.

[117]. I. Yadroitsev, I. Smurov, Selective Laser Melting technology: From the single laser melted track stability to 3D parts of complex shape. Physics Procedia, 5(2), 2010, p. 551–560. https://doi.org/10.1016/j.phpro.2010.08.083.

[118]. I. Yadroitsev, A. Gusarov, I. Yadroitsava, I. Smurov, Single track formation in Selective Laser Melting of metal powders. Journal of Materials Processing Technology, 210(12), 2010.

[119] I. Yadroitsev, P. Bertrand, I. Smurov, Parametric analysis of the Selective Laser Melting process. Applied Surface Science, 253(19), 2007.

[120] T. Gustmann, A. Neves, U. Kühn, P. Gargarella, C. S. Kiminami, C. Bolfarini, J. Eckert, S. Pauly, Influence of processing parameters on the fabrication of a Cu-Al-Ni-Mn shape-memory alloy by Selective Laser Melting. Additive Manufacturing, 11, 2016.

[121]. Y. D. Zhang, D. P. Zhao, Y. J. Huang, M. Yan, J. H. Zhang, J. P. Luo, J. F. Sun, Low-modulus biomedical Ti–30Nb–5Ta–3Zr additively manufactured by Selective Laser Melting and its biocompatibility. Materials Science and Engineering: C, (2018), 97, p. 275–284. https://doi.org/10.1016/j.msec.2018.11.077.

[122]. S. L. Sing, F. E. Wiria, W. Y. Yeong, Selective laser melting of titanium alloy with 50 wt% tantalum: Effect of laser process parameters on part quality. International Journal of Refractory Metals and Hard Materials, (2018), 77, 120–127. https://doi.org/10.1016/j.ijrmhm.2018.08.006.

[123]. W. Chen, C. Chen, X. Zi, X. Cheng, X. Zhang, Y. C. Lin, K. Zhou, Controlling the microstructure and mechanical properties of a metastable β

titanium alloy by selective laser melting. Materials Science and Engineering A, (2018), 726(January), p. 240–250. https://doi.org/10.1016/j.msea.2018.04.087.

[124]. M. Simonelli, Y. Y. Tse, C. Tuck, Effect of the build orientation on the mechanical properties and fracture modes of SLM Ti-6Al-4V. Materials Science and Engineering A, 616, (2014), p. 1–11. https://doi.org/10.1016/j.msea.2014.07.086.

[125]. W. Li, J. Liu, S. Wen, Q. Wei, C. Yan, Y. Shi, Crystal orientation, crystallographic texture and phase evolution in the Ti-45Al-2Cr-5Nb alloy processed by selective laser melting. Materials Characterization, (2016), 113, 125–133. https://doi.org/10.1016/j.matchar.2016.01.012.

[126]. T. Ishimoto, K. Hagihara, K. Hisamoto, S. H. Sun, T. Nakano, Crystallographic texture control of beta-type Ti–15Mo–5Zr–3Al alloy by selective laser melting for the development of novel implants with a biocompatible low Young’s modulus. Scripta Materialia, (2017), 132, 34–38. https://doi.org/10.1016/j.scriptamat.2016.12.038.

[127]. H. Schwab, F. Palm, U. Kühn, J. Eckert, Microstructure and mechanical properties of the near-beta titanium alloy Ti-5553 processed by selective laser melting. Materials and Design, (2016), 105, 75–80. https://doi.org/10.1016/j.matdes.2016.04.103.

[128]. L. N. Carter, C. Martin, P. J. Withers, M. M. Attallah. The influence of the laser scan strategy on grain structure and cracking behaviour in SLM powder-bed fabricated nickel superalloy. Journal of Alloys and Compounds, (2014), 615, p. 338–347. https://doi.org/10.1016/j.jallcom.2014.06.172.

[129]. I. Tolosa, F. Garciandía, F. Zubiri, Study of mechanical properties of AISI 316 stainless steel processed by selective laser melting, following different manufacturing strategies, (2010), p. 639–647. https://doi.org/10.1007/s00170-010-2631-5.

[130]. G. Pyka, A. Burakowski, G. Kerckhofs, M. Moesen, S. Van Bael, J. Schrooten, Surface modification of Ti6Al4V open porous structures produced by additive manufacturing. Adv Eng Mater, 2012, 14, p. 363–70.

[131]. J. V. der Stok, O.P. V. der Jagt, S. A. Yavari, M. F. De Haas, J. H. Waarsing, H. Jahr, Selective laser melting-produced porous titanium scaf- folds regenerate bone in critical size cortical bone defects. J Orthop Res., 2013, 31, p. 792–9.

[132] S. A. Yavari, J. V. der Stok, Y. C. Chai, R. Wauthle, Z. B. Tahmasebi, P. Habibovic,, Bone regeneration performance of surface-treated porous titanium. Biomaterials, 2014, 35, p. 6172–81.

[133]. A. Yadollahi, N. Shamsaei, S. M. Thompson, A. Elwany, L. Bian, Effects of building orientation and heat treatment on fatigue behavior of selective laser melted 17-4 PH stainless steel. International Journal of Fatigue, (2017), 94, 218–235. https://doi.org/10.1016/j.ijfatigue.2016.03.014.

[134]. E. Yasa, J. Kruth, Application of Laser Re-Melting on Selective Laser Melting Parts. Advances in Production Engineering & Management, (2011), 6(4), 259–270.

[135]. E. Yasa, J. Deckers, J. Kruth, The investigation of the influence of laser re-melting on density, surface quality and microstructure of selective laser melting parts. Rapid Prototyping Journal, (2011), 17(5), 312–327. https://doi.org/10.1108/13552541111156450.

[136]. L. C. Zhang, D. Klemm, J. Eckert, Y. L. Hao, T. B. Sercombe, Manufacture by selective laser melting and mechanical behavior of a biomedical Ti-24Nb-4Zr-8Sn alloy. Scripta Materialia, (2011) 65(1), p. 21–24. https://doi.org/10.1016/j.scriptamat.2011.03.024.

[137]. P. Edwards, M. Ramulu, Effect of build direction on the fracture toughness and fatigue crack growth in selective laser melted Ti-6Al-4-‰V. Fatigue and Fracture of Engineering Materials and Structures, (2015), 38(10), 1228–1236. https://doi.org/10.1111/ffe.12303.

[138]. S. H. Lee, M. Todai, M. Tane, K. Hagihara, H. Nakajima, T. Nakano, Biocompatible low Young’s modulus achieved by strong crystallographic elastic anisotropy in Ti-15Mo-5Zr-3Al alloy single crystal. Journal of the Mechanical Behavior of Biomedical Materials, (2012), 14, 48–54. https://doi.org/10.1016/j.jmbbm.2012.05.005.

[139]. J. -P. Kruth, P. Mercelis, J. Van Vaerenbergh, L. Froyen, M. Rombouts, Binding mechanisms in selective laser sintering and selective laser melting, Rapid Prototyping Journal, 11, 2005, p. 1355-2546.

[140]. J. -P. Kruth, B. Vandenbroucke, I. J. Van Vaerenbergh, I. Naert, Rapid manufacturing of dental prostheses by means of selective laser sintering/melting, Proceedings of the AFPR, S4, University of Twente, Enschede, The Netherlands, 2005.

[141]. B. Vandenbroucke, J. P. Kruth, Selective laser melting of biocompatible metals for rapid manufacturing of medical parts, Rapid Prototyping Journal, 13(4), 2007. https://doi.org/10.1108/13552540710776142.

[142]. F.J. Humphreys and M. Hatherly, Recrystallization and Related Annealing Phenomena, Pergamon Press, 1995, p. 281–325.

[143] J.H. Martin, B.D. Yahata, J.M. Hundley, J.A. Mayer, T.A. Schaedler, T.M. Pollock, Nature 549 (2017) 365.

[144]. G. Dieter, Mechanical Metallurgy, 3rd Edition ed., Mc Graw-Hill Book Co., New York, 1986.

[145]. E. G. Obbard, Y. L. Hao, R. J. Talling, S. J. Li, Y. W. Zhang, D. Dye, R. Yang, The effect of oxygen on a α” martensite and superelasticity in Ti – 24Nb – 4Zr – 8Sn. Acta Materialia, 59, 2011, p. 112–125.